Grand Valley State University

ScholarWorks@GVSU

5-9-2023

Surface Electromyographic (sEMG) Transduction of Hand Joint Angles for Human Interfacing Devices (HID)

Brendan P. Beauchamp
Grand Valley State University

Follow this and additional works at: https://scholarworks.gvsu.edu/theses

Part of the Engineering Commons

Surface Electromyographic (sEMG) Transduction of Hand Joint Angles
for Human Interfacing Devices (HID)

Brendan Philip Beauchamp

A Thesis Submitted to the Graduate Faculty of

GRAND VALLEY STATE UNIVERSITY

In

Partial Fulfillment of the Requirements

For the Degree of

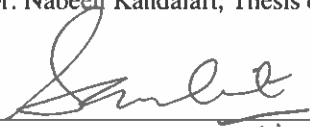Master of Science in Engineering
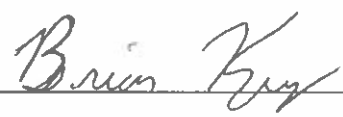
Biomedical Engineering

April 2023

Thesis Approval Form

![Grand Valley State University logo]

GRAND VALLEY STATE UNIVERSITY

The signatories of the committee below indicate that they have read and approved the thesis of Brendan P. Beauchamp in partial fulfillment of the requirements for the degree of Master of Science in Engineering.

_____ 4/25/2023

Dr. Nabeeh Kandalaft, Thesis committee chair   Date

_____ 4/25/23

Dr. Samhita Rhodes, Committee member   Date

_____ 4/26/23

Dr. Brian Krug, Committee member   Date

_____ 4/25/23

Dr. Karl Brakora, Committee member   Date

_____ **04/20/2023**

Dr. Gordon Alderink, Committee member   Date

Accepted and approved on behalf of the   Accepted and approved on behalf of the
Padnos College of Engineering & Computing   Graduate Faculty

_____   _____

Dean of the College   Dean of The Graduate School

4/26/2023   5/9/2023
_____   _____

Date   Date

Dedication

To the idea that anything is possible if you work hard enough.

Mom & Dad – thank you for supporting me and encouraging me to chase my dreams. I always say that my temperament comes from both of you: my love of science from you mom, and my critical thinking and problem-solving you dad. I cherish these gifts and am forever grateful for them. Thank you for sharing your energy and unique perspectives on the world with me.

Milo – I know you are a cat and never going to read this but thank you for running to the door every time I come home and sleeping by my feet even though I kick you off the bed every night.

Dr. Kandalaft – You believed in me from day one and have always treated me like family. I want you to know that I will cherish your teachings forever. I am excited to start my next project and apply myself as proficiently as you have expected during my graduate studies.

Allie – I love you with all of my heart. Thank you for standing by my side and being my best friend.

Acknowledgements

Abstract

    This is an investigation of the use of surface electromyography (sEMG) as a tool to improve human interfacing devices (HID) information bandwidth through the transduction of the fingertip workspace. It combines the work of Merletti et al and Jarque-Bou et al to design an open-source framework for Fingertip Workspace based Human Interfacing Devices (HID). In this framework, the fingertip workspace is defined as the system of forearm and hand muscle force through a tensor which describes hand anthropometry. The thesis discusses the electrophysiology of muscle tissue along with the anatomy and physiology of the arm in pursuit of optimizing sensor location, muscle force measurements, and viable command gestures. Algorithms for correlating sEMG to hand joint angle are investigated using MATLAB for both static and moving gestures.

Seven sEMG spots and Fingertip Joint Angles recorded by Jarque Bou et al are investigated for the application of sEMG to Human Interfacing Devices (HID). Such technology is termed Gesture Computer Interfacing (GCI) and has been shown feasible through devices such as CTRL Labs interface, and models such as those of Sartori, Merletti, and Zhao. Muscles under sEMG spots in this dataset and the actions related to them are discussed, along with what muscles and hand actions are not visible within this dataset. Viable gestures for detection algorithms are discussed based on the muscles discerned to be visible in the dataset through intensity, spectral moment, power spectra, and coherence. Detection and isolation of such viable actions is fundamental to designing an EMG driven musculoskeletal model of the hand needed to facilitate GCI.

    Enveloping, spectral moment, power spectrum, and coherence analysis are applied to a Sollerman Hand Function Test sEMG dataset of twenty-two subjects performing 26 activities of living to differentiate pinching and grasping tasks. Pinches and grasps were found to cause very different activation patterns in sEMG spot 3 relating to flexion of digits I - V. Spectral moment was found to be less correlated with differentiation and provided information about the degree of object manipulation performed and extent of fatigue during each task. Coherence was shown to increase between flexors and extensors with intensity of task but was found corrupted by crosstalk with increasing intensity of muscular activation. Some spectral results correlated between finger flexor and extensor power spectra showed anticipatory coherence between the muscle groups at the end of object manipulation.

    An sEMG amplification system capable of capturing HD-sEMG with a bandwidth of 300 and 500 Hz at a sampling frequency of 2 kHz was designed for future work. The system was designed in ordinance with current IEEE research on sensor-electrode characteristics. Furthermore, discussion of solutions to open issues in HD-sEMG is provided. This work did not implement the designed wristband but serves as a literature review and open-source design using commercially available technologies.

Table of Contents

List of Tables

List of Figures

List of Abbreviations/Symbols

HID	Human Interface Device
EMG	Electromyography
sEMG	Surface Electromyography
HD-sEMG	High-Density Surface Electromyography
MU	Motor Unit
IAP	Intracellular Action Potential
MUAP	Motor Unit Action Potential
Ω	Ohm
V	Volt
A	Amp
F	Farad
V/V, G	Gain
D	Diode
R	Resistor
C	Capacitor
U	Integrated Circuit
VIn	Voltage In
VOut	Voltage Out
SNR	Signal to Noise Ratio
IED	Inter Electrode Distance
Hz	Hertz
m	meter
ICA	Independent Component Analysis
IP	Interphalangeal
DIP	Distal Interphalangeal
PIP	Peripheral Interphalangeal

MCP	Metacarpo-Phalangeal
CMC	Carpo-Metacarpal
TM	Trapezio-Metacarpal
DOF	Degree(s) of Freedom
q	Joint Angles
SHFT	Sollerman Hand Function Test
ADL	Activit(y/ies) of Daily Living
USB	Universal Serial Bus
NMM	Neuromusculoskeletal Modeling
CMRR	Common Mode Rejection Ratio
ECG	Electrocardiography
ADC	Analog to Digital Conversion
$e(t)$	Rectified and Low-Pass Filtered electromyography signal
γ_1	Neural Activation Hyperparameter 1
γ_2	Neural Activation Hyperparameter 2
d	Electromechanical Delay of sEMG, diameter of electrode
$u(t)$	Neural Activation based on electromyography
A Line	Non-linearization to Muscle Activation Relationship
$a(t)$	Muscle Activation based on electromyography
F^{mt}	Musculotendinous Force
Υ	Joint Angle Moment
DH	Denavit-Hartenberg
Φ	Distal Inter-Phalangeal Joint Angle
θ	Peripheral Inter-Phalangeal Joint Angle
APL	Abductor Pollicis Longus
BR	Brachioradialis
ECRB	Extensor Carpi Radialis Brevis
ECRL	Extensor Carpi Radialis Longus

ECU	Extensor Carpi Ulnaris
EDC	Extensor Digitorum Communis
EDM	Extensor Digiti Minimi
EI	Extensor Indicis
EPB	Extensor Pollicis Brevis
EPL	Extensor Pollicis Longus
FCR	Flexor Carpi Radialis
FCU	Flexor Carpi Ulnaris
FDP	Flexor Digitorum Profundus
FDS	Flexor Digitorum Superficialis
FPL	Flexor Pollicis Longus
PL	Palmaris Longus
PT	Pronator Teres
GCI	Gesture Computer Interfacing
fPCA	Functional Principal Component Analysis
MSC	Magnitude Squared Coherence
BSS	Blind Source Separation
X(f)	Fourier transform of time domain signal
F_{max}	Maximum Frequency
P_{tot}	Total Power
F_m	Median Frequency
S	Spectrogram
CS	Coherence Spectrogram
DPSS	Discrete Prolate Spheroidal Sequences
DAQ	Data Acquisition Unit
ESD	Electrostatic Discharge
PCB	Printed Circuit Board
BOM	Bill of Materials

I/O	Input/Output
SPI	Serial Peripheral Interface
SCLK	SPI Clock
SPS	Samples per Second
FRAM	Ferroelectric Random Access Memory
MQTT	IBM MQ Telemetry Transport
FPGA	Field Programmable Gate Array
IEEE	Institute of Electrical and Electronics Engineers
3D	Three Dimensional
CAD	Computer Aided Design
HMI	Human Machine Interface

Chapter 1 – Introduction

1.1 - Muscle Electrophysiology and Neuromuscular Control

The neuromuscular system is responsible for generating voluntary and involuntary movement in the human body. Movement is initiated when electrochemical signals called action potentials travel onto Motor Units (MUs), which are composed of a motor neuron and all the muscle fibers it innervates. These signals originate from nerves as Intracellular Action Potentials (IAP) that propagate from the central and peripheral nervous system. The exchange between these signals and muscle fibers leads to Motor Unit Action Potentials (MUAP), which prompt muscle fiber contraction to generate movement [1]. This interaction takes place at the cervicothoracic junction for forearm muscles.

During the muscle contraction process, an action potential travels down a motor neuron as an IAP. When this action potential reaches the neuromuscular junction of a single fiber in the MU, it triggers cross-bridging between actin and myosin protein fibers, causing the muscle to contract. The influx and outflux of sodium and potassium in the cross-bridging cycle lead to a potential difference in the membrane of active tissue, which is propagated to the surface of the skin through conduction. The measurement of this neuromuscular signal from the surface of the skin is known as surface electromyography (sEMG) [1]. This signal is modeled as a linear combination of MUAP deep and proximal to the electrode and Gaussian noise, which represents electromagnetic interference, motion artifacts, and other unintentionally acquired bioelectric signals. Proper electrode placement allows sEMG to effectively drive physiological models of humans through the DEMOVE grant project [1].

Action potentials originate from alpha motor neurons and travel as IAP to the muscles they innervate. This is achieved through the release of acetylcholine (ACH) from the terminal bouton of the neuron onto the muscles' motor end plates. ACH reacts with nicotinic ACH receptors on the motor end plate, triggering sodium influx into the myofibrils, generating an action potential on the myofibrils, which travels to the transverse tubules of the cell and activates DHP receptors. Calcium influx from the sarcoplasmic reticulum to the sarcomere occurs due to DHP receptor activation. Calcium presence induces the cross-bridging cycle and causes contraction of the muscle cell [2].

Muscular contraction is the summation of the force caused by all activated motor units, which are comprised of small (slow-twitch) and large (fast-twitch) muscle fibers; these motor units are bundled and integrated randomly throughout the entire muscle. Summation occurs spatiotemporally as both quantal (the number of MU recruited) and wave (frequency of stimulus) summation. Therefore, graded contractions can be produced through activation of combinations of muscle fibers. Additionally, sustained contractions are produced by the asynchronous stimulation of different motor units. Motor control is also affected by agonist inhibition of antagonist muscles, innervation of the muscle spindle to maintain proper tension, and the Golgi tendon response protecting muscle from tearing by inhibiting during excessive load [2].

The body has three types of muscle fibers that motor units may activate to fine-tune the muscular contraction generated shown in Figure 1.1; namely Type IIx, Type IIA, and Type I. Type II fibers are fast twitch and produce tension quickly after stimulation, used for quick and powerful movements. Type IIA has a higher oxidative capacity, meaning it can produce tension for a longer time, while Type I fibers are slow twitch and can sustain contraction for long periods without fatigue due to their rich blood supply and increased mitochondrial density [2]. Selective activation

of different muscle fiber groups enables differentiation of muscle tension or force through the coordination of these three fiber types, allowing the same muscle to be utilized for endurance, strength training, and precise motion.
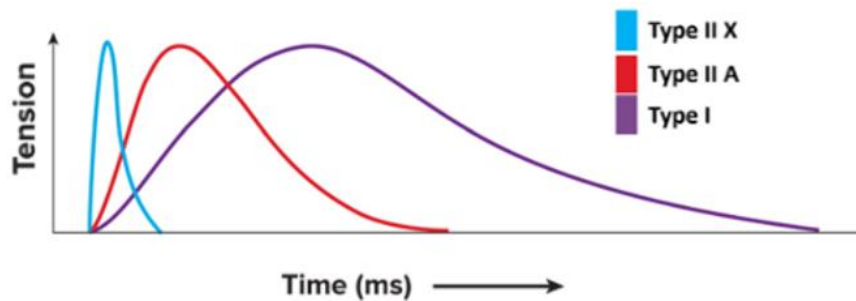
Figure 1.1: Time vs Tension Muscle Fibers [2]

1.2 - Surface Electromyography

Unamplified, measuring electromyography (EMG) signals measured from the surface of the skin will yield voltages ranging between 0 and 10 millivolts, and capture electrical activity approximately 2 centimeters below the surface of the skin. Most of the power of this signal is concentrated to frequencies ranging from 20 to 200 Hz, but sEMG signals do have artifacts extending up to 1000 Hz [3]. The signal measured is the linear combination of proximal MUAP beneath the sensor and noise generated by the conductor effects of the arm. Furthermore, noise is caused by inherent noise in electronic equipment, motion artifacts, ambient noise, and inherent instability in the signal [4]. This noise can be one to three orders of magnitude larger than the muscle's signal.

A significant area of study in the reduction of sEMG noise is the Electrode - Gel - Skin Interface. Merletti et al states that these interfaces are required to have low noise with a standard deviation approximately between 5 and 10 microvolts, and an impedance for the entire electrode skin

interface to be less than 0.5 megaohms [1]. Most of this impedance comes from the Gel - Skin interface, methods to reduce this impedance have been reviewed extensively. The optimal method for reduction of this impedance was found by Piervirgili et al to be through rubbing the surface with an abrasive conductive paste [5]. A circuit model for the electrode skin impedance is shown below in Figure 1.2 where the half or full cell potential is dependent on monopolar or bipolar configuration.

Z_e = Electrode-Skin Impedance
V_b = Half (or Full) Cell Potential
V_n = Random Noise Generator
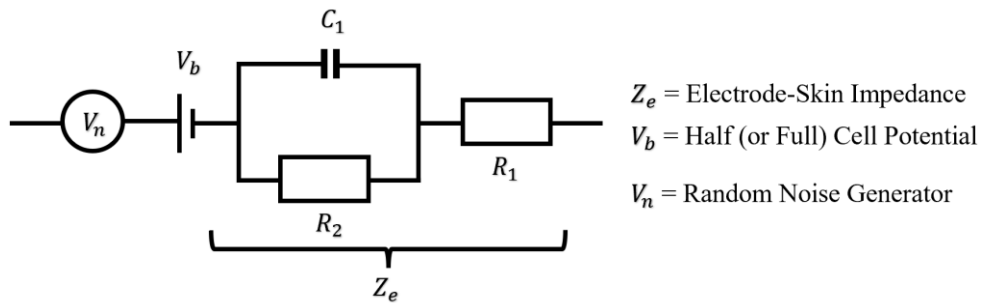
Figure 1.2: Electrode Skin Impedance Circuit [1]

If noise is controlled, muscle activity can be amplified and measured as electrical signals from the surface of the skin. The measurement of these electric potentials requires sensors with high signal to noise ratio that can capture the full frequency spectra of the signal and pass required safety measures for use on human patients. If these sensors are small enough and in high enough density, an accurate estimate of a muscle's force can be made. A high-density map of forearm electrical activity is desired to estimate locomotive drivers for the hand and reduce the crosstalk between individual sEMG channels measured [6].

One of the most heavily studied methods for quantization of MUAP activity is electromyography (EMG). This technology uses electrodes to measure the firing pattern of muscles and condition the signal into a measurable quantity. When this technology is applied using electrodes on the surface of the skin, it is known as surface EMG or sEMG. The technology is used

widely in the study of biomechanics and is less invasive than other prevalent methods of measuring muscle activity such as fine wire EMG. The signal measured from one sEMG sensor is equal to the linear combination of MUAP active underneath the sensor plus gaussian noise. The voltage of this signal ranges from several tens of microvolts to millivolts [7]. The Thevenin equivalent circuit for the human body can be approximated with a source impedance of a 100-pF capacitor in series with a 1.5-kΩ resistor [8].

In sEMG, there are two main types of electrode montages – single differential and monopolar. Merletti, Botter, and Barone designed a novel switchable montage which can be converted between single differential and monopolar [1]. The sEMG Sensor observed are a modified topology of a single differential electrode montage designed by Wang, Tang, and Bronlund [9]. This topology was chosen for its reduction of common mode voltage, and precision at low voltage measurements. Modifications suggested to the topology have been designed for the sensor to interface with digital components. The sensor's inverting Op Amp has been replaced with a limiter using 3.3V Zener diodes to protect the ADC inputs from over voltage. An optional rectifier array can be integrated into the topology to measure the envelope of the sEMG signal. Further modification could be made to this topology to implement the switchable montage. A complete schematic and analysis of Wang's circuit is shown in section 2.3

1.2.a - Electrode Types

Electrodes are loosely classified by their shape and size as well as their electrical properties. While large electrodes measure linear combinations of MUAP from muscle fiber near the electrode, small electrodes have the capability to capture individual MUAP [1]. Electrodes are furthermore differentiated resistive or capacitive based on the impedance between the skin electrode barrier.

1.2.a.1 - Resistive Electrodes

Resistive (Galvanic) Electrodes are those which conduct small currents from biopotentials which are representative of the underlying MUAP. Such electrodes must have direct skin contact during measurement, but signal integrity of these sensors is more consistent with movement, and observed signals have a much smaller signal to noise ratio (SNR). Shown below in Figure 1.3 is the representative circuit for a resistive electrode [1].
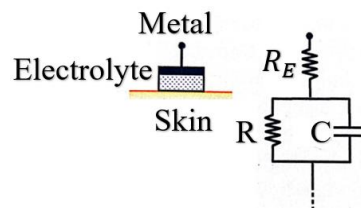
Figure 1.3: Gelled Electrode and Equivalent Circuit [1]

1.2.a.2 - Capacitive Electrodes

Capacitive Electrodes are galvanically isolated from the body; instead of measuring currents proportional to MUAP, these sensors measure a change in capacitance as muscle activity changes. A benefit of such sensors is that they can be used to measure potential without direct skin contact [10] but come with the cost of low noise immunity and small signals. Shown below in Figure 1.4

is the representative circuit for a resistive electrode. Future development of capacitive sEMG may lead to the development of wearable technologies above clothing.
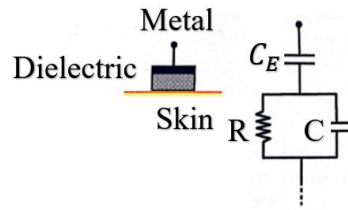
Figure 1.4: Capacitive Electrode and Equivalent Circuit [1]

1.2.b - Designing with Resistive Electrodes

In the design of this device, resistive electrodes were implemented. This decision was made despite the ability to sense over clothing, because signal integrity is essential in the design of an HD-sEMG device. Due to the low frequency noise induced by movement, small signals and high SNR, capacitive electrodes were deemed too early in their development for use in an sEMG Interfacing Development Platform [11].

1.2.c - Microelectrodes

While large electrodes induce spatial filtering through treating the surface underneath the electrode as equipotential, micro-electrodes are furthermore constrained by their spatial Nyquist Criterion. The sampling criterion shown in equation 1, states that the inter electrode distance (IED) must be the inverse of twice the highest harmonic in the signal. In this sense, the "heat map" captured during each cycle of the device contains all the information content in the signal below this harmonic [1]. It has been shown by Farina et al in Figure 1.5 that an IED of 5 mm between electrodes with a diameter of 5mm captures all information present in the forearm [1]. At an interelectrode distance of 5 mm, the sampling frequency is 200 cycles/m. This correlates to a

minimum harmonic of 300 Hz being measured on the forearm when a MUAP propagates at 3 m/s. Because most of the information content of sEMG is found below 500 Hz and specifically high information content below 60 Hz, this is an acceptable bandwidth for the electrodes.

$$f_{samp} = \frac{1}{IED} > 2f_{MAX}$$
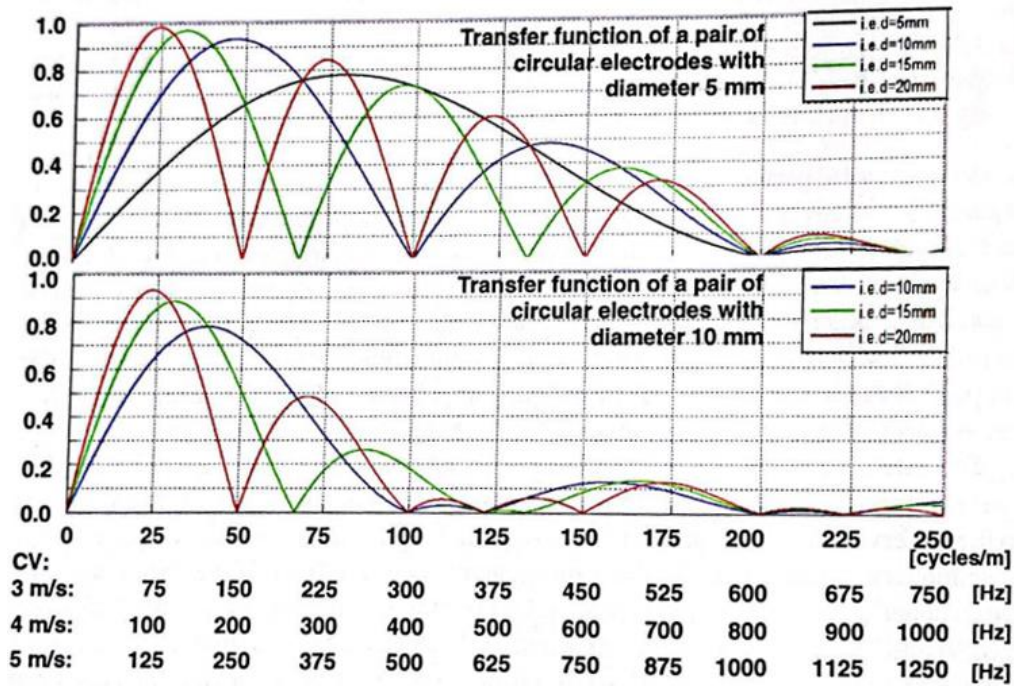
Figure 1.5: Electrode Size Transfer Functions [1]

Regarding the material properties, electrode impedance must be greater than skin impedance, but less than the amplifier's input impedance [1]. In sEMG systems, cross talk is a very important factor to consider for interelectrode distance and signal isolation. Large IED has been shown by Gallina et al to significantly increase crosstalk between sEMG sensors [12]. Crosstalk is caused by the volume conductor properties of the forearm, and thus the "blurring" it causes cannot be

negated without the use of needle electrodes, spatial filtering, or other reduction methods reviewed in literature [1, 6, 13,14].

Extraction of neuromuscular signals through HD-sEMG has been shown to drastically reduce crosstalk, alluding to the measurement of the entire forearm surface [12]. Measurement locations can be chosen through consideration of the entire forearm surface and optimized to target areas of the forearm which cause the most movement in the fingertip workspace and greatest visibility of activation patterns. Optimization of locations for signal measurement and power could be performed using k-means clustering to isolate optimal signal locations [15]. Independent Component Analysis (ICA) such as JADE [16, 17] and Blind Source Separation (BSS) to extract principal signals from electrode pairs has been shown as an effective crosstalk reduction method but requires the acquisition of an unimpeded signal such as fine wire EMG [6, 14]. Specifically in this research, sEMG is measured using seven forearm locations which were prerecorded. Considering that this device would be used by consumers, HD-sEMG is likely the best option.

While it has been shown by Jarque-Bou et al that all forearm neuromuscular control can be derived from seven locations [18], significant signal processing must be performed to do so. Furthermore, measurement above a muscle does not directly imply muscle signal acquisition. Spatiotemporal summation of motoneurons and muscle action potentials is impeded by noise and summed with other proximal muscles. Analysis using these seven sources is prone to crosstalk from multiple muscles firing under the same sEMG spot. Merletti et al have shown microelectrodes and HD -sEMG could significantly increase selectivity of muscles by sourcing multiple sensors for measurement of its MUAP activity [1].

1.3 – Muscle Force Transduction

Muscle force is generated as the summation of muscle fibers being stimulated asynchronously to produce contraction. The tension produced by the muscle sums both quantally and spatially through all motor units in the muscle, whose individual stimulus is defined as a MUAP. Using sEMG, MUAP are sensed at electrodes on the surface of the skin through volume conductor properties of the limb. The signal recorded from a sEMG sensor can therefore represent the activation of many muscles and is not a direct isolation of the electrical signal generated by a single muscle. Non linearities of EMG further abstracts the measurement of muscle force as changes in EMG are often much smaller than the associated force change at low levels and change often becomes much more volatile with activation of larger motor units [1].

Muscle response to stimulus can generally be separated into two categories - twitch and summation. A muscle twitch is defined as a single response to a single stimulus. Summation considers both the number of motor units activated -known as quantal summation and the frequency of stimulus known as wave summation. In wave summation, repeated stimulus at a frequency higher than the relaxation threshold for the fiber causes stimuli to add to the tensile force developed by the previous twitch. Tetanus is high frequency summation such that the twitch responses fuse into a smooth contraction as seen in vivo. This is to say that EMG analysis is primarily performed in the frequency domain, and that the rate of stimulation is related to forces developed.

Muscle contraction can be divided into two subtypes based on the length change of the muscle. Isometric contractions are those which cause no length change in a muscle, while isotonic are those which do cause length change. Isotonic contractions are subdivided based on the direction of length change. Eccentric contractions lead to an increase in length and are caused by the load applied to

the muscle being greater than the force generated by the muscle. Concentric contractions are those which cause a decrease in length of the muscle from the force generated being greater than the load. Such distinction is important as different types of contractions require various experimental setups. Different types of muscle contractions require various experimental setups and can result in different effects on joint angles and muscle activation, which should be taken into consideration when analyzing muscle activity.

Muscle force generation is influenced by several factors, including the length-tension relationship, force-velocity relationship, fatigue, and the balance between agonistic and antagonistic muscle groups. The length-tension relationship describes how the length of a muscle fiber affects its ability to generate tension. If the sarcomeres within the muscle fiber are too short or too long, nonlinearities in force generation can occur. The force-velocity relationship describes how muscle velocity and force are inversely related, meaning that a muscle cannot generate high force and high velocity at the same time due to a power ceiling. Fatigue occurs when ATP stores in the muscle deteriorate, leading to a decrease in the force generated over time [3]. Finally, neural control is important for coordinating the activation of both agonistic and antagonistic muscle groups, which is achieved through reciprocal innervation of bilateral pairs by sensory neurons [1].

In summary, the tension generated by a muscle force is guided by complex relationships between various factors such as length and tension, force and velocity, and fatigue and force. Additionally, factors such as optimal filament overlap, power ceiling, and reciprocal innervation of agonistic and antagonistic muscle groups also contribute to the generation of muscle force [2]. Algorithms for muscle force transduction must consider the relationship between EMG and the firing pattern of motor units in targeted muscles as well as the kinematics and dynamics of the musculoskeletal system. Specifically in the case of an sEMG system, sensitivity and selectivity of sensors also becomes a factor of increasing importance in small and deep muscles. While it has been shown that HD - sEMG drastically improves the selectivity of muscles [12], this research does not directly investigate methods for isolating muscles in HD -sEMG. Instead, this research assumes that sEMG signals capture the muscle directly underneath an sEMG sensor with little interference from nearby muscles and compares their envelopes to joint angles in order to observe gross motor function. Muscles observed are verified using volumetric models provided by the Visible Body platform [19].

1.4 - Hand Anthropometry and Functional Groups

Neuromusculoskeletal modeling (NMM) of a limb implies deriving its kinematic properties and is often used for either determining the final position and velocity of a limb because of muscular activation (forward kinematics) or determining the forces and moments present to generate a vector of observed motion (inverse kinematics) [1]. Through neuromusculoskeletal modeling, local physiology of the hand's musculoskeletal system can be integrated with muscle force transduction to observe changes in hand conformation as they relate to EMG. This conformational change manifests in joints of motion defined in the model and can be as simple as modeling open hand/grasping or as complex as the skeletal anatomy of the hand. Shown below in Figure 1.6 is

the skeletal anatomy of the hand derived into its three elementary bone types (phalanges, metacarpals and carpals). Phalanges make up the fingers, while metacarpals and carpals make up the hand and wrist respectively.
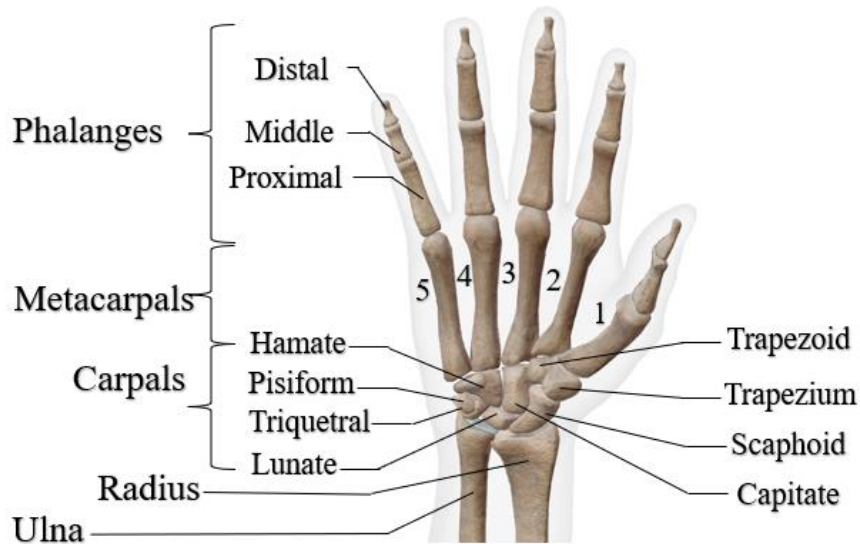
Figure 1.6: Skeletal Anatomy of Hand

The skeletal anatomy of the hand yields six different types of joints labeled by the bones which interface the joint. These joints can be furthermore abstracted to synovial joints - of which the hand has three different types. The wrist can be modeled as a condyloid joint consisting of the carpal bones, radius and ulna. The convex shape of the carpal bones interfaces with the concavity of the radius and ulna in order to allow for biaxial motion [20]. The MCP joints of the fingers as well as the MCP and CMC joints of the thumb are modeled as saddle joints. Saddle joints are biaxial and lead to the opposability of the thumb, and the ability to abduct/adduct digits II-V [20]. All IP, PIP and DIP joints are modeled as hinge joints. In hinge joints, the concave end of one bone interfaces with the convex face of another bone to create a uniaxial point of motion [20]. The joints of the hand are shown below in Figure 1.7 with their synovial analogues, marking the CMC joint of digits IV-V unlabeled as an area of contention in hand modeling.
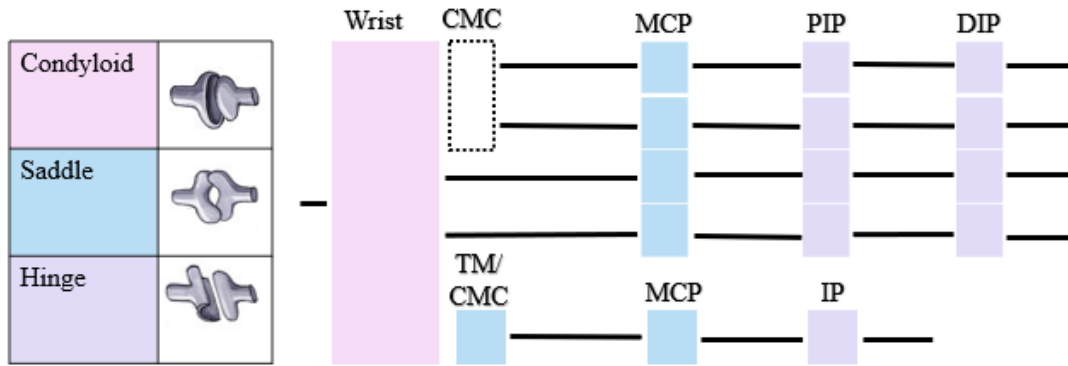
Figure 1.7: Hand Joints and Synovial Joint Models

Considering the mapping from muscles to their moments on joints in the hand, the tensile force generated by a muscle pulls the insertion on a distal bone towards its origin on a proximal bone [2]. Merletti designs the interaction between muscles and the conformation of the limb it acts on through principal vectors of tension from the origin of the muscle to its insertion on the distal bone [1]. Tensile forces of muscles counteract one another at joints, the derivation of this relation is known as its kinematics. In this derivation, a joint's axes constitute unique degrees of freedom (DOF) in the model and muscle forces change the angle at these DOF. In the language of physiology, the direction of angle change constitutes which muscles are considered flexors, extensors, or opposers (Abductors and Adductors). The functions of these muscle types are listed below in Table 1.1. DOF can either be derived using mathematical methods such as D-H parameters [21, 22, 23], or captured using a joint angle glove as discussed later in this section [18].

Table 1.1: Actions of Muscle Types

Muscle Type	Action
Extensor	Increase the angle at a joint
Flexor	Decrease the angle at a joint
Abductor	Moves limb away from midline of body
Adductor	Moves limb toward the midline of body

Functionally the hand actions originating from forearm muscles can be differentiated as shown in Figure 1.8. Ensemble flexion and extension of Digits II-V is actuated largely by the digitorum muscles and is easily measured using sEMG from the forearm. While opposition is actuated by the thenar and hypothenar muscles originating from the transverse carpal ligament, it is also actuated by the palmaris longus superficial to the flexor digitorum and deep to the bicipital aponeurosis and may therefore be measured from the forearm [24]. Further muscle groups observable from the forearm are Digit I flexion and extension, supination and pronation, and wrist actuation. Index finger extension may be observable with the use of HD-sEMG, but the muscle is deep to the forearm, and therefore the measurement of its actuation is impeded by the muscles superficial to it. Missing from this model are muscles of the hand, such as the lumbricals and palmar and dorsal interossei originating from the volar interosseous of the metacarpals and inserting into the sheaths of the terminal flexor digitorum and extensor expansions [15]. These muscles aid in fine motor control of the hand, but their measurement would be unwieldy for a subject because sensors would have to be on their hands.
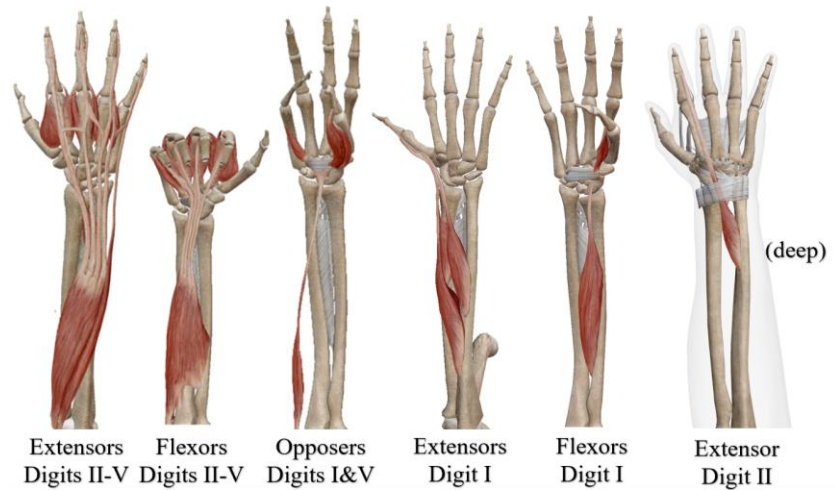
Figure 1.8: Hand Functional Groups in Forearm

A functional mapping from muscles to the joint angles which they control involves the derivation of a computational model such as that of ARMS Lab Hand and Wrist Model shown below in Figure 1.9. This is the most extensive open-source hand model available to date and integrates the BioSim framework to perform both forward and inverse kinematics on a 23 DOF model of the hand [25]. Other notable computational models for the hand include joint angle gloves, and kinematic models such as the 25 DOF model generated using D-H parameters by Peña-Pitarch et al [21, 22, 23]. This thesis did not investigate kinematic derivation for the hand, it instead shares the open-source models available for a more mechanically minded researcher to investigate. A beneficial development in this field would be integration of variant DOF models into the ARMS Lab Model.
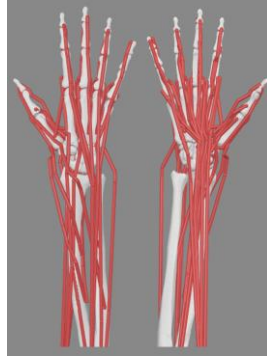
Figure 1.9: ARMS Lab Hand and Wrist Model (23 DOF) [25]

This thesis applies the 18 DOF joint angle glove measurements captured by Jarque Bou et al with prescribed hand conformations defined in the Sollerman Hand Function Test (SHFT) [26] to visualize hand conformation. sEMG signals captured in this dataset were then compared to joint angle motions to observe hand functional groups effectively measurable from the forearm. Joint-Angle or Data Gloves are a core component of hand research platforms as they can be used to track the conformation of a hand under study. Jarque Bou et al used the CYBERGLOVE II as shown below in Figure 1.10 to capture their hand joint angle data which measures the hand in 18 DOF [18, 27]. These gloves are composed of an array of sensors, supporting materials to mount the sensors on a hand, and electronics for signal processing [27,28].
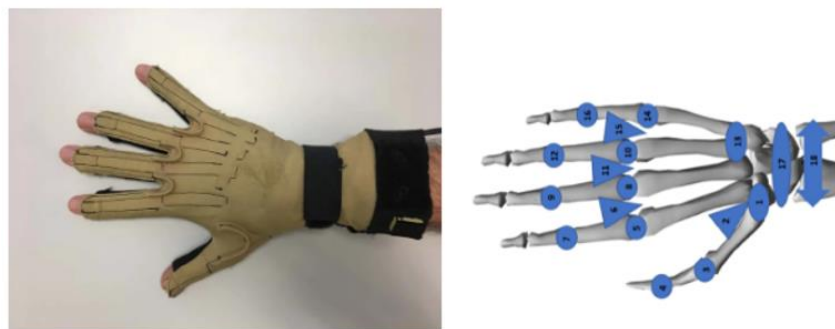
Figure 1.10: CYBERGLOVE II Joint Angle Glove (18 DOF)

In order to integrate any dataset with the ARMS Lab Hand and Wrist Model, a dataset of joint angles would need to be or cast to 23 DOF. Furthermore, the generation of a computational hand model would also involve the integration of neuromusculoskeletal modeling with the ARMS Lab Model. This would involve the targeting of muscles or functional groups, quantization of their force through methods in 1.3, coupling to the ARMS Lab Model, and derivation of forward kinematics. Implementing neuromusculoskeletal modeling within the ARMS Lab Model is significant because these models can be optimized for real time performance on embedded systems [1].

1.5 - Human Interface Device (HID)

Human Interface Devices (HID) refer to devices which use USB-HID protocol to allow a user to control a computer [29]. Historic examples of such devices are the keyboard and mouse invented in 1819 and 1964 respectively, or voice control devices such as the Amazon Alexa shown below in Figure 1.11. Such devices interface with computers by generating reports of a structure defined in the Device Class Definition for Human Interface Devices (HID) [29]. When a user clicks a key on a keyboard, button on a mouse, or speaks to a voice control device the system converts that information into a report formatted for specific HID interfaces. In this way, transactions are standardized to a single interface class, and developers can focus efforts on designing devices to existing drivers such as keyboard or mouse formats. This field of computing has seen significant development over recent years to keep up with the capabilities of modern computer systems, and the use of HID protocol enhances the generalization of such technologies to many different platforms.
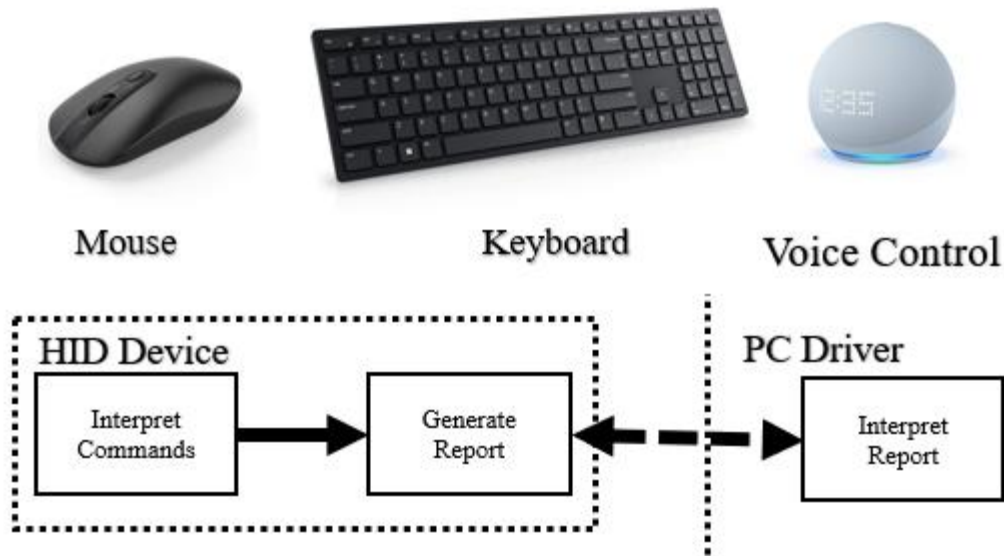
Figure 1.11: Human Interface Devices (HID)

Modern HID development has invested significant research into the anthropometry of the human body. Devices such as joysticks and mice take the conformation of the hand into account when designing grips, while three-dimensional interface devices such as the Oculus and head up displays attempt to merge computation with dynamic motion of the body and the ocular field. The development of a neuromusculoskeletal hand model for HID would be the most advanced interfacing tool for the upper limb and would allow for users to manipulate digital objects with their fingers. HID reporting is not investigated in this research as the development of sEMG technology is still in its infancy. HID instead is regarded as a destination for such a neuromusculoskeletal model of the hand and promises an unparalleled degree of applications from hazardous chemical handling to robotic surgery and prosthetic limb interfacing.

A Neuromusculoskeletal-HID would likely emulate the driver for a computer mouse, as many of the same controls available for a two-dimensional interface apply. Three-dimensional hand location could be monitored using an accelerometer and zero point, while HD-sEMG could be

used to update the NMM and determine when a user is performing a control gesture. Control gestures could be related to computer mouse commands such as right/left click and scroll to emulate the traditional performance of a mouse. These control gestures could be simple tasks such as pinching and grasping over a threshold force, while a relaxed hand could mean no control gestures are being sent. Viable options for gesture control are discussed further in chapter 3 using the KIN - MUS UJI dataset.

1.6 – Outline of Thesis

This thesis utilized existing models of the hand, the KIN-MUS UJI dataset, and the sEMG Driven Musculoskeletal modeling of Sartori to analyze the viability of using forearm sEMG as a control interface for computing. The electrophysiology of muscle tissue and anatomy and of the arm will be studied in conjunction with the Sollerman Hand Function test and optimally recorded muscles reported by Jarque Bou in order to determine how much of the hand can be actuated by an EMG driven musculoskeletal model. Furthermore, this thesis investigated the development of an HD-sEMG sleeve with much lower inter-electrode distance than that utilized in the KIN-MUS UJI dataset.

Bottlenecks in the development of an sEMG Driven Musculoskeletal model are the sensors, EMG acquisition from specific muscles, the musculoskeletal model, linking sEMG and joint angle data to the musculoskeletal model hyperparameter tuning, and development of a data analysis platform. This thesis sought to narrow the scope of future development in this field through not only showcasing the opportunity for pinch and grasp detection within open-source datasets, but also through investigation of open source sEMG sensors and computer architectures utilized in similar research. The thesis concludes with the development of Microelectrode Preamplifiers which can be used to make a sensor grid smaller than that utilized in the KIN-MUS UJI dataset.

While these sensors can be utilized to capture similar recordings to Jarque Bou, further investigation of the fingertip workspace may require a smaller inter electrode distance to spatially sample the forearm at a higher resolution. All applications discussed in this thesis are available through the associated GitHub repositories listed in the appendix of this thesis.

This research aims to show applicability of the KIN - MUS UJI dataset for study of the ARMS Lab Hand and Wrist Neuromusculoskeletal Model, along with developing a review of applicable technologies to recording forearm HD - sEMG. This research has application in robotic medicine, space missions, computer interfacing, and any task in dangerous environments where precise hand control is needed. Neuromusculoskeletal modeling is a highly interdisciplinary field at the cutting edge of biomedical research, and therefore requires the cumulative effort of its researchers to make advances. The dissemination of this work coincides with seven years of personal work on this topic and the hope that future efforts will be expedited by its development.
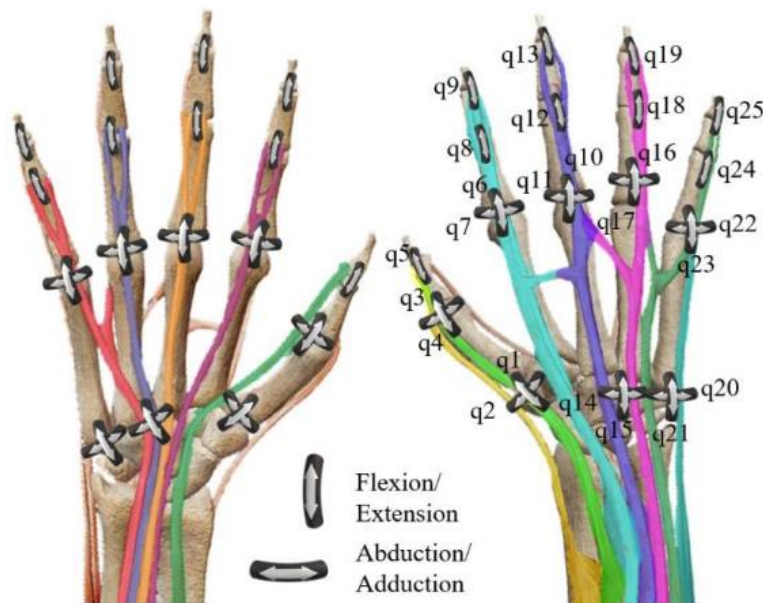
Figure 1.12: Artist Rendering Forearm Muscular Control of Hand

Chapter 2 - Review of Literature

2.1 - Sollerman Hand Function Test (SHFT)

The Sollerman Hand Function Test (SHFT) is a physiologic assessment used to measure the ability of the hand [26]. The test consists of a prescribed apparatus and observes a subject performing tasks on the apparatus. The level of detail described in the tasks of this test allows a physician to compare subjects based on their ability to perform them. The SHFT was used to observe hand motion during this study due to the expectation that subjects will perform tasks through similar hand-grips if they have full limb functionality. Hand-grips describe a normal conformation of the hand, those useful to this study are shown below along with the relaxed hand in Figure 2.1.

Relaxed Hand   **Pulp Pinch**   **Five-Fingered Pinch**   **Diagonal Volar Grip**
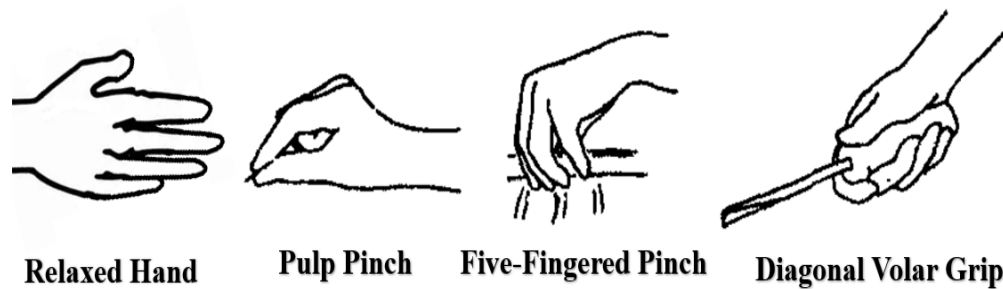
Figure 2.1: Observed Hand Conformations

Tasks of the SHFT constitute hand manipulation tasks which are used regularly and are therefore known as Activities of Daily Living (ADL). ADL of interest to this research are those which show the gradient of flexor intensity between pinches with digit II and grasps with all digits. Shown later in this research, the KIN-MUS UJI dataset is only able to capture ensemble digital flexor activity with electrodes of 20 mm IED. These ADL are namely 1,3,6, and 14 shown below in Table 2.1 reflecting their hand grip and numeral in both the Sollerman-Ejeskar test and the KIN-MUS UJI

dataset [18, 26]. These ADL are chosen to illustrate the gradient between a pinch and a grasping task.

Table 2.1: Relating KIN - MUS UJI ADL to SHFT ADL

ADL (JB)	ADL (SE)	Description	Hand-Grips
1	2	Collecting a coin and putting it into a change purse	Pulp Pinch
3	4	Removing the coin from the change purse and leaving it on the table	Pulp Pinch Five-Finger Pinch
6	7	Taking a screwdriver and turning a screw clockwise 360° with it	Diagonal Volar Grip (Supination)
14	11	Taking a knife with the right hand and a fork with the left hand and splitting a piece of clay (sitting)	Diagonal Volar Grip (Opposition)

Each ADL begins from a relaxed hand and conforms to the desired hand-grip to manipulate the object in the activity. After the activity has been performed, the subject returns to the relaxed hand conformation. ADL 1 and 3 are likely to use Pulp Pinch to pick up coins, while ADL 3 is also likely to use the Five-Finger Pinch if the location of coins is unknown in the purse. Similarly, ADL 6 and 14 will utilize the Diagonal Volar Grip to manipulate their objects but will vary in the use of the grip for force generation. ADL 6 utilizes the Diagonal Volar Grip to hold on to a screwdriver, while supination muscles are used for force generation. ADL 14 uses the Diagonal Volar Grip to directly oppose the force generated by cutting clay with a knife. The four ADL activities show an increase in dexterous force as first more fingers are recruited, then more force is generated by the ensemble in opposition to forces acting against the hand closing.

2.2 - KIN-MUS UJI and RAW_EMG Datasets

The Jarque Bou Dataset referenced refers to the "KIN-MUS UJI" and "RAW_EMG" Datasets included in "A calibrated database of kinematics and EMG of the forearm and hand during activities of daily living". It is a collection of 22 subjects performing modified tasks from the SHFT while measuring both sEMG activity and joint angles of the hand. Joint angles are recorded in 18 degrees of freedom and captured at 100 Hz by the CYBERGLOVE II. The sEMG was collected using SX230 electrodes placed over seven optimal recording locations for the forearm as shown below in Figure 2.2 [18]. The sEMG signals are recorded using an 8-channel sEMG Biometrics Ltd device with a sampling frequency of 1000 Hz. This dataset was chosen because of its high-quality kinematics acquisition, recording of sEMG measurement locations, and segmentation of data into reaching, manipulation of objects, and their release.
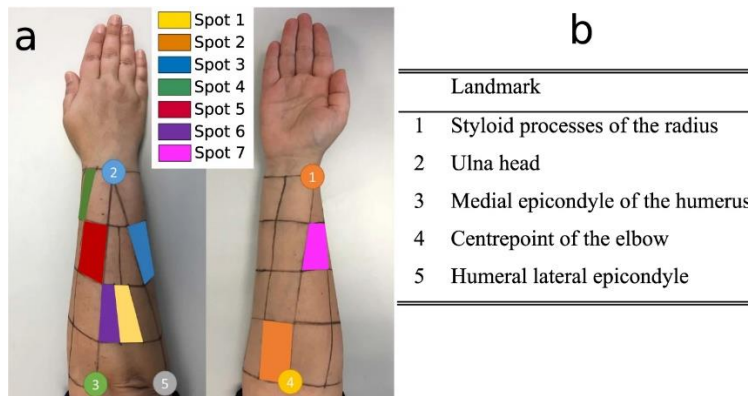
Figure 2.2: Optimal sEMG Recording Spots

Actions with the largest contribution to each sEMG spot are shown below in Table 2.2. Notably, fingertip workspace actuation is only visible from spots 3-5 in this dataset, while all others measure wrist actuation. Consequently, bilateral control of the wrist and ensemble finger motion are the only actions visible. Thumb extension is measurable from spot 4, but spot 3 measures flexion for

both the thumb and digits II-V. Electrode three is noted to be positioned on the dorsal side of the interosseous crest since the hand has a limited number of muscle bellies on the dorsal side of this region, and most of the activation group is present on the palmar forearm.

Table 2.2: sEMG Spot and Associated Action

Spot	Actions of Muscles Identified by Jarque Bou
1	Wrist Flexion & Ulnar Deviation
2	Wrist Flexion & Radial Deviation
3	Flexion I-V
4	Extension I
5	Extension II-V
6	Wrist Extension and Ulnar Deviation
7	Wrist Pronation, Supination, Extension

Though opposition of digits I&V is largely actuated by muscles originating from the transverse carpal ligament and inserting distally on the hand, it may be visible in a subset of subjects through measurement of the Palmaris Longus muscle. The muscle originates from the medial epicondyle of the humerus and inserts to transverse carpal ligament and activates during oppositional tasks for stabilization of the wrist and oppositional muscles. The Palmaris Longus may be visible from spot 2, but abstracting these are orders of signal magnitude and some subjects lack a Palmaris Longus. The presence of the Palmaris Longus varies more than any other muscle in the body and can be missing in 1.5% to 63.9% of populations around the world [24].

Another important consideration of this dataset is that because the signals are sEMG, the crosstalk between signals is significant. Muscles may be measurable from more than one sEMG spot, and this needs to be considered when studying the relationship between sEMG and joint angles. Not only does measuring EMG from the surface of the skin induce volume conductor interference as current travels through the forearm to the sensor, but these signals then sum at sensors [1]. Due to this it is not likely that small or deep muscles will be measurable, but instead that the largest movements induced by forearm muscles in the fingertip workspace will be visible with minor interference.

Two subsets of the dataset are utilized during this thesis: namely "RAW_EMG" and "KIN-MUS UJI". These two datasets measure raw sEMG and rectified integrated sEMG with joint angles respectively. Each subset records 22 patients performing 26 ADL. Included in the repository discussed later is a script for concatenating the two datasets signals together for comparison. This allows for comparison of frequency domain characteristics captured only in the raw sEMG to be compared to the joint angle data implemented in KIN-MUS UJI.

The "RAW_EMG" dataset constitutes the raw sEMG recordings for each of the seven spots. This is recorded for 22 patients performing 26 ADL. Signals are sampled at 1000 Hz. No segmentation is performed by object manipulation in this dataset, there is one signal per spot per recording. The "KIN-MUS UJI" data set comprises rectified and integrated envelopes of the seven sEMG recordings as well as the 18 joint angles recorded by the CYBERGOVE II. This dataset resamples the enveloped sEMG to 100 Hz so that it is coordinated with the joint angle data. Furthermore, this dataset is also abstracted by segmentation around the time of object manipulation. Each subject's ADL are segmented into three recordings for pre, during, and post object manipulation.

While the authors briefly mention the validation of their methods by stating that they used standard procedures for data collection and calibrated the data with known physical values, they do not provide any specific details about the validation process or the results of any validation studies. The dataset was collected from a relatively small sample size of twenty-two healthy individuals, and it is possible that the kinematic and EMG data collected from this sample may not generalize well to other populations with different levels of motor ability or health status. Furthermore, sEMG data is not all normalized to maximal voluntary contraction (MVC), with the exception being spot 4 normalized to ADL 11. Researchers analyzing this dataset do not have access to the MVC measurements, which may abstract results. Most significantly, it is noted by the authors that wrist angle measurements are subject to much higher variability than those of the hand due to the design of the apparatus. This is a significant limitation to the dataset as the majority of sEMG sensors track wrist motion, while only three are dedicated to measuring actuators of the fingertip workspace.

This dataset is significant to the development of an sEMG interfacing device because it implements recording of both raw EMG and joint angles. This dataset is utilized for the purpose of determining how much of the fingertip workspace is visible using low dimensional sEMG recording. Because all flexors of the digits are visible from a single spot, the dataset provides insight into ensemble flexion of digits. Furthermore, the rectified envelope function utilized by Jarque Bou allows for similar study of sEMG to that as performed in EMG Driven Musculoskeletal Models such as those by Sartori et al [30]. EMG Driven Musculoskeletal Models use sEMG enveloping and Hill Type muscle models to determine joint moments. Because Jarque Bou implements such enveloping, the dataset offers future opportunities for Musculoskeletal Modeling of the Hand.

This dataset is significant to the development of an HD-sEMG Driven Musculoskeletal Model because it constitutes the most apparent sEMG signals measured from the forearm and coordinates them with a kinematic recording device for hand joint angles. This is the largest open-source dataset available with this breadth of information and is further notable for its recording of practical and reproducible actions through the SHFT. The largest drawback for this dataset is its use of 20 mm IED electrodes, which cause significant spatial filtering and impedes the selectivity of the sEMG sensors to specific muscles. Despite this, the dataset provides needed insight into forearm muscle control of the hand and wrist through its application of the SHFT and the CYBERGLOVE II to sEMG recordings. If it is found that the spatial sampling frequency needs to be increased to accurately track joint moments, this research also develops upon open-source HD-sEMG to develop an electrode sleeve with a higher spatial sampling frequency than that utilized in the KIN - MUS UJI dataset.

2.3 - sEMG Sensor

2.3.a - Topology

The sEMG Sensor investigated is a modified topology of the single differential sEMG sensor designed by Wang, Tang, and Bronlund [9]. Their sensor topology is shown in Figure 2.3 and analyzed further in subsequent sections. The sensor has a total gain of 2900 and a usable bandwidth of 20 Hz to 500 Hz. It consists of a preamplifier, second order high pass, second order low pass, inverting amplifier, and second order low pass filter . While the upper bandwidth of the expected signal is 500 Hz, due to the non-ideal roll off of the filter, aliasing may be present to much higher frequencies. Wang and his team made use of a (sigma)-(delta) ADC to sample the data at 2000 Hz, but only return 1000 samples per second (SPS).
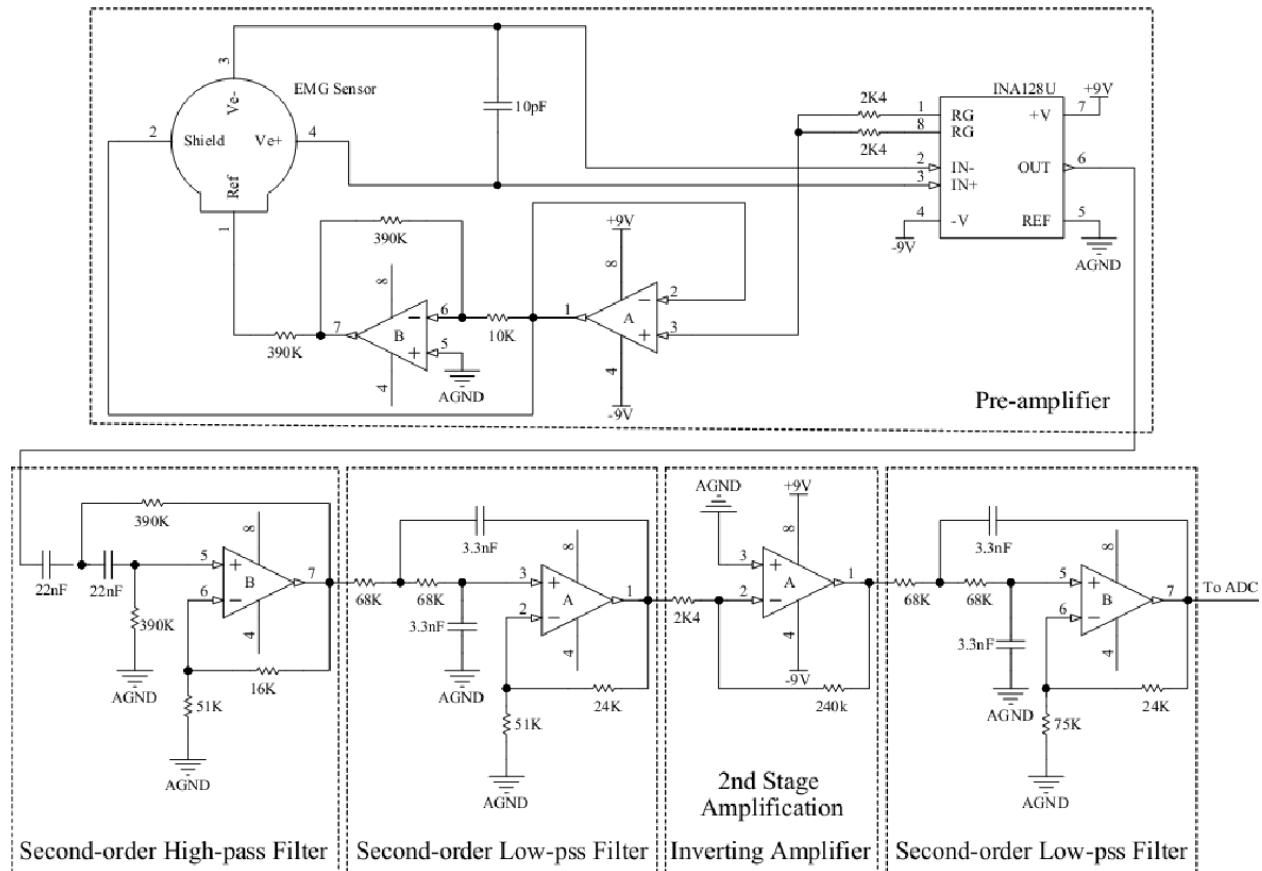
Figure 2.3: Wang et al sEMG Sensor

2.3.b - Preamplifier

The pre-amplifier in the sEMG sensor topology shown above in figure 2.3 utilized the ECG Amplifier (low voltage signal measurement) schematic from the INAX28 data sheet. Desired characteristics of this circuit are high CMRR, high input impedance, a strong DC current source, and a short distance from the electrodes. Positive and negative leads are placed on the muscle belly's origin and insertion end respectively, while the two op-amp inverter circuit is used to inject common mode input back into the body and reject it from the sensor [31]. The gain equation for the pre-amplifier is shown below in equation 2.

$$G \; = \; 1 \; + \; \frac{50 \; k\Omega}{R_G} \; = \; 1 \; + \; \frac{50 \; k\Omega}{2K4 \; + \; 2K4} \; = \; 11.4 \qquad \text{Equation 2}$$

2.3.c - Sallen-Key Filters

The filters utilized in the design of this sensor are Second Order Sallen-Key filters. While Merletti et al state that usable sEMG artifacts only extend 0-250 Hz, Wang et al designed their EMG system to capture 0-500 Hz bandwidth [9]. High pass filters are utilized in the design of this sensor to remove low frequency noise and motion artifacts, while the low pass filter removes high frequency content and noise from amplification. The high pass filter was designed with a cutoff frequency of approximately 20 Hz to remove low frequency movement artifacts from the signal; its derivation of cutoff frequency and gain are shown in equations 3-4(a). The low pass filter is designed with a cutoff frequency of 709 Hz and two are cascaded to reach the cutoff frequency of 500 Hz; its derivation of cutoff frequency and gain are shown below in equations 3-4(b).

While both fourth order and second order low pass filters were tested in this circuit, amplification changes within the pass band were not significant enough for designers to merit the implementation of a fourth order low pass filter. While Nyquist - Shannon Limit states that the sampling frequency needs to be twice the upper band limit, this upper band limit is not 500 Hz as expected with EMG. Due to the non-ideal nature of the low pass filters, the roll off past the cutoff frequency allows frequencies above the cutoff to pass to the output of the filter. This risk of aliasing was circumnavigated by the designers through implementation of a Σ - Δ analog to digital converter (ADC) which samples at 2000 Hz, but only outputs a 1000 Hz resampling of the signal [9]. In this way computational load is not increased by having the entire system run at a higher frequency, but aliasing is circumnavigated through a sufficiently high sampling rate.

$$f_c = \frac{1}{2\pi\sqrt{390K \ast 390\,K \ast 22n \ast 22n}} = 18.55\,[Hz] \qquad \text{Equation 3.a}$$

$$G_{pass} = 1 + \frac{16K}{51K} = 1.31\,[V/V] \qquad \text{Equation 4.a}$$

$$f_c = \frac{1}{2\pi\sqrt{68K \ast 68\,K \ast 3.3n \ast 3.3n}} = 709.25\,[Hz] \qquad \text{Equation 3.b}$$

$$G_{pass} = 1 + \frac{24K}{51K} = 1.47\,[V/V] \qquad \text{Equation 4.b}$$

2.3.d - Inverting Op-Amp

The inverting op amp is a topology in which there is a feedback resistor from the output to the negative input terminal. The inverting op amp in the sEMG sensor is utilized as a second amplification stage. The gain of the amplifier is set to -100 as shown in equation 5. It was found that most of the noise induced by this amplifier was high frequency power line interference, therefore a low pass filter was utilized after the amplifier to reduce this.

$$\frac{V_{OUT}}{V_{IN}} = -\frac{240K}{2.4K} = -100\,[V/V] \qquad \text{Equation 5}$$

2.4 - Hill-Type EMG Driven Muscles

Using Hill Type muscle models, Heine et al designed an algorithm to generate EMG driven forward dynamics of musculoskeletal geometries. This was performed in four steps as shown below in Figure 2.4, namely capturing EMG, muscle activation dynamics, muscle contraction dynamics, and computation of moment arms within the geometry. This algorithm has been verified by several groups including Sartori et al, Heine et al, and Kong et al [30, 32, 33]. Furthermore, this algorithm requires the development of a musculoskeletal model of the target limb - such as those shown in section 2.5. Several research groups have shown that such models can be implemented using sEMG but is limited to major superficial muscle groups [1, 34-37].
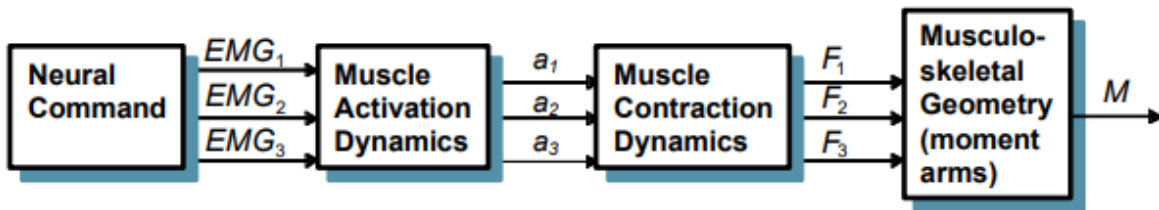
Figure 2.4: Forward Dynamic Neuromusculoskeletal Modeling [32]

Figure 2.5 below outlines the process of converting raw EMG into a signal representative of the muscle activation dynamics related to that signal. To transform the EMG into this envelope, the signal must be full wave rectified, low pass filtered at 4 Hz, and transformed by activation dynamics & nonlinearization. This process provides a signal representative of muscular activation related to the EMG signal measured. All steps are implemented digitally in this research except for EMG acquisition, though analog rectification is discussed in section 6.4.
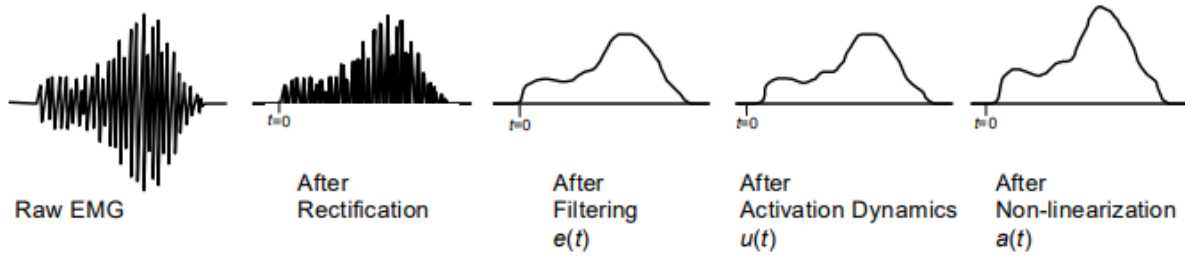
Figure 2.5: Muscle Activation Dynamics [32]

After EMG was rectified and filtered, it was transformed to represent the activation dynamics of the muscle. The transform was assumed to be a critically damped second order differential system, and its discretized form is shown below in equation 6. The transformation from rectified filtered signal can be described as a function of three parameters, γ_1, γ_2, and d which were initially guessed as 0.5, 0.5, and 40 mS and then refined later. The coefficients α, β_1, and β_2 are coefficients for the second order differential system, while d represents the electromechanical delay of the system.

$$u(t) \; = \; \alpha e(t - d) \; - \; \beta_1 u(t - 1) \; - \; \beta_2 u(t - 2) \qquad\qquad \text{Equation 6}$$

Coefficients β_1, and β_2 are functions of γ_1, and γ_2 which can be evaluated using equations 7 and 8 on the next page. After β_1, and β_2 have been calculated α can be evaluated using equation 11. β_1, and β_2 are constrained further by equation 9 and 10. These coefficients are updated iteratively after estimated joint moments are compared to actual joint moments.

$$\beta_1 \; = \; \gamma_1 \; + \; \gamma_2 \qquad\qquad \text{Equation 7}$$

$$\beta_2 \; = \; \gamma_1 \; * \; \gamma_2 \qquad\qquad \text{Equation 8}$$

$$|\gamma_1| < 1 \hspace{5cm} \text{Equation 9}$$

$$|\gamma_2| < 1 \hspace{5cm} \text{Equation 10}$$

$$\alpha - \beta_1 - \beta_2 = 1 \hspace{4cm} \text{Equation 11}$$

After activation dynamics are evaluated, the nonlinear musculoskeletal activation can then be computed using equation 12 below. This transformation is shown pictorially as the fitting from neural activation to logarithmic muscle activation shown in Figure 2.6 below. Coefficients d, c, m, and b refine the nonlinearity of low EMG amplitude, and can be evaluated as a single point on the "A-Line" shown between points P and O. Point P represents the translation from neural activation to muscle activation reported for the biceps brachii by Woods and Bigland-Ritchie, while point O represents a completely linear relationship between activations [32]. Sartori et al has shown that by learning a single distance A between point O and point P, the nonlinearity of EMG to muscle activation can be characterized much better at low amplitudes. Finding this nonlinearity was done by performing several isometric contractions and performing gradient descent to optimize A from a good starting point while keeping variation between one standard deviation of standard physiologic values.

$$\alpha(t) = d\ ln(cu(t) + 1); \ 0 \leq u(t) < {\sim}0.3 \hspace{2cm} \text{Equation 12}$$

$$\alpha(t) = mu(t) + b; \ {\sim}0.3 \leq u(t) < 1$$

Figure 2.6: Non-linearization to Muscle Activation Relationship [32]

Finding the Euclidean Distance along the A line implies finding the node point (u_0, a_0) by performing measurement of separate maximum effort isometric tasks with EMG and a load cell as described in the methods by Buchanan et al [38]. A was initialized with a value of 1.0 and a location for the node point was evaluated using equations 13 and 14. Constants M and b for the linear portion of the graph can be found by solving for the line from (1,1) to the node point, while constants d and c are solved using equations 15-18. Constant d was solved iteratively using the Euler - Cauchy method as described in [38]. As tasks are isometric, DOF remain fixed, and a(t) was the only parameter varying in the Hill muscle model.

$$u_0 = 0.3085 - Acos(\pi/4) \qquad \qquad \text{Equation 13}$$

$$a_0 = 0.3085 + A\sin(\pi/4) \qquad\qquad \text{Equation 14}$$

$$c = \frac{e^{(a_0/d)} - 1}{u_0} \qquad\qquad \text{Equation 15}$$

$$d_i = d_{i-1} - \frac{f(d_{i-1})}{f'(d_{i-1})} \qquad\qquad \text{Equation 16}$$

$$f(d) = m - \frac{dc}{cu_0 + 1} \qquad\qquad \text{Equation 17}$$

$$f'(d) = \frac{1}{u_0}\left[-1 + \left(1 - \frac{a_0}{d}e^{a_0/d}\right]\right. \qquad\qquad \text{Equation 18}$$

After muscle activation was calculated, force could then be described by equation 19 below. This equation evaluates time varying musculotendon force ($F^{mt}(t)$) as a function of normalized force-velocity ($f(v)$), active and passive normalized length dependent fiber force ($f_A(l)$, $f_P(l)$), activation (a(t)), maximum isometric muscle fiber force (F_0^m), and length dependent muscle fiber pennation angle ($\Phi(l)$). The activation a(t) was described above in equations 12-18, while force-length and force velocity curves have been described by Zajac et al [39]. The pennation angle as a function of muscle length was described by Scott and Winter [40]. Muscle forces are computed all at once for the model, as each muscle force has an impact on the pennation angle of all other muscles in the model.

$$F^{mt}(t) = F^t = \left[f_A(l)\, f(v)\, a(t)\, F_0^m + f_p(l)F_0^m\right]\cos(\Phi(l)) \qquad \text{Equation 19}$$

To compute joint moments and fiber lengths, a musculoskeletal model was needed. The equation above also implements an improvement to the optimal fiber length as shown below in equations 20 and 21. Equation 7 describes the percent difference in optimal fiber length over the entire range of activation (typically between 0 and 0.5). Equation 21 was used to initially calculate the length, while equation 21 was used in subsequent updates of this equation. As described in Murray and Zajac et al, the musculoskeletal model used must be capable of producing musculotendon lengths [39] to properly interface with the Hill - Type muscle force computation model. Heine also used Murray et al's initial values for optimal fiber length, tendon slack length, maximal muscle force, and resting pennation angle. Joint moments are computed as the sum of musculotendon forces multiplied by their respective moment arms [32]. Heine computes moment arms using equation 22, this method is the tendon displacement method described by An et al [41].

$$l^m_{0-new} = l^m_0(\delta(1 - a(t)) + 1) \qquad \text{Equation 20}$$

$$l^t = l^{mt} - l^m cos(\Phi) \qquad \text{Equation 21}$$

$$\gamma(\theta) = \frac{\sigma l^{mt}(\theta)}{\sigma \theta} \qquad \text{Equation 22}$$

Optimization was performed by minimizing the squared error between predicted joint moments and physical joint moments as shown in equation 23. Physical joint moments are measured through application of load cells, a joint angle glove, or other DOF marker. Modeled joint moments require input from both EMG and the musculoskeletal model. While tuning for A was described in the methods of Buchanan and Manal et al [38], similar optimization tasks must be performed for the hyperparameters mapping EMG envelope to neural activation (d,γ_1,γ_2). Optimization has been

shown in literature for A, d, and γ as reported in Table 2.3 with typical initial guesses and bounding

by physiological limits.

$$min \sum_{i}^{n} (M_{mod} - M_{meas})^2$$

Table 2.3: Hyperparameters in Hill Type Muscle Model

Parameter	Range	Initial Guess
A	$0 \leq A \leq 0.12$	0.1
d	$10 \leq d \leq 100$	40
γ_1	$|\gamma_1| < 1$ & Equation 9	0.5
γ_2	$|\gamma_2| < 1$ & Equation 10	0.5

Hill-Type muscles are observed in this thesis because their activation stage closely resembles

the 8 Hz filtration and rectification method used for enveloping sEMG by the KIN-MUS UJI

dataset. Hill-Type Muscles are utilized in the ARMS Lab Model, Sartori Model, and can be used

to simulate joint moments with a high degree of precision while needing to optimize relatively few

hyperparameters. While force transduction and moment computation have not been analyzed in

this thesis, the enveloping utilized by Jarque Bou and Heine are similar enough to observe gross

motor control and determine likely muscles for implementation in a neuromusculoskeletal model.

It was noted that for such a model to be developed, not only must the anthropometry of the hand

and forearm be modeled, but also origin and insertion of each muscle in the model, their pennation

angle, respective torques on different joints, and how the conformation of the hand impacts the

maximum force of muscles. Using the work of Heine et al, muscles can be simulated in a neuromusculoskeletal model such as theirs depicted below in Figure 2.7.
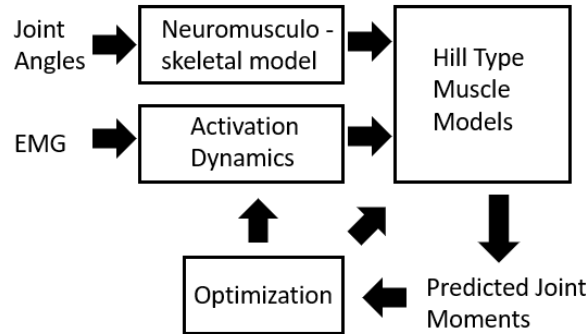
Figure 2.7: Heine Neuromusculoskeletal Model

2.5 - Hand and Wrist Models

2.5.a - 25 DOF Model

Currently, the most advanced computational model of the hand uses 25 DOF [21, 22, 42]. Using this model, the location of the fingertips can be described by multiplying a vector of hand joint angles by the product of two matrices – one which defines the movement of each finger locally, and one projecting these local finger movements into the global workspace of the hand. Because of the unanimity of this model, it is used throughout 2.5 as a reference tool for which DOF of the hand are observed in different models. The 25 DOF model of the hand is shown below in Figure 2.8.

Pitarch designs this hand model to include 25 DOF in the hand, the wrist in this model contains a further 2 DOF. The model defined flexion/extension for all IP joints of digits I-V. Flexion/extension and abduction/adduction has been modeled for all MCP joints as well as a CMC joint for the thumb, digit IV and digit V. While Pitarch does not include a wrist in his model, he does show how one could be implemented using D-H parameters similarly to other joints in the

model [21, 22, 43]. Because a wrist was included in the 25 DOF model of Peña-Pitarch, a wrist has been included in Figure 2.8.
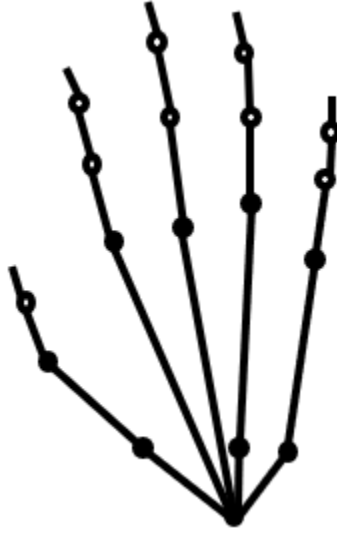
Figure 2.8: 25 DOF Model

As this model includes Digit I MCP and two oppositional DOF for digit IV-V, it was promising for the simulation of oppositional tasks and the end locations of digits IV-V. Furthermore, this model was extensively designed in literature, and is opportune for the design of an EMG driven Musculoskeletal Model from first principles. An important consideration of this hand model was that there are no muscles associated with it. This was a significant drawback because joint moments are dependent on parameters such as muscle tendon length, pennation angle, and the origin/insertion of the muscle. Therefore, for this model to be utilized for an EMG driven Musculoskeletal Model it must be developed to include muscles.

While this model was the most advanced anthropometric projection of the hand currently available, the lack of a musculoskeletal model means that it was not a viable option for this research. Pitarch states that in future research this model will be developed into a complete

musculoskeletal model. For researchers interested in the continuation of this project, Pitarch's work may be useful in the application of D-H parameters to describe hand motion, forward and inverse kinematics. Until this model is developed to include muscles, it cannot be used to develop an EMG Driven Musculoskeletal Model.

2.5.b - 18 DOF MODEL (CYBERGLOVE II)

The 18 DOF hand model implemented by the CYBERGLOVE II was utilized in the KIN-MUS UJI dataset for kinematic feedback [18]. This model implemented PIP and MCP flexion and extension of digits II- IV like the model implemented by Pitarch et al. It differs in implementation of digit I, digits II-IV abduction/adduction, the conformation of digit IV-V opposition to digit I, and this model does not implement PIP actuation. This model only implements three angles between digits II-IV and not the individual joint abduction and adduction as in Pitarch's model. Furthermore, while Pitarch's model implemented four DOF for digits IV-V opposition, this model only implemented one angle of flexion as shown below in Figure 2.9.
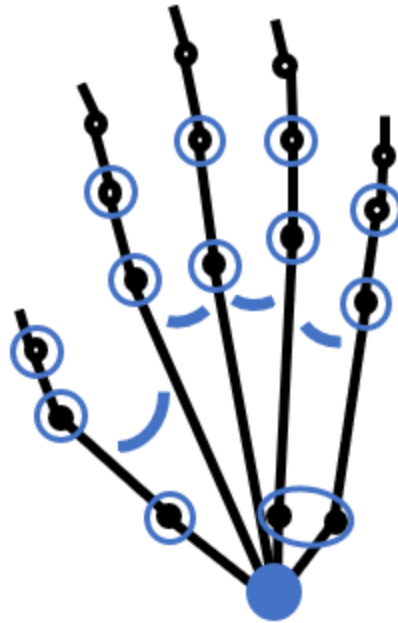
Figure 2.9: 18 DOF Model

The Cyberglove II is a joint angle glove which measures fingertip joint angles in 18 DOF at 100 Hz. The device is wireless and has sensor resolution of less than one degree. Jarque Bou used this glove for measurement of joint angles in the KIN-MUS UJI dataset. Joint angles were validated within individual studies to expected ranges of motion (ROM), yet these ROM themselves were measured with the CYBERGLOVE II. It was notable for its use in the verification of the ARMS Lab Hand and Wrist Model in two simulations, which supports its accuracy during pinch and grasp tasks and the validation procedure of Jarque Bou et al [18, 25]. An image of CYBERGLOVE II is shown below in Figure 2.10. While this glove itself was not a musculoskeletal model, its coordination with a full model allows for tracking of joint angles and moments during live data collection.

Figure 2.10: CYBERGLOVE II

2.5.c - ARMS Lab Hand and Wrist Model

The ARMS Lab Hand and Wrist Model was designed by Heine et al as an open-source kinematic hand model for the OpenSim platform. It was also notable for including all 43 intrinsic and extrinsic muscles of the hand [25]. It differs from the 25 DOF model only in that it does not implement adduction/abduction of the thumb MCP and one CMC joint for digits IV and V. This model differs from the 18 DOF model by including DIP and modeling abduction/adduction directly at MCP joints as shown in Figure 2.11. In ARMS Lab's method for verification of the model, forward dynamics and optimal control theory were used in conjunction with the CYBERGLOVE II to conform hyperparameters to the current patient under study. For this reason and the development team's commitment to making the most robust open-source model of the upper limb, the ARMS Lab Hand and Wrist Model offers the greatest opportunity to develop an sEMG Driven Musculoskeletal Model for the Hand.
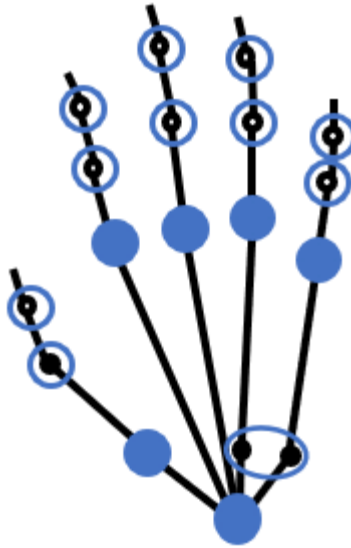
Figure 2.11: 23 DOF Model

A significant attribute of the ARMS Lab model for this research was its detailed tutorial on the simulation of pinch and grasp tasks. In their white paper on the model, ARMS Lab verified maximal pinch and grasp force estimates with two patient trials using the CYBERGLOVE II. Training of the model required input of grip force, distribution of finger forces, EMG, and joint posture [25]. While the KIN - MUS UJI dataset only measured seven sEMG signals and joint posture, the methods of the SHFT detail the object under manipulation and the typical hand conformation during its manipulation [18]. Other significant discrepancies between the dataset and this model were the use of sEMG instead of EMG and converting the 18 DOF of the CYBERGLOVE II into the 23 DOF of the ARMS Lab model.

Though ARMS Lab verified their model using the CYBERGLOVE II, no open-source conversion between these two hand models currently exists [33, 44]. A relation between the PIP and DIP angle has been defined by VanZwieten et al shown in equations 23-28 and visualized in Figure 2.12 [45]. This relationship defines the DIP joint angle as an equation of the spindle fiber

and interphalangeal angle divided by the radius of curvature on the distal end of the middle phalanx. Correlating MCP abduction and adduction angles between the two models has not been investigated but would implement similar methods.
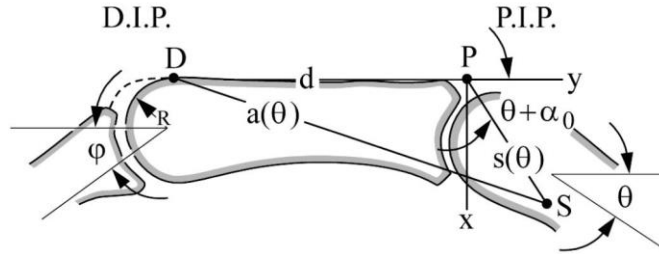
Figure 2.12: Relating DIP and PIP Angle

$$\varphi(\theta) \ = \ \frac{\sqrt{a_x(0)^2 \ + \ a_y(0)^2} \ + \ s(0) \ - \ \sqrt{a_x(\theta)^2 \ + \ a_y(\theta)^2} \ - \ s(\theta)}{R(\theta)} \qquad \text{Equation 24}$$

$$a_x(0) \ = \ s(0) \cdot sin(\alpha_0) \qquad \text{Equation 25}$$

$$a_y(0) \ = \ s(0) \cdot cos(\alpha_0) + d \qquad \text{Equation 26}$$

$$a_y(\theta) \ = \ s(\theta) \cdot sin(\theta \ + \ \alpha_0)$$

Equation 27

$$a_y(\theta) \ = \ s(\theta) \cdot cos(\theta \ + \ \alpha_0) + d \qquad \text{Equation 28}$$

The model was limited by its lack of validation datasets, modeling of passive joint properties (namely in digits IV-V) and its negation of the extensor mechanism. Due to its lack of modeling the extensor mechanism, the extensor digitorum communis (EDC) has been reported by McFarland

et al to exhibit higher activation than expected [25]. Because the model is open source, there is an opportunity for future readers to validate this model using the KIN - MUS UJI dataset. As shown through tutorial of pinch and grasp experiments, different muscles in the model can have zero, constant, and time varying activation in the same study. Through proper selection of sEMG targets and peripheral muscle activation, the KIN - MUS UJI dataset could offer 28 more validation subjects for both pinch and grasp tasks.

Correlating the Jarque Bou dataset to the ARMS Lab Hand and Wrist Model was significant for the development of a neuromusculoskeletal model of the hand because of its similarity to the validation dataset used for the model. Specifically, the Jarque Bou dataset modeled four tasks which show a variation in pinch and grasp intensity. In the ARMS Lab model these tasks are demonstrated extensively through tutorial, and therefore offer the greatest opportunity for integration of this dataset. To perform this experiment, the seven EMG spots in the KIN-MUS UJI dataset must be correlated to muscles in the ARMS Lab model. Furthermore, because digit II-V flexion and extension was only measured bilaterally through one group of electrodes in the KIN-MUS UJI dataset but actuated through a multi-body muscle in the ARMS Lab model, a relationship between these two models must be realized to complete the relationship between the two models.

Chapter 3 – Viable Gestures for Fingertip Workspace HID

3.1 – Introduction

The human hand is one of our most important tools, and its ability to perform complex movements has led to significant interest in using it to control computer devices. Human Interface Devices (HID) such as mice and keyboards have been in use for decades, but recent developments in biophysical signal modeling have allowed for the development of more sophisticated HID. One such technology, sEMG, has been used by companies like CTRL Labs for Gesture Computer Interfacing (GCI) [46]. This chapter focuses on the feasibility of using sEMG to control computer devices through hand gestures. It discusses the dataset used, in which Jarque Bou et al recorded sEMG activity of the forearm and fingertip joint angles performing the Sollerman Hand Function Test (SHFT) and explores what muscles and hand actions are visible within the dataset [18, 26]. The purpose of this chapter was to investigate viable hand gestures for the application of surface electromyographic (sEMG) technology to human interfacing devices (HID) for Gesture Computer Interfacing (GCI) specifically for extrinsic muscles of the hand in the forearm.

3.2 - Methods

3.2.a - KIN-MUS UJI Dataset

Jarque Bou investigated an original thirty sEMG recording sites on the forearm to determine seven optimal recording locations for the forearm used in the dataset [18]. Forearm regions with similar sEMG activity are shown below in Figure 3.1.a, while the final recording spots are shown in Figure 3.1.b. Figure 3.1.c shows anatomical landmarks used to locate these recording spots [18, 47]. To record joint angles in this study, the CYBERGLOVE II was utilized to record the fingertip

workspace in eighteen degrees of freedom [27]. The fingertip workspace and sEMG spots are recorded for 22 patients and 26 ADL of the SHFT. The SHFT Apparatus (a) and the CYBERGLOVE II (b) are shown below in Figure 3.2.
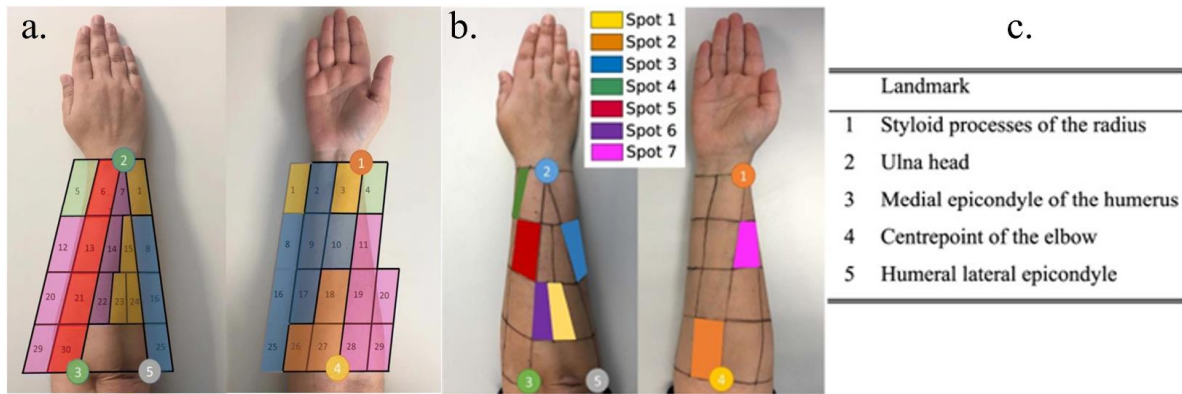
Figure 3.1: sEMG Recording Spots and Anatomical Landmarks
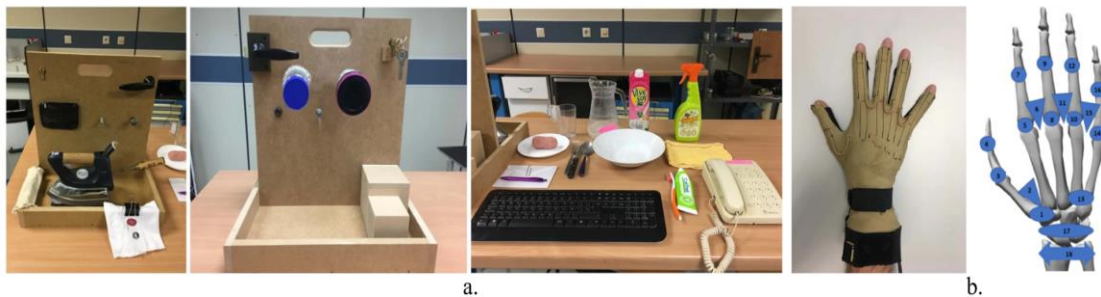
Figure 3.2: SHFT Apparatus and CYBERGLOVE II

Optimal sEMG recording locations for the forearm were identified by determining regions with similar sEMG activity using functional principal component analysis (fPCA) and locating anatomical landmarks to record joint angles [47]. While the study provided a table of expected actions causing increased sEMG activity at each spot, the actual recorded actions require the synchronization of many muscles, and the list of likely contributing muscles was not exhaustive. To address this, the subsequent study utilized the visual body platform to perform an exhaustive

analysis of the muscles under these spots. This enabled a complete musculoskeletal model of the limb to be investigated while discerning the likely muscles under each spot.

3.2.b - Actuation of the Fingertip Workspace

Joint angles between bones are controlled through bilateral pairs of muscles producing contractile forces opposing one another at the joint. Moment arms are perpendicular linearizations of rotational force which a muscle contributes to an axis of rotation. The sum of the forces opposing one another at a joint angle is known as its moment and informs the direction of angular motion caused by muscular action [1, 2, 32]. For example, shown below in Figure 3.3 is the wrist being actuated by flexors and extensors. Force generated by the wrist flexors was greater than extensors leading to the larger moment arm shown. Because the flexor moment arm was greater than the extensor, the moment caused the joint angle to decrease.
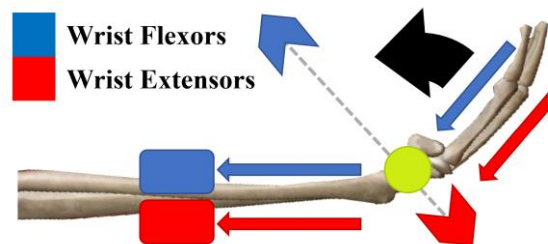
Figure 3.3: Moment Arms of Wrist Flexors and Extensors

Functionally, the hand actions originating from forearm muscles can be differentiated as shown in Figure 3.4. Sartori et al designed the interaction between muscles and the conformation of the limb it acts upon through principal vectors of tension from the origin of the muscle to its insertion on the distal bone [1, 38, 34-37]. Tensile forces of muscles counteract one another at joints, the derivation of this relation is known as its kinematics. A joint's axes constitute unique degrees of freedom (DOF) in the model and muscle forces change the angle at these DOF [36]. In the language

of physiology, the direction of angle change constitutes which muscles are considered flexors, extensors, or opposers (Abductors and Adductors) [48]. In order to compare the activation of muscles between subjects, the sEMG signals of each subject are normalized to their maximal voluntary contraction (MVC).
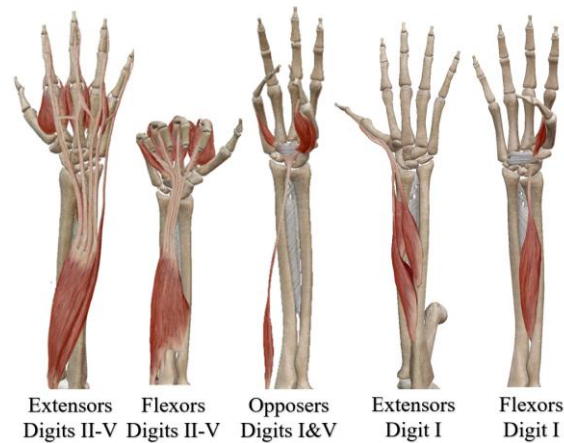
Figure 3.4: Hand Functional Groups in Forearm

Ensemble flexion and extension of Digits II-V was actuated largely by the digitorum muscles and was easily measured using sEMG from the forearm [18, 47]. While opposition was actuated by the thenar and hypothenar muscles originating from the transverse carpal ligament, it was also actuated by the palmaris longus superficial to the flexor digitorum and deep to the bicipital aponeurosis and can therefore be measured from the forearm [19, 43, 48]. Further muscle groups observable from the forearm are Digit I flexion and extension, supination and pronation, and wrist actuation. Index finger extension may be observable with the use of HD-sEMG, but the muscle is deep to the forearm, and therefore the measurement of its actuation was impeded by the muscles superficial to it. Missing from this model are muscles of the hand which would require cumbersome measurement devices, and muscles actuating supination & pronation as they are measured from the same spot and lack a kinematic representation in the CYBERGLOVE II.

3.2.c -Modeling of the Fingertip Workspace

To model the Fingertip Workspace in real time, a Musculoskeletal Model is needed to drive simulation of Musculotendon Kinematics [1]. Therefore, one of the most significant developments to fingertip workspace modeling was the creation of the ARMS Lab BioSim model [25]. While the benefit of sEMG driven musculoskeletal models proposed by Merletti et al was that they can be reduced for embedded processing [1], several stages of development stand in the way of developing a model of similar caliber to their lower body model [38, 34-37]. These stages are visualized below in Figure 3.5. Primarily, the Cyberglove II used to record joint angles by Jarque Bou et al recorded the fingertip workspace in 18 DOF, while the ARMS Lab model described the hand in 23 DOF. The conversion method between these two models is known as a Denavit-Hartenberg transformation and has not been investigated in this research [23]. Furthermore, due to the proximity of muscles within the forearm, neural drives for many actions of the hand are recorded from the same SEMG spot. This summation abstracted muscular activation, and therefore must be either differentiated into muscular activation, or used in conjunction with other signal processing methods to describe activation without direct muscular activation input. It was therefore important to the development of sEMG Driven Musculoskeletal Simulation that optimal recording sites are chosen, and that the muscles within these spots are accurately mapped to the ARMS Lab model.
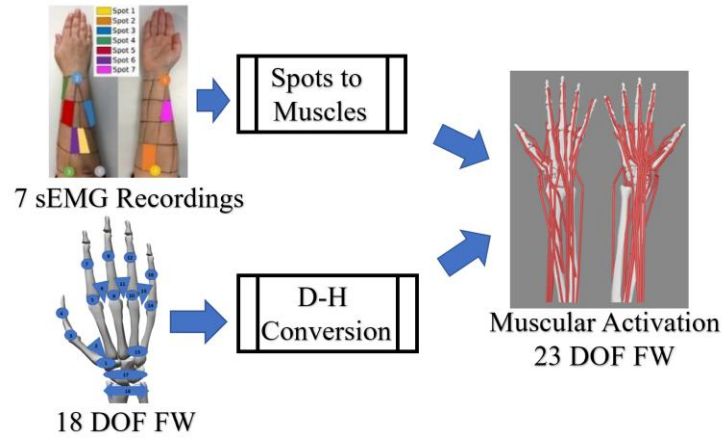
Figure 3.5: Jarque Bou Dataset as Input to ARMS Lab Model

Several other methods for further analysis of a single sEMG signal include Activation Enveloping, and Spectral Moment Analysis. Spectral moment is a statistical measure of the power distribution within an sEMG signal. As muscular activation is frequency modulated by motor neurons, spectral moment can provide insight into which motor units are active, the fatigue of motor units, and the intensity of a task. Thongpanja et al has shown correlation between median and mean frequency of the bicep and flexor pollicis longus with joint angle [49], while the differentiation between pinching and grasping hand conformations using the Jarque Bou dataset has been shown in this research through the application of activation envelopes from a single sEMG recording. While these research show that more information than activation can be obtained from low dimensional sEMG recordings, further studies are required to implement direct activation of the ARMS Lab model.

3.3 - Results

3.3.a - Neuromuscular Control - KIN-MUS UJI Dataset

In order to interpret sEMG recorded in the Jarque Bou Dataset for their relation to neuromuscular control of the hand, recording spots from the Jarque Bou Dataset were analyzed for likely muscles contributing to each sEMG signal. Jarque Bou et al proposed likely muscles which constitute most of the observed signal at each spot, these muscles are labeled with check marks in Table 3.1 below. Furthermore, because these signals have been physically identified by forearm landmarks, muscles underneath these landmarks have been labeled with an asterisk in Table 3.1 for further research into signal contribution. Volumetric models of the forearm were observed in the Visible Body platform for observation of muscles underneath electrode spots [19].

Groupings of sEMG spots are likely to record the same muscles due to the volume conductor effects of the forearm. The signal at spot 1 was stated by Jarque Bou to be largely composed of the Extensor Carpi Ulnaris [14, 47]. This made sense because it was a superficial muscle and had many motor units [19]. Cross talk at this source likely came from muscles actuating digits III-V due to its location on the forearm. Despite this, some muscles such as the APL and EPL which contribute to thumb actuation and radial adduction may also contribute to this signal. Furthermore, spot 6 which likely measured wrist extension and ulnar deviation was likely to contain artifacts of spot 1 due to the proximity of the sensors. Spots 5 and 6 were likely to record mutual sources originating near the interosseous of the ulna and radius and actuating near digit I.

Special care should be taken in the placement of electrodes at spots 5-7 due to their proximity to the brachioradialis. The muscle will cause significant interference with electrodes in this range due to its high number of motor units and proximity to the surface of the skin. Similarly, electrode

three should be placed on the dorsal side of the interosseous crest to focus the signal on digital flexors. Digital flexors are visible from spot 3 due to the hand having few muscle bellies on the dorsal side of this region of the forearm, and significant crosstalk sources were seen on the palmar forearm. Spot 2 observes wrist flexion at the origin of the digital flexors, the flexor carpi radialis is superficial, and it was therefore measured from this point.

Wrist pronation and supination can be observed from sEMG spot 7 because the muscles responsible for these movements are in the same region of the forearm and therefore have overlapping activation patterns. The pronator teres muscle is responsible for pronation (palm down), while the supinator muscle is responsible for supination (palm up). Accurately decoding the activation of individual muscles from the sEMG signal can be difficult due to crosstalk, a phenomenon where the activation of one muscle interferes with the signal of another muscle [6]. Therefore, bilateral control of supination and pronation was not visible directly within this dataset.

Through experimentation with a Myoware Muscle Sensor, it was noted that spot 3 exhibits significant interference from the Extensor Digiti Minimi [50]. Spot 3 was chosen to be placed on the dorsal side of the interosseous crest of the ulna to measure forearm flexion, yet in previous work it was shown to have a significant activation region on the palmar side of the forearm as well [51]. Further care should be taken in the placement of electrodes for spot 3 to reduce interference from extensors. Table 3.1 is illustrated in further detail in Appendix A.

While Table 3.1 outlines muscles whose activation pattern may be visible from an sEMG spot, it does not quantify the quality of that muscle's EMG in an sEMG spot signal. Accurately decoding the activation of individual muscles from the sEMG signal can be difficult, and the reduction of crosstalk between sEMG was reviewed extensively by Mesin and Talib et al [6, 14]. Signal processing methods discussed in these works are not utilized in this work for lack of validation

methods determining which muscle EMG has been separated. Although Farina discusses pure sEMG crosstalk reduction algorithms, not knowing which muscles are causing crosstalk at each spot limits investigation without actuating the ARMS Lab model or using fine wire EMG for validation [52].

Table 3.1: Muscles Under sEMG Spots; Mutual (✓), This Research (*)

Muscle	Spot 1	Spot 2	Spot 3	Spot 4	Spot 5	Spot 6	Spot 7
APL	*			✓		*	
BR				*			✓
ECRB				*	*		✓
ECRL				*			✓
ECU	*		*			✓	
EDC	*				✓	*	
EDM	*		*			*	
EI					*		

EPB				✓	*		
EPL	*		*	✓	*	*	
FCR		✓	*				*
FCU	✓		*				
FDP		*	✓				
FDS		*	✓				
FPL			✓				*
PL		✓					
PT		*					✓

Continuing from the work shown above in Table 3.1, Table 3.2 below shows the actions related with each sEMG spot. This table was notable for future use of this dataset, as it outlined bilateral pairs for finger flexion and extension in spots 3 and 5, thumb flexion and extension in spots 4 and 5, and wrist control abstracted through spots 1,2,6, and 7. Bilateral control of radial and ulnar deviation was observed through spot 2 (radial) and spots 1&6 (ulnar). Wrist flexion and extension

was controlled bilaterally through spots 1 & 2 for flexion and spots 6 & 7 for extension. This table coincided with the spot actions described by Jarque Bou [18].

Table 3.2: sEMG Spot and Associated Action

Spot	Actions of Muscles Identified by Jarque Bou
1	Wrist Flexion & Ulnar Deviation
2	Wrist Flexion & Radial Deviation
3	Flexion I-V
4	Extension I
5	Extension II-V
6	Wrist Extension and Ulnar Deviation
7	Wrist Pronation, Supination, Extension

3.3.b - Correlating Gestures to KIN-MUS UJI Dataset

Expanding upon the most likely muscles observed at each EMG spot, gestures easily differentiable using these spots would generate the greatest muscle activity in muscles directly below these sensors. Because the spots isolated bilateral wrist actuation, gestures using wrist motion are easily detectable. Digits I-V flexion was measured from spot 3, therefore bilateral control of digit I (thumb) was not differentiable from digits II-V solely through measurement of activation of these seven spots. Despite this, opening and closing the hand was grossly observable through the activation of spots 3,4, and 5. Gestures differentiable from the Jarque Bou Dataset are shown below in Figure 3.6.
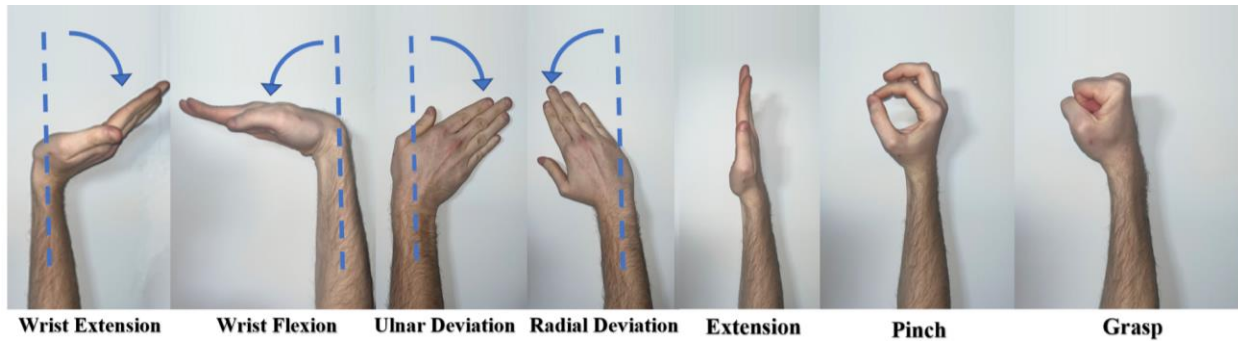
Figure 3.6: Differentiable Activation Jarque Bou Dataset

In chapter four, the variability in the activation envelope of spot 3 has been investigated. While not directly representative of fingertip joint angles, it was shown that the intensity and frequency of activation stimulus increased with the intensity of hand manipulation [49]. Manipulating lightweight targets such as coins required significantly less muscle activation than heavy targets such as weights. Variability in activation for spot 3 as shown below in Figure 3.7 provided opportunity to encode different intensity grasps due to the high degree of separation between task envelope distributions.
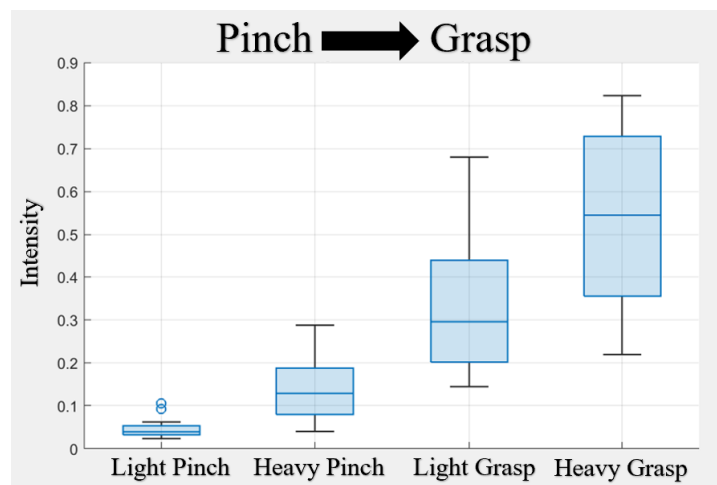
Figure 3.7: Normalized EMG Intensity Spot 3 (Digit Flexion) Pinch & Grasp

The identification of this gradient in flexor intensity between pinch and grasp tasks is significant to the utilization of the KIN-MUS UJI dataset for a neuromusculoskeletal model. Many ADL in the dataset were performed isometrically and the time under manipulation marked. Therefore, time under manipulation could be used as a calibration task for Hill Muscle hyperparameters. Then, the entire task from relaxed hand to manipulation back to relaxed hand could be simulated. An important consideration is that the KIN-MUS UJI dataset did not measure any EMG for intrinsic hand muscles. Therefore, they will need to be simulated using a priori knowledge from the SHFT, or assumptions based on joint angle motion.

3.4 – Discussion

This research showed that using the sEMG groupings in the KIN-MUS UJI dataset, bilateral actuation of the entire wrist, as well as digits II-V flexion and extension are visible. Due to sEMG spot 3 recording digit I-V flexion, bilateral control of digit I was not possible using activation envelopes supplied by Jarque Bou. Furthermore, ensemble study of digits II - V was required as digits could not be differentiated from the sEMG envelopes alone. Application of this dataset to the ARMS Lab model would require similar ensemble activation of muscles as to the nature of the recordings. Further investigation to signal composition could apply coherence, entropy, or spatial filtering methods to the sEMG to attempt a reduction of signal crosstalk [6, 14, 53]. Furthermore, muscle inferences could be contributed by joint angle change and observing activation change with the model based on weights of depth and motor unit pool size.

Gestures not differentiable within this dataset are any whose bilateral control was not observed from separate EMG spots. An example of such a gesture is a peace sign, which uses the dorsal interossei between digits 1 and II to abduct digit II, and the palmar interossei to adduct digit III. These muscles originate from the proximal side of the metacarpals and insert on the extensor

expansions and phalanges. Therefore, they are not observable from any of the seven sEMG spots. It is a good rule of thumb that abduction and adduction of digits will not be visible bilaterally due to their reliance on hand muscles. Pronation and Supination are not differentiable in this dataset using activation because both actions are controlled by muscles observable only from spot 7. While these actions would not be visible using muscle force, application of an accelerometer to an sEMG wristband would not only allow actuation of supination and pronation, but also create insight on limb conformation and three-dimensional position.

While these gestures are not part of the SHFT, actions such as pointing with digit II or digit V may be visible from sEMG data. Extensors for these digits were observed at spots 5 and 3 using the visible body software, and through observation on volunteers. Finger II extension is actuated from the extensor indicis and likely observable from spot 5, while finger V extension is actuated by the extensor digiti minimi visible from spot 3. The lack of fingertip workspace data and SHFT tasks to observe these actions limit the development of this investigation. Future work could involve directly observing these two actions to differentiate more fingertip workspace control from forearm musculature.

The GitHub link provided in Appendix B.1 is an open-source repository to aid in physiologic study of the forearm through the Jarque Bou dataset [18]. Code was designed in conjunctive research to aid in the differentiation of pinch and grasp tasks using forearm sEMG. The Fingertip Workspace Atlas is a spreadsheet containing the muscles of the forearm and hand as well as their physiologic properties within multiple models of the fingertip workspace. The purpose of this research was integration of the ARMS Lab model, Hill Type Musculoskeletal Modeling, Jarque Bou Dataset, and Lower Limb EMG Driven Musculoskeletal Models by Sartori et al to generate

an open source sEMG Driven Musculoskeletal Model of the forearm. This technology would aid in the development of Gesture Computer Interfacing.

Using sEMG Driven Musculoskeletal models for human interfacing devices implies the transduction of a computational model of the hand using information derived solely from sEMG. The analysis of the Jarque Bou Dataset in this research implied a significantly lower dimensional model than that designed by the ARMS Lab. This can be circumnavigated through conversion between models. Further investigation into signal extraction from the Jarque Bou Dataset, or an HD-sEMG sleeve could be designed to spatially sample the forearm using a smaller interelectrode distance in order to isolate more signals. Through development of such a model, insight into hand conformation could aid in assistive technologies, protecting humans from hazardous materials testing, or improve human interfacing to complex technologies.

An important consideration of this research is that Jarque Bou initially identified thirty regions of the forearm to record and reduced these thirty down to seven by finding principal signals using functional principal component analysis (fPCA). These thirty locations were recorded using electrodes with an inter electrode distance of 20 mm, and therefore induced significant spatial filtering and low selectivity. While this research showed several degrees of bilateral control are possible using seven sEMG spots, more neuromuscular control may be visible when sampling at a higher spatial resolution as discussed in crosstalk reduction methods by Gallina [12]. This would not only reduce the need for spatial filtering but may also provide more selectivity of which muscles are being measured.

Using sEMG for such interfacing devices was intuitive because the technology is noninvasive and can therefore be implemented as a wearable device not limited to laboratory study like fine wire EMG. Such sensors can be easily applied to measure large, superficial muscles up to

approximately two centimeters below the surface of the skin. Disadvantages of the technology are its nonlinear nature, noise, and the presence of motion artifacts [1]. Furthermore, due to sEMG recording electrical activity deep to the electrodes, many muscles are superimposed upon one another in each recording within the Jarque Bou Dataset. It was therefore imperative to the development of GCI that viable muscles and their respective actuation of the fingertip workspace are outlined, and the location from which they are optimally measured is discerned.

This dataset was analyzed for its implementation into sEMG Musculoskeletal Modeling of the hand and forearm. The Jarque Bou Dataset was found to measure full bilateral control of the forearm, and ensemble bilateral control of digits II-V. sEMG groups were analyzed for muscles underneath them and correlated to the actions of the muscles which were most likely to contribute to measured signals. Development of this technology was not only useful for the development of assistive technologies, but imperative to streamline the control of devices which require three-dimensional control. Limitations in this technology are discussed as they relate to the Jarque Bou dataset, and methods for further investigation of the fingertip workspace are introduced. Specifically, it is of utmost importance that crosstalk reduction is addressed so that individual muscle signals can be identified. sEMG Driven Musculoskeletal Modeling proposes that musculoskeletal actuation can be transduced as a vector of sEMG signals which can be used to biometrically encode motor control.

Chapter 4 - Differentiation of Pinch and Grasp Tasks using Forearm sEMG and Joint Angles from KIN-MUS-UJI Dataset

4.1 – Introduction

This chapter explores the use of sEMG enveloping, spectral moment analysis, coherence, and joint angle observation to differentiate pinch and grasp tasks using data from the Sollerman Hand Function Test (SHFT) dataset recorded by Jarque Bou et al. The analysis involved the use of one sEMG sensor to observe all digit flexors in the KIN-MUS-UJI dataset, making it particularly significant for the development of neuromusculoskeletal models with few inputs. By measuring envelopes, mean and median frequency, and their ratio, as well as coherence analysis of sEMG signals, this study seeks to assess muscle activation patterns, fatigue levels, and neuromuscular coupling between agonistic and antagonistic muscle pairs controlling ensemble digit motion. The chapter investigated the depth of information that could be extracted from the coordinated analysis of intensity with spectral characteristics, such as median and mean frequency and coherence, to differentiate between pinch and grasp tasks in the KIN-MUS-UJI dataset. Methods for the time frequency analysis of sEMG were largely informed from the combined works of Merletti, Lindstrom, DeLuca, Lago, Clancy, and Mesin et al [1, 14, 54-57].

4.2 - Methods

4.2.a - Experiment

Gestures within the SHFT were differentiated between pinching and grasping tasks, then sEMG was used to observe measures of activation, spectral moments, and coherence. Joint angles were observed for the ensemble average of the PIP and MCP for digits II-V, and index finger, while the

IP, MCP, and CMC were observed for the thumb. Muscle groups observed included thumb, index finger, and ensemble finger flexion and extension. Muscles were not measured directly, but instead through 7 optimal locations for forearm sEMG measurement as described by Jarque Bou [18] and shown below in Table 4.1 shown below.

As shown through previous research, many muscles overlap underneath these seven sEMG spots [18, 19, 47]. The actions associated with sEMG spots in Table 4.1 are correlated to the muscles reported by Jarque Bou to be directly below the electrodes [18]. Only spots 3,4, and 5 constituted bilateral motion in the fingertip workspace, all other recording spots measured wrist motion. Spot 3, which measured all digit flexors, was used to indicate intensity. The spectral moment and coherence analysis of the sEMG signals were used to assess the activation patterns, synchronization, and fatigue levels of the muscles involved in the pinch and grasp tasks.

Table 4.1: sEMG Spot and Associated Action

Spot	Actions of Muscles Identified by Jarque Bou
1	Wrist Flexion & Ulnar Deviation
2	Wrist Flexion & Radial Deviation
3	Flexion I-V
4	Extension I
5	Extension II-V
6	Wrist Extension and Ulnar Deviation
7	Wrist Pronation, Supination, Extension

4.2.b - Data Collection and Filtering

The dataset used in this study was designed by Jarque-Bou et all and observed the Sollerman Hand Function test through seven sEMG signals representative of all muscle activity in the forearm and fingertip joint angles recorded by the Cyberglove II [18]. This dataset was designed to aid in physiologic study of the forearm and was notable for its investigation into optimal sEMG recording and integration with the fingertip workspace in 18 degrees of freedom (DOF). SX230 electrodes were used in conjunction with an sEMG Biometrics Ltd device to collect the data with a gain of 1000. Data was sampled at a frequency of 1 kHz and had a usable bandwidth between 20 and 460 Hz. Joint angles and envelopes recorded by Jarque Bou were resampled to 100 Hz. Patients' hair was removed by shaving and skin was cleaned with alcohol before the electrodes were placed. Signal filtering was performed using a fourth order band-pass filter between 25 and 500 Hz on raw sEMG [18].

4.2.c - Enveloping and Activation

Enveloping of sEMG has been traditionally used in kinematic studies to assess the activation levels of muscles during movement. Enveloping involves rectifying and smoothing raw sEMG signal to obtain an envelope representative of the overall muscle activity. This signal can then be used to quantify the timing and intensity of muscle activation during movement. Rectification is a debated topic in EMG studies because it significantly changes the frequency spectra of the signal [1]. Low-pass filters between 4-8 Hz are commonly chosen for sEMG enveloping because they attenuate high-frequency noise and physiological artifacts while preserving the desired signal components [18, 32, 47]. Rectification converts the negative portions of the sEMG signal into positive values, resulting in a loss of phase information and spectral distortion. However, rectification can improve the signal-to-noise ratio and make the envelope signal more

representative of muscle activity [1]. In the dataset used for this study, all envelopes were normalized by a maximal voluntary contraction (MVC) experiment for comparison of sEMG activity across different individuals and muscle sites [18].

To observe the activation of muscles, two different enveloping functions were observed. The first from the Jarque Bou Dataset itself, raw sEMG was rectified and filtered using a fourth order low pass filter at 8 Hz and gaussian smoothing [18]. Furthermore, activation analogous to Hill Type Muscle activation was investigated in this research by rectifying and filtering using a 4th order Butterworth lowpass filter at 4 Hz [32]. Application of the second order recursive filter was not performed due to lack of knowledge on electromechanical delay and scaling coefficients for musculoskeletal models of the forearm [32]. While the rectified and filtered envelope was reported by Heine et al to be a poor representation of neural drive, this assessment pertains to the nonlinearities of the peaks of the envelope [32]. The application of the filter was instead used for comparison to the enveloped sEMG within the dataset.

4.2.d – Spectral Moment Analysis

Spectral moment analysis is a technique used to analyze surface electromyography (sEMG) signals in the frequency domain. It involved calculating statistical moments of the power spectrum of the sEMG signal, which provided information about the shape and distribution of the frequency content [1]. Spectral moment analysis has been used in various applications such as muscle fatigue assessment, motor unit recruitment analysis, and muscle activation pattern recognition [57]. This method can provide valuable insights into the underlying neuromuscular activity during different tasks and can complement other sEMG analysis techniques such as activation envelopes. In this section, spectral moment analysis methods are outlined for application to analyzing sEMG signals during activities of daily living (ADL).

Median Frequency is commonly used in sEMG studies as an indicator for fatigue and has also been shown by Thopanja et al to be an indicator for joint angle motion [1,49,58]. Median frequency was observed to track changes in frequency spectra of flexor sEMG with tasks of varying intensity flexion. This was done without any window overlap. The algorithm is shown below in equations 29 and 30 where total power was first calculated for each time segment (29), then power summation was reiterated until the half power point was reached (30). The median frequency vector was then regressed for the timespan in which the subject was touching the object under manipulation to observe frequency changes based on the specific ADL. This reduction of time span removed the effect of resting frequency of the muscles from the regression.

$$P_{tot} = \sum_{f=0}^{f_{max}} X^2(f)$$

Equation 29

$$\sum_{f=0}^{f_{median}} X^2(f) = \frac{1}{2} P_{tot}$$

Equation 30

The mean frequency function is another commonly used tool in sEMG studies. Mean frequency is defined as the average frequency weighted by the amplitude of the sEMG signal. It has been observed that mean frequency decreases with increasing fatigue and is often used as an indicator of muscle fatigue [1]. To calculate mean frequency, the power spectral density of the sEMG signal was first computed, followed by the determination of the spectral moments. The first moment, which is the mean frequency, is then calculated by dividing the second moment by the first moment as shown below in equation 31 [1]. Similarly to median frequency, the mean frequency vector can be regressed for the timespan in which the subject was touching the object under manipulation to observe changes in frequency related to the specific ADL.

$$f_{mean} = \frac{\sum_{f=0}^{f_s/2} f\, X(f)}{\sum_{f=0}^{f_s/2} X(f)}$$

<div align="right">Equation 31</div>

Spectral moment analysis is a powerful tool in the analysis of sEMG signals. One of its primary applications is the assessment of muscle fatigue. As muscles fatigue, larger motor units are recruited to perform the same action, and these motor units produce action potentials at lower frequencies. This leads to a decrease in the median frequency of the sEMG signal. By observing a negative slope in the regression of median frequency over time, it is possible to discern the onset of muscle fatigue. The ability to detect muscle fatigue using sEMG signals can be a valuable tool in understanding the underlying neuromuscular mechanisms involved in different tasks and activities. However, it was important to note that mean frequency is more susceptible to high-frequency interference. As a result, Merletti et al suggests using both median and mean frequency in tandem to accurately assess muscle fatigue [1].

Another application of spectral moment analysis is the assessment of muscle activation patterns in the neuromusculoskeletal system. The ratio defined in equation 32 is an indicator of spectral skew used for this assessment. Skewness of the power spectrum can be used to indicate changes in muscle fiber recruitment patterns and occurs when there is an asymmetry in the distribution of power within a frequency spectra [1]. Analyzing this ratio can provide insights into the function of the system and its response to different stimuli or interventions. In this study, spectral skew was measured using a single sEMG sensor on the forearm to gain insights into muscle recruitment patterns during reaching, manipulation, and release stages of tasks. By studying muscle activation patterns, researchers can better understand the biomechanics of different movements and develop more effective interventions.

$$r = \frac{f_{mean}}{f_{median}}$$

4.2.e - Magnitude Squared Coherence Analysis

Magnitude-squared coherence (MSC) is a frequency domain analog of a squared correlation coefficient (r2), the work of Lovett et al develops a Coherence Spectrogram (CS) which can be used to observe localized changes in coherence between two signals [53]. The algorithm involves calculating the average of a Discrete Prolate Spheroidal Sequence (DPSS) windowed MSC for every second in the signal. The CS can be interpreted as the cross spectra divided by the spectrograms of the two signals. The equations for the CS and spectrogram are shown respectively in equations 33 and 34.

$$CS[n,k] = \frac{\left|\sum_{i=0}^{L-1} X_i[n,k]Y_i^*[n,k]\right|^2}{\sum_{i=0}^{L-1}|X_i[n,k]|^2 \sum_{i=0}^{L-1}|Y_i[n,k]|^2}$$

$$S[n,k] = \sum_{i=0}^{L-1}|X_i[n,k]|^2$$

The Magnitude-squared Coherence (MSC) is a measure of the degree of coherence or correlation between two signals x and y in the frequency domain. The implementation provided first applied the DPSS window to each window of the data and then calculated the Fourier transforms of each window of the data. The input parameters for the function include the two signals x and y, sampling frequency (fs), number of data points in the FFT (nfft), and the amount of overlap between consecutive windows (noverlap). The DPSS window was applied to obtain a

set of overlapping windows, and the Fourier transforms of each window are calculated. The cross and auto power spectral densities are then computed, which are used to calculate the MSC. Here, 'i' represents the window index in the DPSS, k represents the frequency bin index, and n represents the time segment index.

The Coherence Spectrum (CS) function computes the Magnitude Squared Coherence (MSC) value for a given frequency bin k and time segment n. The MSC value quantifies the degree of coherence or correlation between two signals at a particular frequency and time. A coherence spectrogram can help visualize the coherence between the two signals at different frequencies and times. An MSC value of 0 means that there is no correlation between the two signals at that frequency and time, while an MSC value of 1 indicates perfect coherence. The phase difference between the two signals at a given frequency can also be inferred from the MSC value. When the phase difference is constant over time, the MSC value is high, indicating a high degree of coherence. However, when the phase difference varies over time, the MSC value is lower, indicating a lower degree of coherence.

Specifically, in this research the coherence between digit flexors and extensors was observed for changes in synchronization patterns during the increased utilization of hand flexors from pinch to grasp tasks. In the study of sEMG signals, coherence analysis can be performed by examining the synchronization of these signals within different frequency bands. Frequency bands are specific ranges of frequencies within the electromagnetic spectrum that correspond to different types of brain waves that oscillate at those frequencies as shown below in Table 4.2. By examining the coherence between sEMG signals within these different frequency bands, researchers can gain insights into the neuromuscular coupling between different muscle groups and their coordination during various tasks.

Table 4.2: Frequency Bands

Frequency Band	Frequency Range [Hz]
Delta	0.5 – 4
Theta	4-8
Alpha	8-12
Beta	12-35
Gamma	>35

4.3 – Results

4.3.a – Flexor Intensity during ADL

Shown below in Figure 4.1 is a box chart displaying normalized EMG flexor intensity of for all 26 ADL. Of particular interest to this investigation were ADL 1,3, 6 and 14 in which the intensity of flexion was varied controllably. In ADL 1 and 3, subjects were picking up coins on a desk, putting them in a purse, and retrieving them from the purse respectively. ADL 6 involved picking up a screwdriver, and turning a screw 360 degrees with it, while ADL 14 increased flexion force further by cutting a piece of clay with a knife.

ADL 1 and 3 were pinch tasks that required the subject to perform fine motor movements with their fingers. In ADL 1, the subject collected a coin and put it into a change purse using a pulp pinch hand conformation. In ADL 3, the subject removed the coin from the change purse and left it on the table using both pulp pinch and five-fingered pinch hand conformations. Although both tasks involved pinching, ADL 3 had a much longer object manipulation phase as compared to ADL 1. This led to a larger intensity envelope observed during ADL 3 than in ADL 1.

ADL 6 and 14 were grasp tasks that required the subject to apply a greater amount of force. In ADL 6, the subject took a screwdriver and turned a screw clockwise 360° with a diagonal volar grip hand conformation. This task therefore required both grasping and rotational forces. ADL 14 involved taking a knife with the right hand and a fork with the left hand and splitting a piece of clay while sitting. This task had the highest intensity rating and required solely grasping forces with a diagonal volar grip hand conformation.

While ADL 14 required the subject to resist forces associated with cutting clay, ADL 6 involved picking up a screwdriver and turning a screw 360 degrees with it. Both ADL 6 and 14 were grasping tasks that required different levels of grasping force. In ADL 14, the subject needed to apply a higher level of grasping force as compared to ADL 6, which involved both grasping and rotational force as the subject turned the screwdriver. ADL 14 created a maximum in spot 3 intensity due to subjects resisting friction, deformation, and cutting forces required to split the clay. The difference in the grasping force and the rotational force required in ADL 6 and 14 could potentially affect the activation envelopes seen in the sEMG signals recorded during these tasks. The activation envelopes may be different due to the difference in the required muscle activity and the involvement of different muscle groups during these tasks.
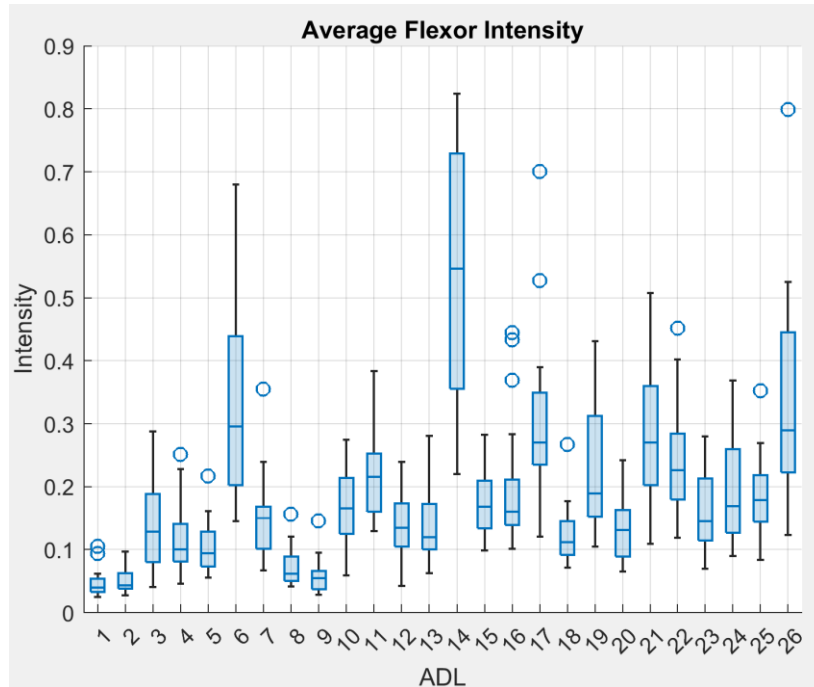
Figure 4.1: Normalized EMG Intensity of all ADL Spot 3 (Digit I-V Flexion)

4.3.b - Pinch and Grasp Excitation

Figure 4.2 displays the activation envelope reported by Jarque Bou et al and the envelopes derived using the filtering reported by Heine. As shown, the Heine envelope appears to match the shape of the Bou envelope, but the Bou envelope has had gaussian smoothing applied to it. Due to the similarity seen between the two envelopes, the envelope applied by Jarque Bou was used to observe joint angles in further investigation for this experiment.

Figure 4.2: Bou and Heine Normalized EMG Intensity Comparison

Four tasks were found to be representative of the gradient between a pinch and a grasp, namely, ADL 1, 3, 6, and 14. This was determined as these four ADL increase in envelope intensity and utilization of flexor muscles to maintain a hold of the object under mani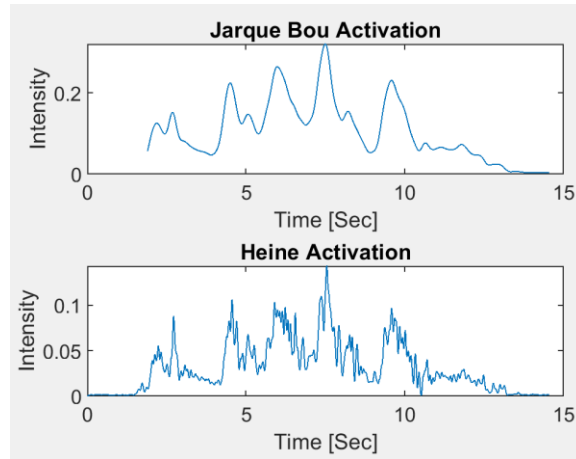pulation. While ADL 1 and 3 are similar in task, ADL 3 likely produces larger intensity measures due to the subject digging around the coin purse. Similarly, while ADL 6 and 14 both cause larger intensity than 1 and 3, ADL 14 likely causes the largest activation envelopes due to resisting the force of the knife as clay was cut.

Likely hand confirmations for these four ADL are listed below in Table 4.3 along with their relative intensity of flexor activation. Shown below in Figures 4.3 - 4.6 are individual figures showing the change in joint angles in each ADL with respect to envelope intensity. Activation envelopes for digits I - V flexion, digits II-V extension, and digit I extension were observed with CYBERGLOVE II joint angles for digit I, digit II, and an ensemble of digits II-V. Red asterisk bound the time a subject has an object under manipulation.

Table 4.3: Observed ADL Intensity

ADL	Description	Hand Conformation	Intensity
1	Collecting a coin and putting it into a change purse	Pulp Pinch	1
3	Removing the coin from the change purse and leaving it on the table	Pulp Pinch, Five-Fingered Pinch	2
6	Taking a screwdriver and turning a screw clockwise 360° with it	Diagonal Volar Grip	3
14	Taking a knife with the right hand and a fork with the left hand and splitting a piece of clay (sitting)	Diagonal Volar Grip	4

Shown below in Figure 4.3 are the MCP and PIP for digit I, digit II, and an ensemble average of digits II - V along with the activation envelopes for digits I-V flexion, digits II-V extension, and digit I extension for ADL 1. ADL 1 involved collecting a coin and putting it into a change purse. Observing the activation envelope for digit I flexion, it is noted that there are two pulses which occur before the subject grasped the coin. Furthermore, there was a decrease in intensity of all fingertip workspace actuators from the point the coin was touched to the point that it was placed in the purse. There are similar pulses observed in both digit I extension and digit II extension.
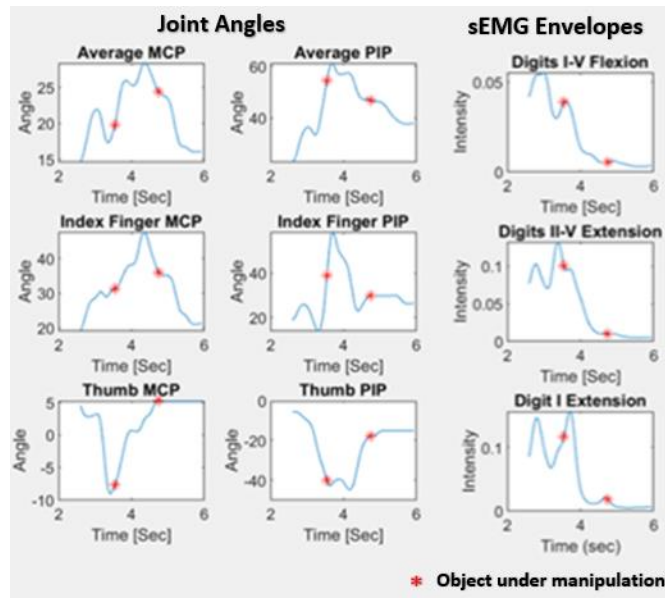
Figure 4.3: Subject 1 ADL 1 (Pulp Pinch)

Figure 4.4 displays the same parameters in the hand model as those in Figure 4.3, but for ADL 3. ADL 3 involved removing the coin placed within the coin purse and leaving it on the table. It was noted that there was much higher intensity sEMG observed in this experiment, and that there were several pulses of flexor intensity while the subject was holding on to the coin. It was further noted that in this experiment, digit II-V extension became tetanized with high intensity. There was much more volatility in the joint angle motion for this ADL.
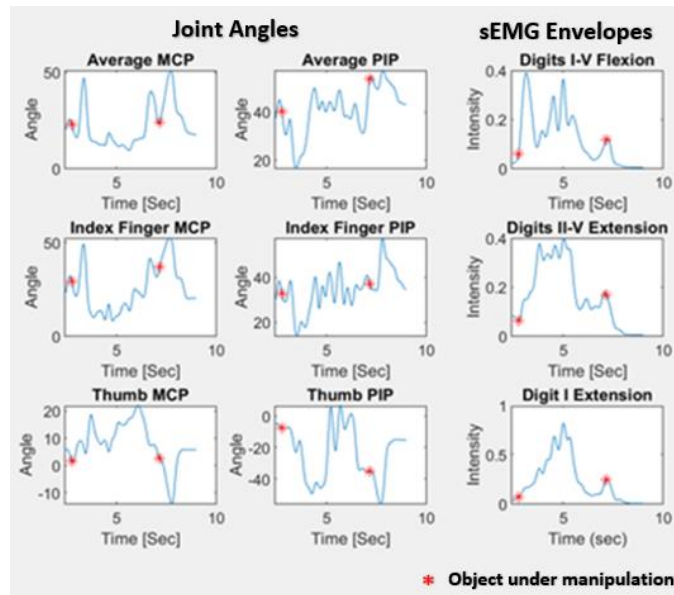
Figure 4.4: Subject 1 ADL 3 (Pulp Pinch/ Five-Fingered Pinch)

Shown below in Figure 4.5 are similar joint angle and intensity data to previous experiments for ADL 6. ADL 6 involved taking a screwdriver and turning a screw 360 degrees with it. All sEMG appeared to tetanize in this experiment, and joint angles fluctuated rapidly. Notably, four pulses appeared in the stimulation of the three observed sEMG spots. Observing the average PIP and digit II PIP, these pulses were visible as quick fluctuations in joint angle as the subject twisted the screwdriver. Intensity of sEMG did not settle to zero in between pulses, suggesting that force was used to oppose the pulses generated in antagonistic muscles.
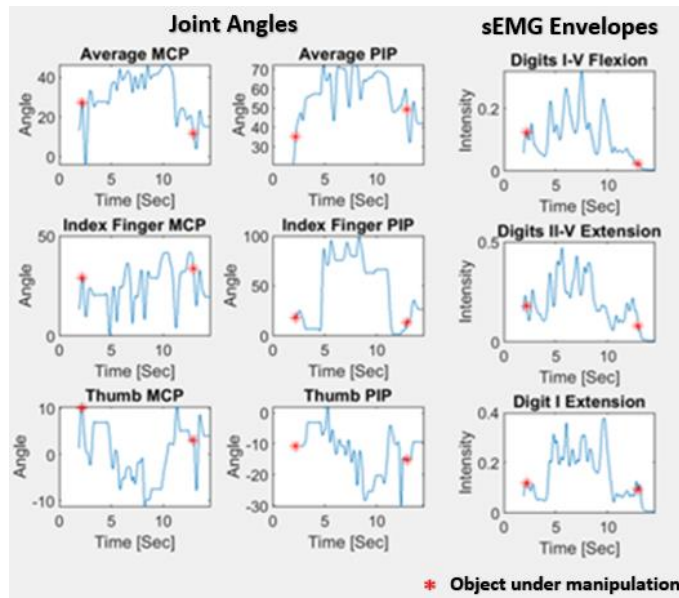
Figure 4.5: Subject 2 ADL 6 (Diagonal Volar Grip)

Shown below in Figure 4.6 are the markers for fingertip workspace and sEMG intensity for ADL 14. ADL 14 involved taking a knife with the right hand and a fork with the left hand to split a piece of clay while sitting. This ADL involved significant force and control of the knife, this control was reflected in the frequency and amplitude of stimulus observed in sEMG intensity. Joint angles were held nearly constant with minor fluctuations for stabilization and adjustment of grip.
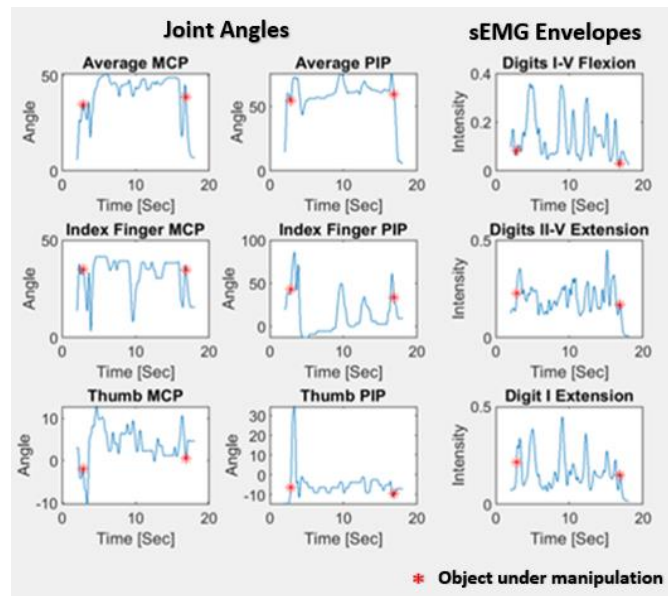
Figure 4.6: Subject 1 ADL 14 (Diagonal Volar Grip)

4.3.c – Spectral Moment Analysis

Shown below in Figure 4.7 are the spectral moment markers for flexors for digits I-V during ADL 1 with time the subject was manipulating a coin linearly regressed. Median and mean frequency while the coin was being held are roughly 70 and 90 Hz respectively but fluctuated more right before the coin was released. Interestingly, frequency markers decreased before the hand touched the coin, and this decrease was preceded by a spike in MNF/MDF suggesting high frequency spectral skew. A similar spike was observed at the end of the manipulation phase before the subject released the object. Before and after the hand was used for manipulation, much higher and more volatile frequencies appeard. In further regard to these regions, there appears to be a more symmetric frequency spectra during the recovery than in the reaching phase.

Figure 4.7: Subject 1 ADL 1 Spectral Moment Markers

Shown below in Figure 4.8 is the power spectra observed for flexors in ADL 1. Comparing Figures 4.7 and 4.8, it was seen that the high median frequency at the beginning and end of the trial was not caused by a high-power signal. In contrast, a high intensity low frequency signal was observed where the median frequency drops. This high intensity patch was also related to an increase in flexor activation in the time domain.
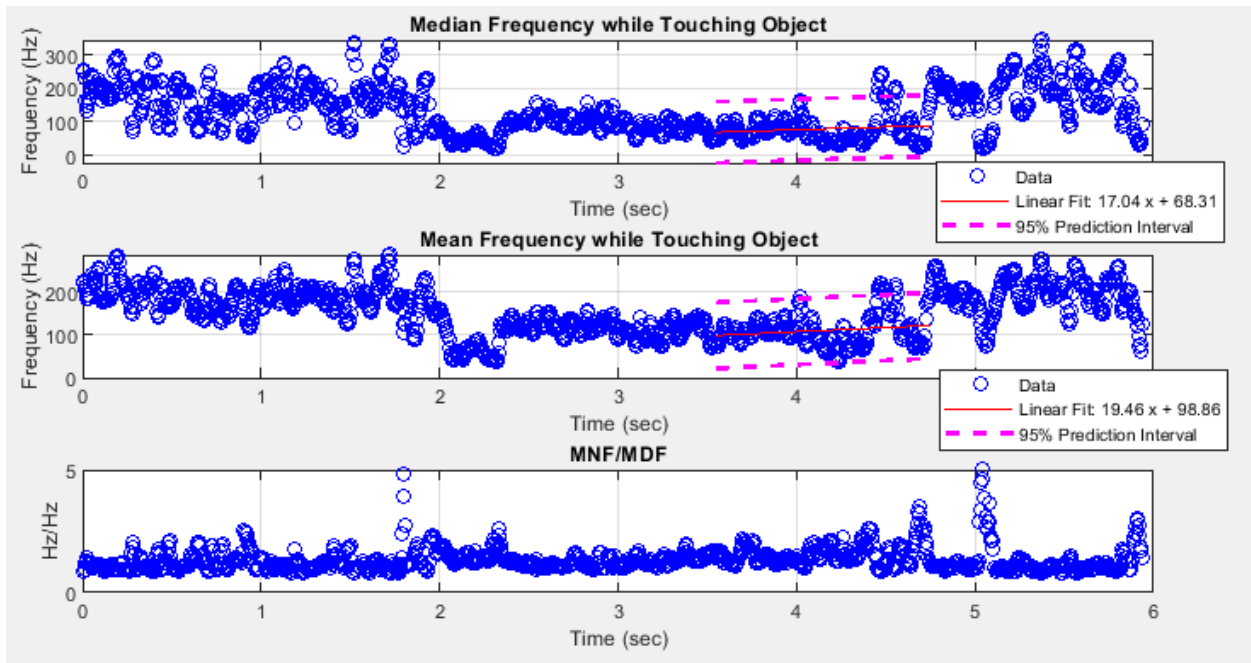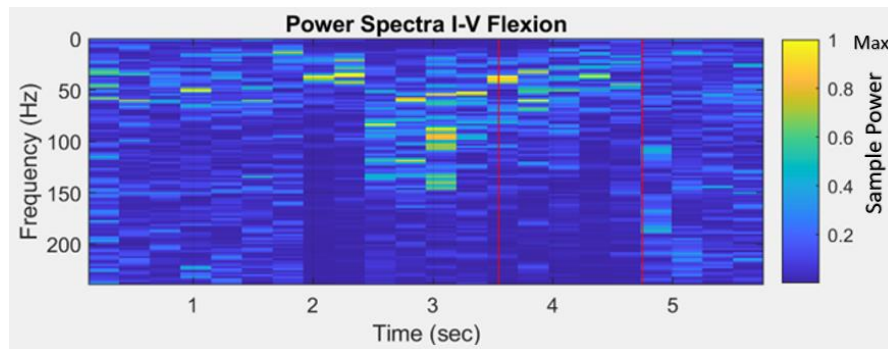

Figure 4.8: Subject 1 ADL 1 Spectrogram

Shown below in Figure 4.9 are the spectral moment markers for flexors during ADL 3 similarly to ADL 1 above. In the time domain, ADL 3 exhibited tetanization which was not seen in ADL 1. In the frequency domain this translated to significantly more motor unit activation sustained over time. The median and mean frequency in Figure 4.9 were regressed with a much greater y intercept frequency and a negative slope instead of a positive one as shown in ADL 1. Furthermore, contrasting the pinch observed in ADL 1 and ADL 3 was that the coin was manipulated for much longer in ADL 3. There was less time where the fingers were manipulated before the object was grasped in ADL 3, and the coins were manipulated for much longer in ADL 3 than in ADL 1. In regard to the ratio of MNF/MDF, there were less spikes showing spectral skewing. Notably though, there was a much more volatile increase in this ratio during recovery than what was observed during ADL 1.
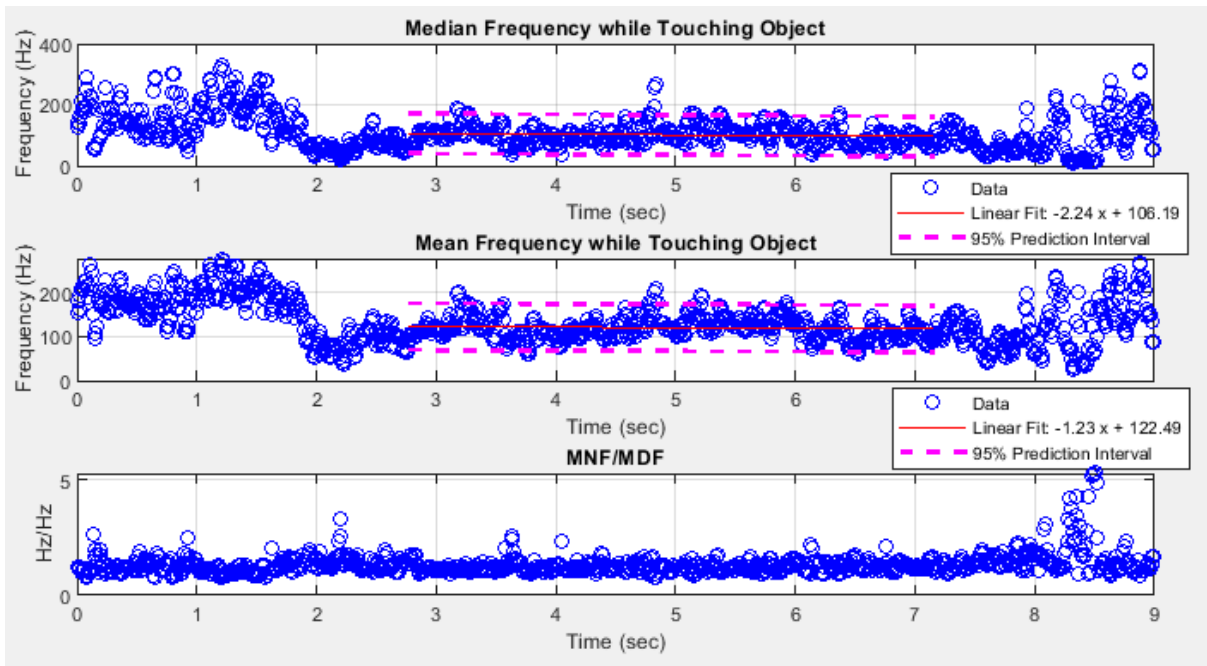
Figure 4.9: Subject 1 ADL 3 Spectral Moment Markers

Figure 4.10 displays the spectrogram for flexor sEMG during ADL 3. There was significantly more spectral activity observed in ADL 3 than there was in ADL 1. Comparing the time domain activation for the two pinches, the larger amount of spectral activity related to the tetanization of the pinch flexion in ADL 3. The highest intensity spectral activity seemed to occupy the same range in both ADL. The beginning and end of flexor activation exhibited a decrease in frequency.

Figure 4.10: Subject 1 ADL 3 Spectrogram

Shown below in Figure 4.11 are the spectral moment markers for flexor sEMG in ADL 6. Like ADL 3, the object was manipulated for much longer than ADL 1. Interestingly though, the median and mean frequency of ADL 6 were between the median frequencies of ADL 1 and 3 despite generating larger activation envelopes than both in the time domain. While flexor activation intensity was greater for flexors in ADL 6 than in ADL 3, Jarque Bou reported an overall greater activation of sEMG in ADL 6 than 3. Furthermore, Jarque Bou reported a greater degree of joint angle manipulation in ADL 6 than in ADL 3. The ratio of MNF/MDF was notable in ADL 6 for having significantly lower spikes than ADL 1 or 3. ADL 6 exhibited the ramp in MNF/MDF at the end of the manipulation phase similarly to ADL 1 and 3.
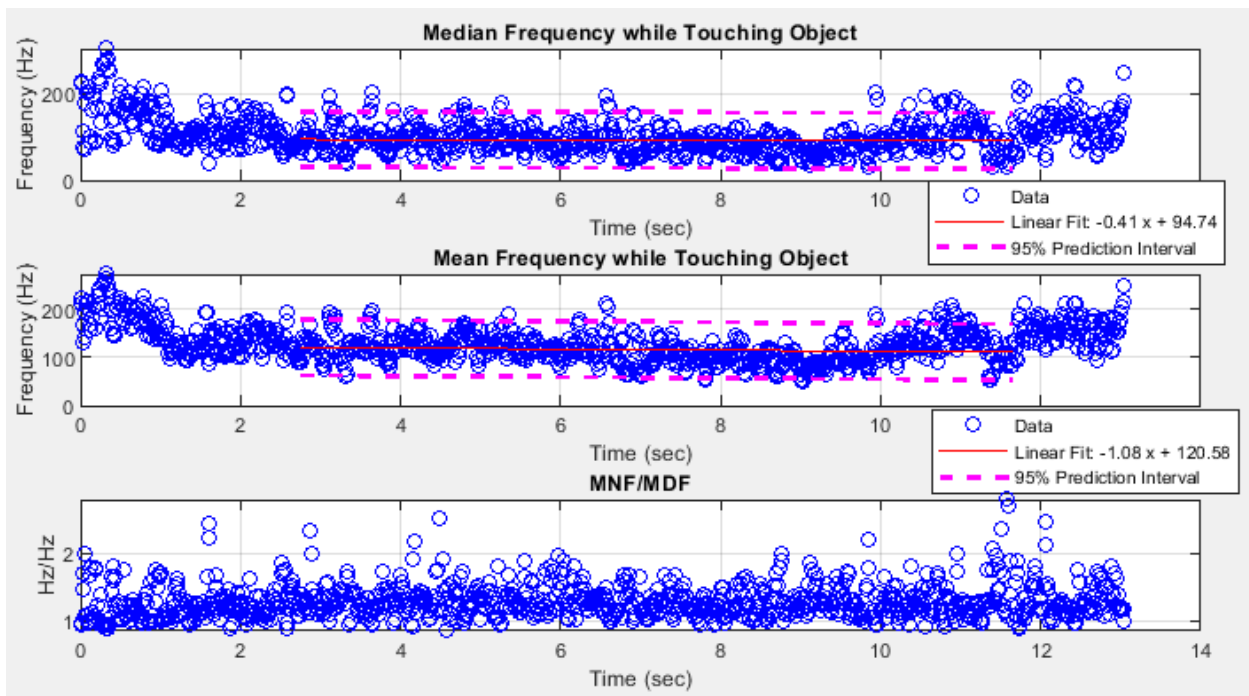
Figure 4.11: Subject 2 ADL 6 Spectral Moment Markers

Figure 4.12 shows the spectrogram for flexor sEMG during ADL 6. This experiment appeared to show further tetanization than that observed in ADL 3 and continued for a longer duration. When observing the spectrogram, it was not initially clear that the median frequency was lower in ADL 6 than it was in ADL 3. Furthermore, the intensity of contraction was also abstracted from the spectrogram.
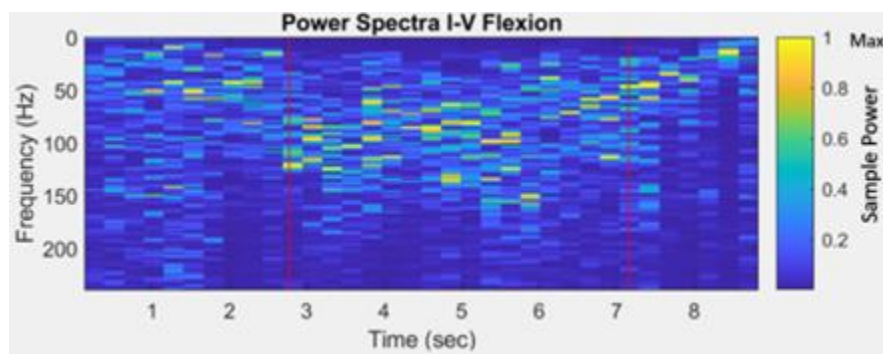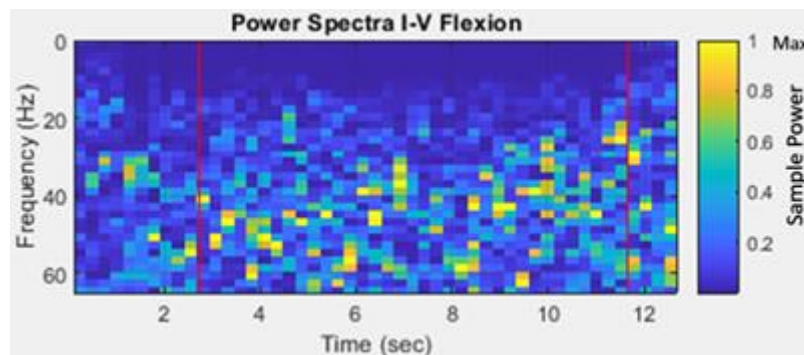

Figure 4.12: Subject 2 ADL 6 Spectrogram

Shown in Figure 4.13 are the spectral moment markers for flexor sEMG during ADL 14. The median and mean frequency observed in ADL 14 was the largest observed in the dataset. It was the second largest decrease in median and mean frequency during object manipulation, with ADL 3 causing the largest decrease. This was interesting because Jarque Bou reported the largest change in joint angle manipulation from ADL 14, ADL 3 had a comparable change in joint angle manipulation to ADL 1. The ratio between MNF and MDF remained between 0 and 2 for most of the study with no noticeable ramp after the manipulation phase. This contrasted with all three ADL before it.
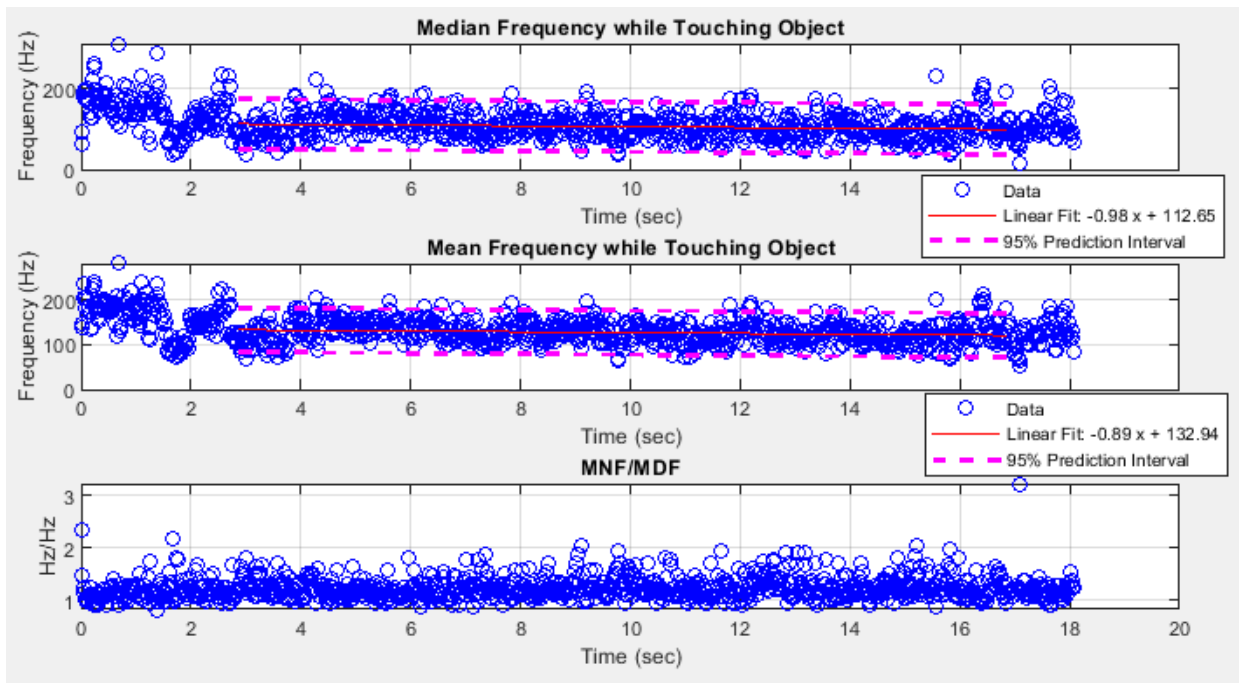
Figure 4.13: Subject 1 ADL 14 Spectral Moment Markers

Shown below in Figure 4.14 is the spectrogram for flexor sEMG during ADL 14. Flexors exhibited the highest amount of activation in ADL 14, and this could be seen below by the high intensity frequency activity between 20 and 150 Hz. ADL 14 also differed from others in that it caused high intensity signals up to nearly 200 Hz. All other ADL stopped near 150 Hz. The background noise of this ADL was significantly higher than other ADL.
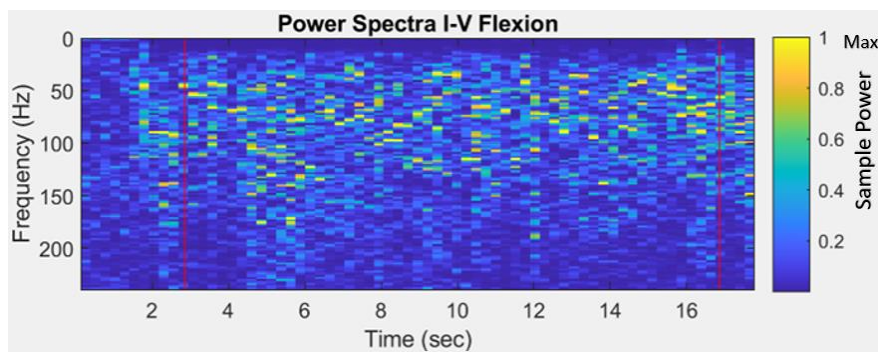
Figure 4.14: Subject 1 ADL 14 Spectrogram

4.3.d - Coherence Analysis

Coherence between flexors and extensors of digits II -V were compared with spectral images, activation of muscles, and the average joint angle motion of digits II-V MCP. Coherence was observed to increase from the lightest pinch to the strongest grasp observed. Some Alpha and Gamma wave coherence observed overlapped with power spectra of flexor and extensor sEMG. Coherence appeared often when a joint angle was maintained against an opposing force.

Anticipatory activation appeared to be visible in the coherence spectra of flexors and extensors. High coherence was observed in delta through gamma frequencies before the object under manipulation was grasped and let go. This was reflected with power observed near these points, but it did not occupy the same bandwidth as the entire coherence spike. Coherent results presented similar bandwidths in spectra and the coherence may have been caused by sEMG sensors measuring the same source.

Shown below in Figure 4.15 are the power spectra, intensity time plots and coherence for digits I-V flexion and digits II-V extension during ADL 1. Low frequency coherence in delta - alpha band appeared near chirps in the spectra of flexion and extension. Coherent spikes in the beta and delta range also correlated with high power information in the spectrograms. The patch of delta coherence near 60 Hz and 5 seconds also showed up in both power spectra at low intensity. A decreasing chirp in beta-gamma coherence was present during the largest change in joint angles but did not appear to relate to high power spectra of flexion or extension. An increase in low frequency power was only noted in extensors after object manipulation, yet high coherence was observed between flexors and extensors during this phase in the beta frequency band.

Figure 4.15: Subject 1 ADL 1 Coherence

Shown below in Figure 4.16 are the power spectra, intensity time plots and coherence for digits I-V flexion and digits II-V extension during ADL 3. Notably despite not relating to high intensity artifacts in either power spectra, beta coherence is much more present in low frequency coherence between the signals. Coherence around 2 seconds and 40 Hz appeared to relate to power spectra of flexors and extensors and related to the start of tetanization of hand muscles. During extension tetanus there was high power visible for extensors, and low power for flexors, this matched their respective intensity graphs. The region afterward had minimal coherence and a significant change in joint angle during object manipulation. Coherence exhibited after this patch appeared to correlate with a high degree of joint angle change. When both flexors and extensors were at their maximum tetanization between 4 and 6 seconds, there was almost no coherence visible from 0-60 Hz except for some in the delta-theta range.

Before the object was released, there was an increase in high frequency power in both flexors and extensors correlating to a high coherence between the muscles. This was likely anticipatory coherence as there was a significant change in both activation envelopes and joint angles after this spike. After the object manipulation phase, both flexors and extensors exhibited an increase in low frequency power that showed little to no coherence between the two signals in this band. There appeared to be more high-power signals observed in the alpha and beta range for extensors post object manipulation. This coordinated well with an increase in joint angle at the MCP during this time.

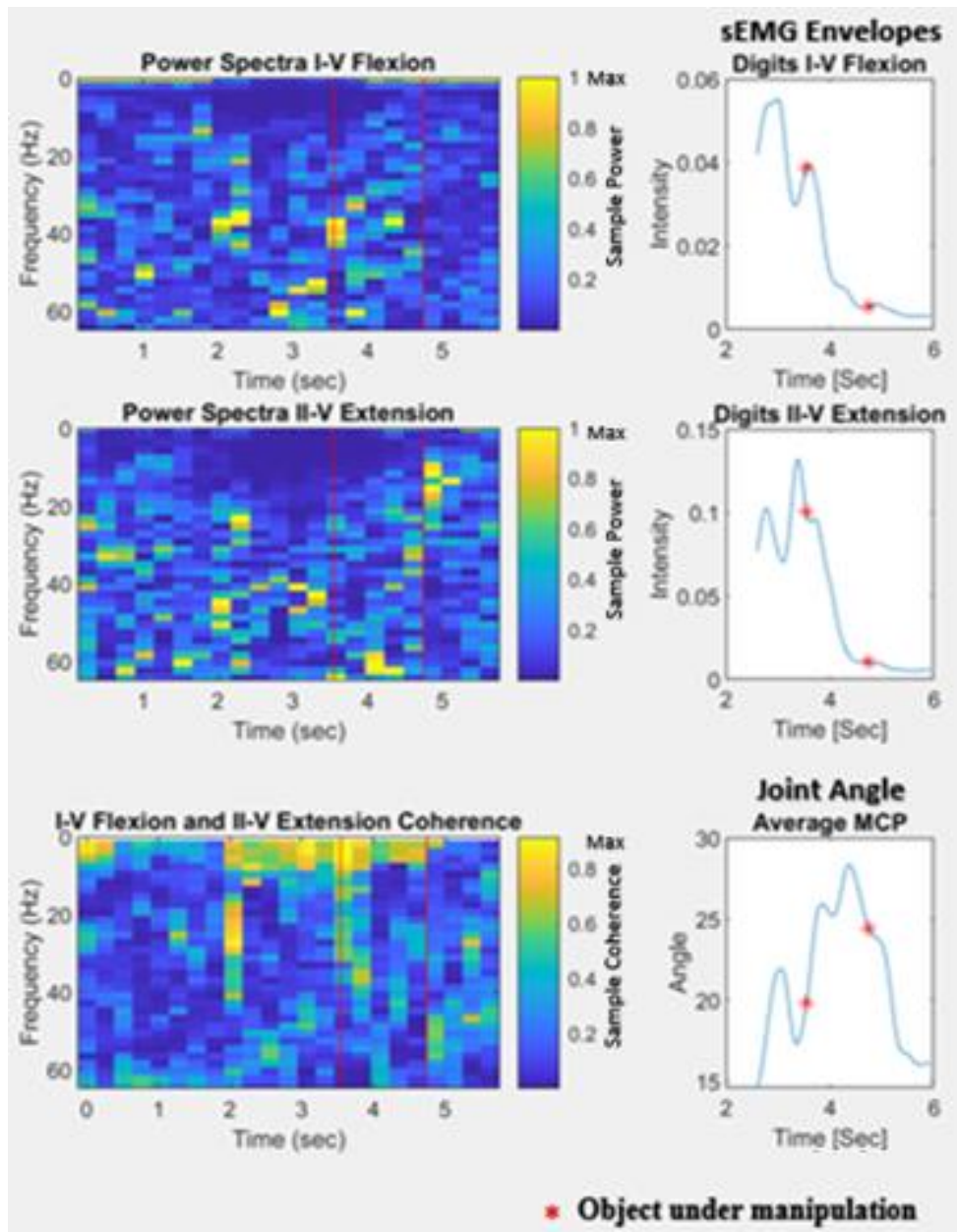Figure 4.16: Subject 1 ADL 3 Coherence

Shown in Figure 4.17 are the power spectra, intensity time plots and coherence for digits I-V flexion and digits II-V extension during ADL 6. Similar to all other ADL, there appeared to be high coherence in all bandwidths when the user first grasped and let go of the object being manipulated. This coherence occurred as spikes before the subject grasped and let go of the object. More coherence in the range of 0.6 to 0.4 was visible in this task than in the pinching tasks. The patch of coherence at 8 seconds near 40 Hz occurred at the same time as a significant decrease in joint angle. Leading up to this point there was an increase in flexor activity and afterward flexors decreased, and extensors increased. There was an increase in high frequency spectra after manipulation similarly to ADL 3. Notably after the manipulation phase there was higher coherence observed between the power spectra of flexors and extensors. A similar pattern of coherence was not observed in ADL 1 or 3 suggesting that the increase in coherence was related to an increase in flexor intensity. It appeared the periodicity of the screwdriver rotation was encoded into the spectra of the flexors and extensors, though this relationship is discussed in much greater detail during section 4.3.d. The largest coherence signal during object manipulation appeared between 8 and 9 seconds, despite there being minimal extensor power observed in this region. As there was no significant change in crosstalk levels of forearm muscles between supination and pronation of the wrist [59, 60], activation and coherence patterns observed suggested neural control of grip strength and rotational force.
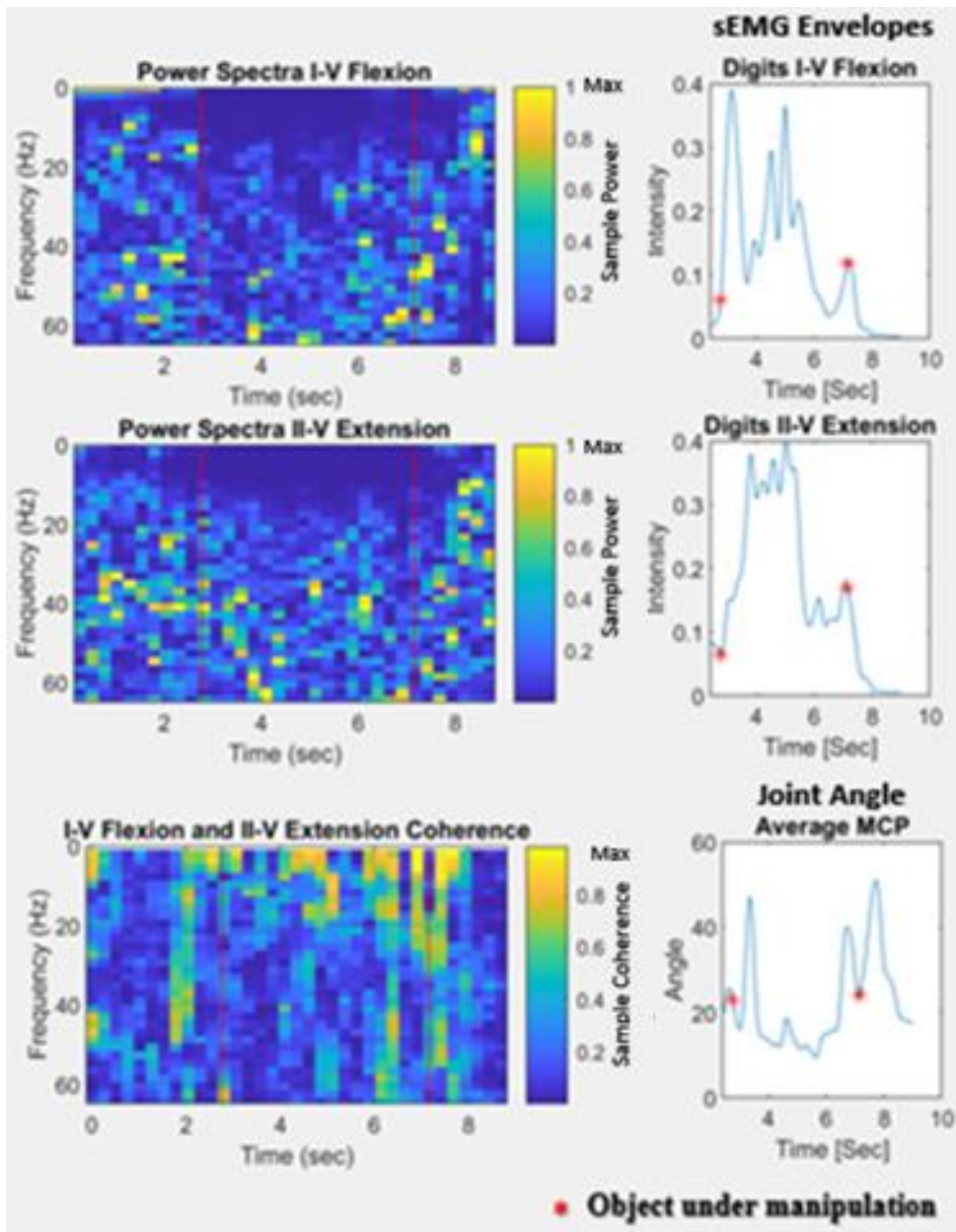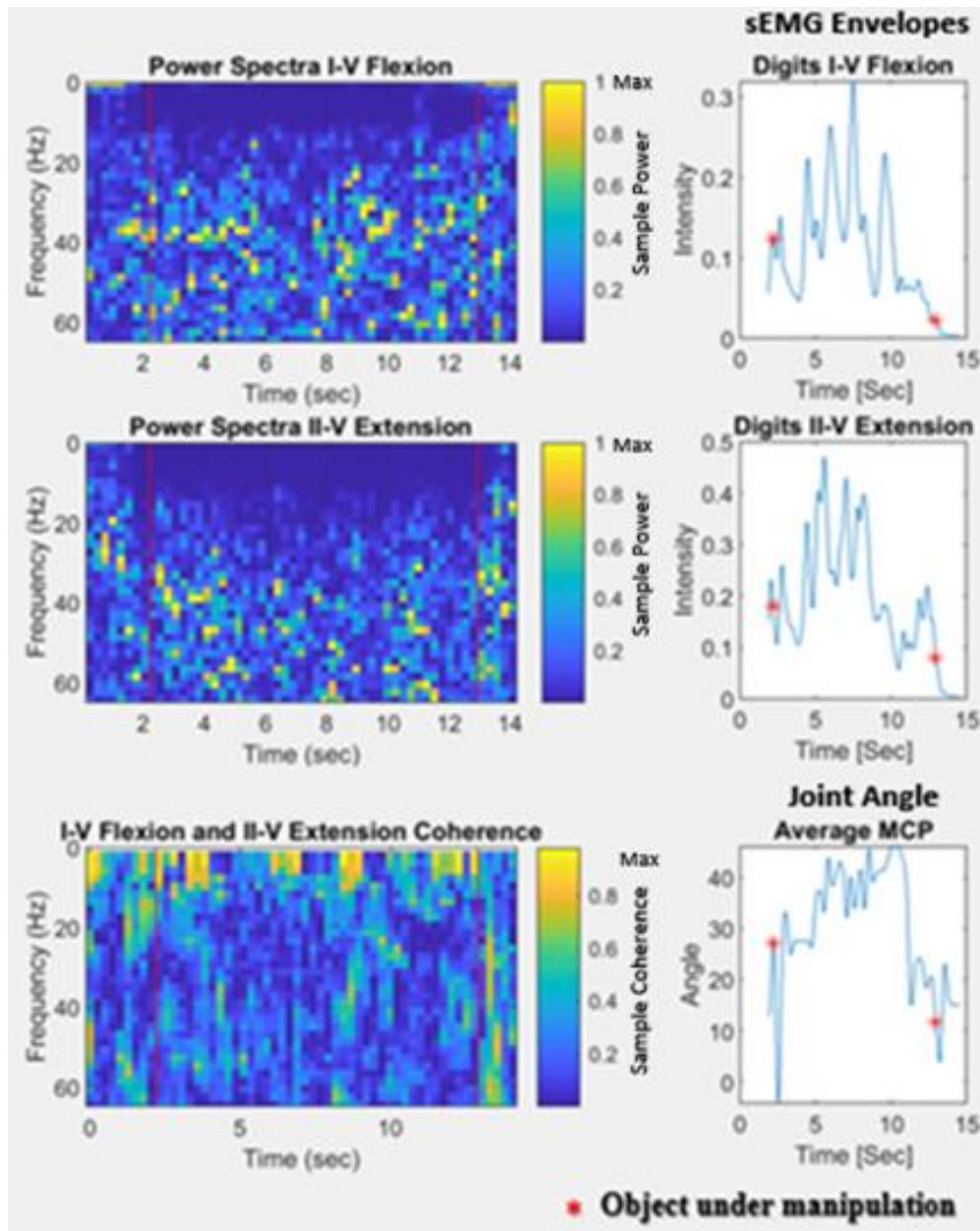
Figure 4.17: Subject 2 ADL 6 Coherence

Shown below in Figure 4.18 are the power spectra, intensity time plots and coherence for digits I-V flexion and digits II-V extension during ADL 14. ADL 14 exhibited the highest degree of coherence between all datasets and had an overlapping bandwidth with the power spectra of both flexor and extensor sEMG in alpha and gamma range. As crosstalk drastically increases with the intensity of muscle activation, it is hard to differentiate muscle synergy from the effects of forearm volume conduction without techniques like spatial filtering or HD-sEMG. The patches of high intensity power observed in both flexor and extensor spectra corresponded to patches of high coherence, which suggested that some of the high-intensity coherence may be caused by the synergy between flexors and extensors. The relatively consistent joint angle of 40 to 50 degrees at the MCP joint indicated that the hand is making fine adjustments to resist the forces of the knife during the task.

It was important to note that crosstalk was shown to increase with muscle effort and grip force [61]. Coherence is a combination of crosstalk and synergy, and as the intensity of muscle activation increases, crosstalk between muscles constitutes a larger ratio of the signal. This was promising, as the level of crosstalk in a coherence pattern can be somewhat inferred by magnitude of the activation envelopes, but it was important to make the distinction between crosstalk and true neural coordination through muscle synergy. The significant increase in coherence between flexors and extensors cannot be fully attributed to synergy, and this invalidates the application of coherence spectrograms especially at high intensities of muscle activation [3]. Fortunately, this also suggests that ADL 1,3, and 6 are less affected crosstalk, and that intensity can be used as a measure for the effectiveness of coherence analysis. In order to improve the accuracy of coherence plots, future work should investigate crosstalk reduction algorithms to better observe this phenomenon.
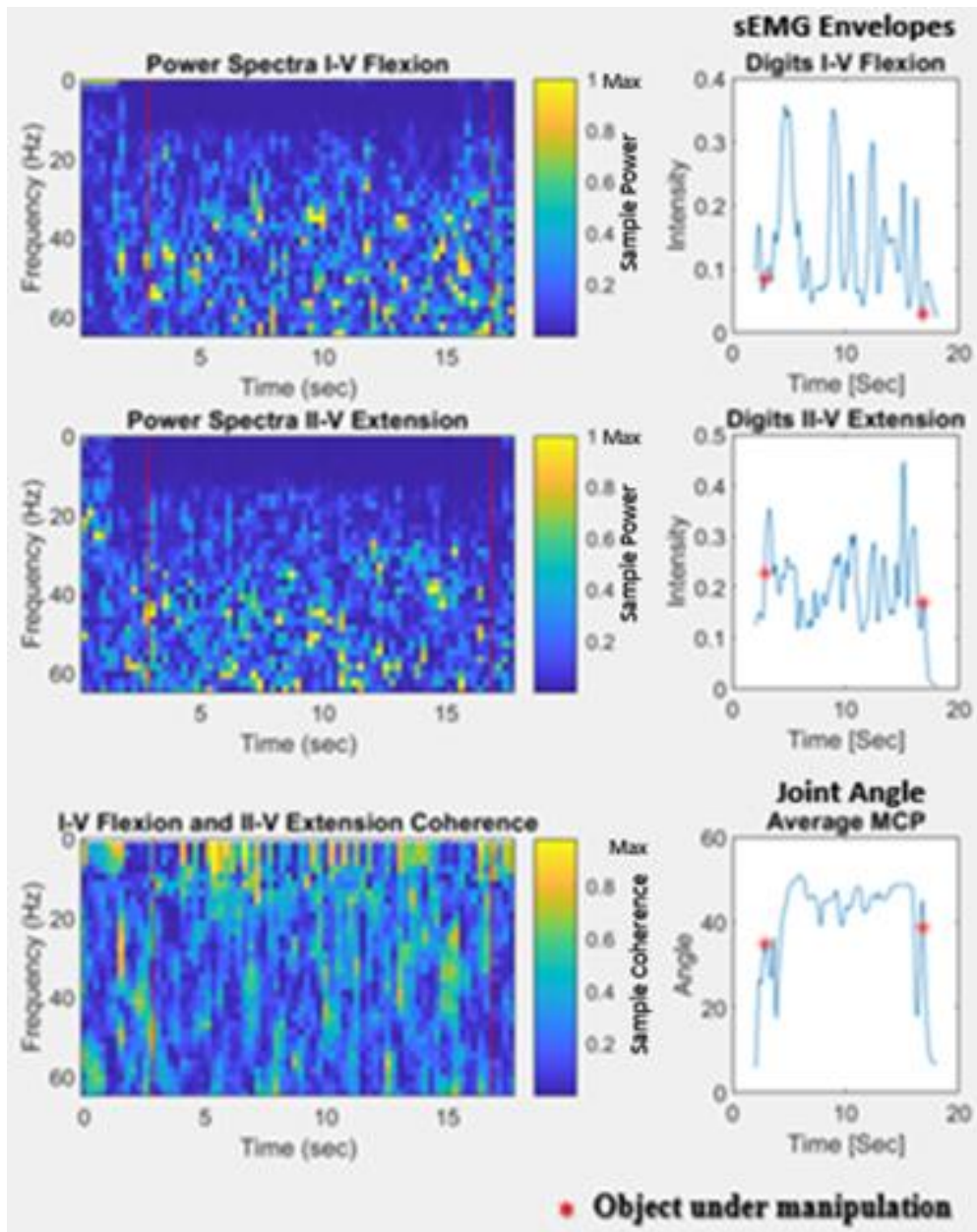
Figure 4.18: Subject 1 ADL 14 Coherence

4.3.e – Detection of Supination and Pronation

As spot 7 was speculated to measure both supination and pronation of the forearm and the CYBERGLVOE II does not have a DOF for measuring rotation of the wrist, observing these actions from the KIN-MUS-UJI dataset proved to be challenging. Figure 4.19 below exhibits activation envelopes for spots 3 (Digits I-V Flexion), 5 (Digits II-V Extension), 7 (Supination, Pronation, Wrist Extension), power spectra of spots 3, 5, and 7, Digit I CMC, and an average of the MCP flexion/extension for digits II-V. The MCP was held relatively constant, making fine adjustments as the screwdriver was manipulated in the hand. Digit I CMC appeared to be a better indicator for the periodicity of the screwdriver rotation through thumb motion.

The troughs of CMC joint angle align closely with the peaks in flexor and spot 7 activity. High extensor activity was observed, which is surprising as this task involved a high degree of flexion and supination force. Spot 7 exhibits a low frequency spike between 6 and 7 seconds which also occurs during a large degree of CMC joint change. This suggests the CMC releasing pressure on the screwdriver so that digits II-V are free to configure themselves for screwdriver rotation. Flexion appears to exhibit higher intensity and more consistent power spectral intensity when the CMC is held constant, suggesting that the thumb joint is resisting the frictional force of the screwdriver slipping during rotation. Furthermore, envelope spikes in all three sEMG spots appear to occur in synchrony, but due to the time scale of this figure phase relationships are not visible.

Figure 4.19: ADL 6 Intensities & Power Spectra: Spot 3, 5 and 7

Figure 4.20 below displays activation envelopes for spots 3 (Digits I-V Flexion), 5 (Digits II – V Extension), 7 (Supination, Pronation, Wrist Extension), power spectra of spot 7, coherence between spots 3&7, 5&7, Digit I CMC, and an average of the MCP flexion/extension f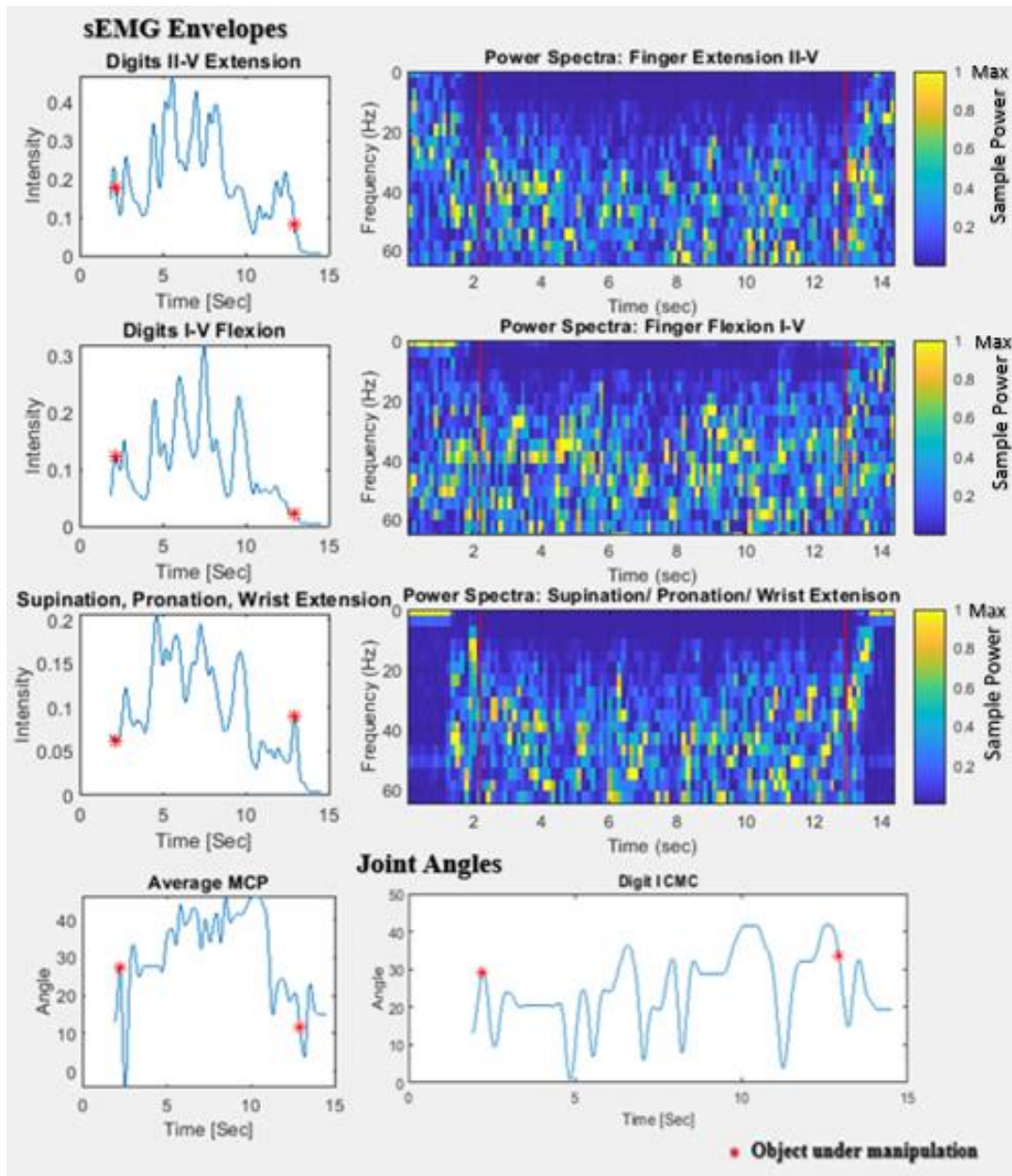or digits II-V. Very high coherence between spot 7 (Supination, Pronation, Wrist Extension) and spot 5 (Digit II-V Extension) was observed throughout the entire duration of object manipulation. As spot 7 observed wrist extensors and spot 5 observed digital extensors, some coherence between these two spots may have measured synergy between wrist and digital extensors. However, high coherence between these spots could also be a case of mutual source coherence. Shown in table 3.1, the extensor carpi radialis brevis was a likely source of crosstalk for spot 5 and could have obstructed synergy measurements.

In contrast, there was very low coherence between digits I-V flexors and spot 7 despite the activation envelopes of the two sEMG spots resembling one another. While synergy measurements may be impeded by mutual source coherence of the flexor pollicis longus, sensors were on the palmar and distal forearm respectively (see Figure 3.1) and would be impeded by the spatial filter of the bones and mass between them. There was an increase in coherence between spot 3 & 7 at the end of object manipulation (10s), which may have been an increase in synergy between the supinator and digit I-V flexors caused by fatigue. This was furthered by the results of Mogk, Keir, Yung, and Wells showing that there is a negligible increase in crosstalk on forearm muscles between supination and pronation tasks. These results suggest that this increase in coherence was not caused by wrist conformation changing crosstalk properties significantly [59, 60]. Another important consideration was that coherence increase may have been caused by the increase in crosstalk observed during increase in contractile force as described by Kong et al [61].
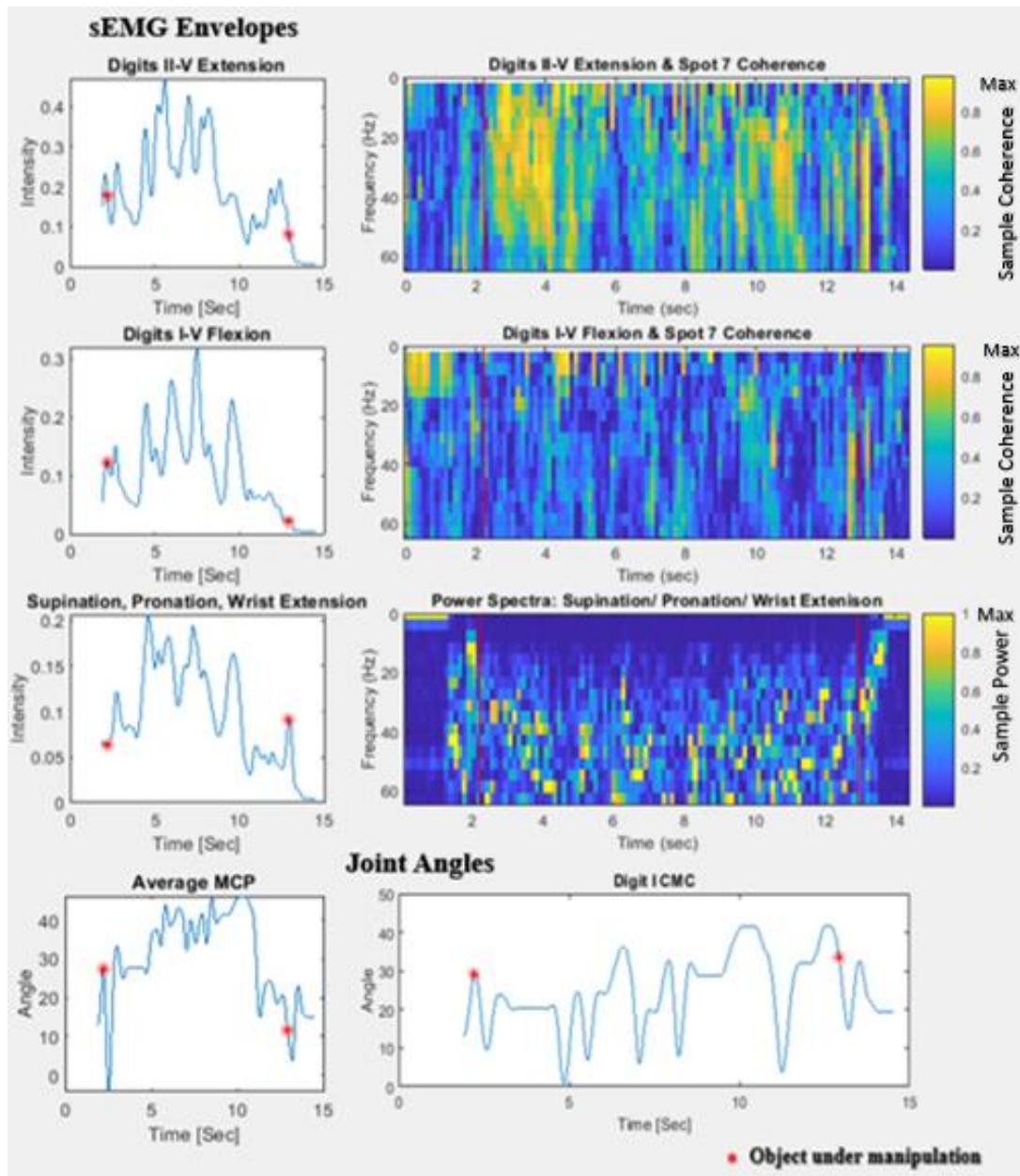
Figure 4.20: ADL 6 Spot 7 Power Spectra and Coherence with Spot 3 and 5

Shown below in Figure 4.21 are activation envelopes for spots 3 (Digits I-V Flexion), 5 (Digits II-V Extension), 7 (Supination, Pronation, Wrist Extension), Digit I CMC, and an average of the MCP flexion/extension for digits II-V for all pinch and grasp ADL observed in this experiment. This Figure was generated to show the phase relationship between flexors, extensors, and spot 7 during ADL 6 as it could not be discerned from Figure 4.19. As shown, the maximum spikes of intensity in spot 7 followed the maximum intensities of flexors very closely. Furthermore, these spikes of intensity in flexion and spot 7 appeared to be 90 degrees out of phase with the high intensity spikes of digits II-V extensors. This phase relationship between supination, pronation and wrist extension was exclusively visible during ADL 6. Spikes in flexion appeared to be loosely related to decreases in both digits I CMC and average MCP.

This phase relationship between spot 7, digit I-V flexors, and digit II-V extensors appeared to indicate the sequence of object release, reorientation with the screwdriver, and continued rotation. Flexion and spot 7 intensity envelopes aligning implied that the hand was grasping an object while supinating. These intensities decreased while extension increased implying a release and reorientation phase during the object manipulation of ADL 6. This relationship only appeared during ADL 6 with pinch tasks appearing to increase in spot 7 activity during increase of flexion and digits II-V extension tetanization. ADL 14 exhibited tetanized envelopes for all sEMG spots which appear to reach maximum intensity in tandem. Phase relationships of spot 7 intensity further differentiate tasks such as making a fist and rotating a screwdriver and outline the increase in information which could be attained through phase relationships between intensity envelopes provided in the dataset.

It should be noted that spot 7 not only measured supination and pronation, but also measured wrist extension. As II-V Extension was observed to be highly coherent with spot 7, crosstalk and

muscle synergies between these two locations were significant contributions to this signal which needed to be noted. Interestingly there was much less coherence between spots 5 and 7 despite their time varying envelopes following each other closely in this task. While the spikes of spot 7's envelopes followed I-V flexion closely, it appeared that intensity followed extensor activity to a lesser extent. Intensity of spot seven did not decrease significantly until II-V extension decreased, suggesting that wrist extension contributed significantly to the signal observed at spot 7. These results show that while information such as rotational joint angles were not visible from the CYBERGLOVE II, they may be inferred through the observation of phase relationships between envelopes. It also showed that despite supination and pronation being visible from the same location on the forearm, inferences could be made about the rotation of the forearm through analysis of flexion and extension envelopes and knowledge of expected action during the ADL.
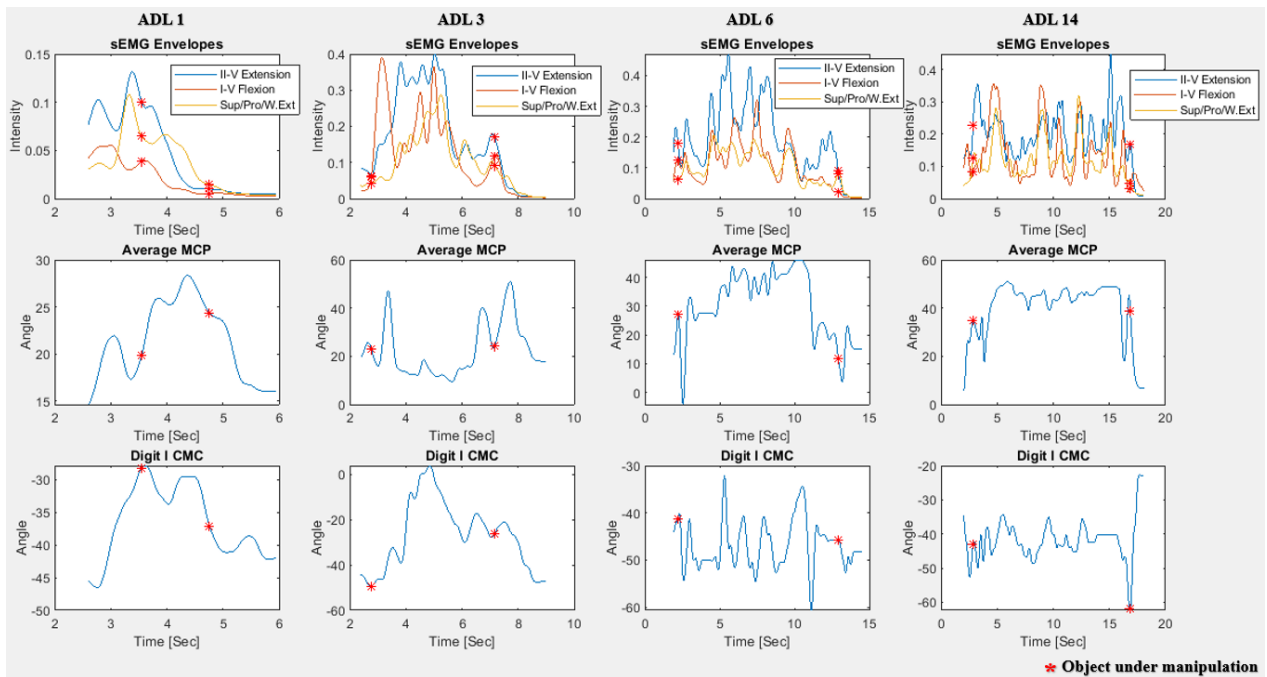

Figure 4.21: Differentiating Rotational Grasp Tasks

4.4 - Discussion

Results showed that pinch and grasp tasks could be best differentiated through observation of activation intensity of sEMG spot 3. This spot was above the flexor digitorum muscles, which are thought to be the largest contributors to sEMG signal in spot 3. In pinching tasks, the activation was a twitch or light tetanization. Interestingly, the light grasp in ADL 6 led to a smaller initial activation twitch than the grasp in ADL 3. This may be due to the subject digging around a coin purse and needing to coherently grasp a small coin, while in ADL 6 flexion force was used to grossly hold the screwdriver. Supination and pronation were used for rotational force to drive the action of screwing the screw into the board. When flexing to stabilize opposing forces, intensity of activation significantly increased such as observed in ADL 14.

These research findings suggest that both median frequency (MDF) and mean frequency (MNF) were inconclusive measures for differentiating between pinch and grasp tasks. The differences in MDF and MNF were not consistent across all tasks, and pinch tasks with extended manipulation ended up exhibiting steeper decrease in MNF/MDF and higher Y intercepts. This relationship between negative slope of MDF and MNF and the intensity of flexion may be due to the fine motor motion needing to perform an extended pinch task, which may have fatigued the subject more than a light grasp task. Therefore, the ramp in MNF/MDF was a more reliable indicator of muscle fatigue in pinch tasks, especially those with extended manipulation phases. Spectral moment was interpreted as a measure for fine motor control instead of activation in hand muscles, as fatigue was related to the relative intensity and time the object was under manipulation.

Coherence results were subdivided into four categories; one source measured from multiple electrodes (mutual source coherence), mutual innervation, anticipatory activation, and crosstalk. High intensity coherence observed in ADL 6 between spots 5 and 7 was likely an example of

mutual source measurement. The spikes before and after object manipulation in ADL 1,3,6, and 14 were likely anticipatory activation. Anticipatory activation would mean that the opposing muscles coherence is common neural input that the hand is to be manipulated and was therefore a very interesting finding. As forces increase in the ADL, coherence between spots was more likely to be observed. While it has been shown by several research groups that crosstalk increases with the intensity of muscular contraction, this coherence could also be influenced by anticipatory or mutual innervation as these sources sum. Low frequency coherence was likely caused by phase alignment of filtered signals at low frequencies.

Through analysis of spot 7 during ADL 6, changes in the phase alignment of intensity between flexors and extensors with spot 7 were observed. During non-rotational tasks, spot 7 was observed to activate in phase with both flexors and extensors. Conversely during rotation of the screwdriver in ADL 6 phase between the flexors and spot 7 was 90 degrees out from that of extensors. This phase alignment showed flexors working in tandem with digital flexors, while extensors intensity increased during flexor and supinator rest. This was indicative of the hand flexing and supinating to tighten the screw, then releasing the screw to readjust hand conformation for the next rotation. This encoding of periodicity has significant implications for tool use and shows that even without joint angle data for a DOF, information about its activity may still be captured using EMG.

Implications for further research suggest a similar amount of activation variability in each sEMG spot. Through observation of all spot activations and fingertip workspace data, many more gestures may be differentiable with low sensor input as proposed in this thesis. While this dataset has not been shown differentiate individual fingers using sEMG, it was shown that through measurement of available flexor activation that several degrees of pinch and grasping tasks could be observed. The breadth of information on the fingertip workspace included in the Jarque Bou dataset allows

researchers to study the hand with a high level of physiologic detail, without the need for direct interaction with subjects or complex recording instruments. Pinches and Grasps were differentiated using activation envelopes of sEMG sensors, light pinches and hard grasps were clearly differentiable actions through the measurement of activation envelopes of spot 3. Spectral moment showed some indication of task differentiation but was not as directly apparent as activation envelope intensity. Observation of spot 7 provided insight into rotational control of the forearm without direct measurement of supination and pronation joint angle.

Chapter 5 – Conclusions

The intent of this research has been to reimagine future human interfacing devices through the application of neuromusculoskeletal modeling to the extrinsic muscles of the hand in the forearm. The ARMS Lab Hand and Wrist Model, released in December 2021, and its integration of testing and training procedures using the CYBERGLOVE II, yielded the most advanced human hand and wrist model in existence at the time of the research. The Jarque Bou dataset was analyzed for application to the ARMS Lab model due to its application of the CYBERGLOVE II for joint angles. Pinch and grasp tasks were analyzed as validation tools for the ARMS Lab model as it extensively detailed the process for simulating pinch and grasp tasks. With the continued development and analysis of OpenSim models for human limbs and the improvements in neuromusculoskeletal modeling seen in the past two decades, this goal is becoming ever more achievable.

Existing material in musculoskeletal modeling of the hand and forearm was expanded upon through two parallel modes: implementing training sets and advancing data collection. The Jarque Bou dataset analyzed in chapters 3 and 4 showed the relationship between sEMG signals in the dataset and gross limb motion, providing an opportunity for further testing of the ARMS Lab model through its similarity of data input. Chapter 3 generated an atlas of every forearm muscle observable within this dataset as a tool for investigating actuation of the ARMS Lab model with the dataset and to provide likely crosstalk sources for each sEMG spot. Furthermore, analysis of the dataset showed that actions such as hand rotation may also be encoded in the sEMG spots despite lack of joint angles to compare this with. Future work provided in chapter 6 investigates the development of an HD-sEMG sleeve to circumnavigate the use of test data sets and to run the

ARMS Lab model in real time. These two separate investigations, along with the extensive literature review of NMM outlined in this thesis, offer a conclusive approach to the edge of this technology and ways in which it could be further developed.

This research discussed the analog front end needed for capturing sEMG, HD-sEMG, and addressed limitations of modern computers in implementing such a device as an HD-sEMG embedded system. While significant research is still needed in power, embedded system design, data transmission, and embedding of the NMM, it is not likely that this pipeline will be completed until the ARMS Lab model can be tested using the KIN-MUS UJI dataset. Future research combining this model and dataset is significant to developing such an NMM because the dataset is the largest collection of hand joint angle and sEMG data available open source and is further significant for its standardization of the SHFT process. Active muscles in the ARMS Lab Model could be chosen from results found in chapters 3 and 4 for ADL 1,3,6 and 14 to further simulate pinch and grasp tasks, while other ADL could be used to simulate new gestures with the model. In this way the thesis produces novel results itself but lays the groundwork for personal PhD study on the topic.

It was shown how the sEMG groupings in the Jarque Bou dataset can be used to observe bilateral actuation of the entire wrist and digits II-V flexion and extension, but some gestures such as the peace sign could not be differentiated due to the reliance on hand muscles. Through analysis of spot 7, it was found that the KIN-MUS-UJI dataset can provide insight into forearm and hand rotation through supination and pronation, even without having a joint angle to directly validate rotation. Limitations of the dataset such as large IED, reduction of groupings from thirty to seven using functional PCA, lack of MVC recordings, and lack of rotational joint angles were discussed. Furthermore, recommendations for improving the dataset such as sampling at a higher spatial

resolution, application of crosstalk reduction algorithms, and detection of MVC within ADL are discussed. Overall, the dataset provides valuable information about the movements involved in forearm and hand motion, which can help in understanding the mechanics of complex hand and arm movements.

Consolidation of neuromusculoskeletal modeling, HD-sEMG, and existing anthropometric models of the hand was performed for the purpose of developing a Human Interfacing Device (HID) controlled by sEMG activity of extrinsic hand muscles of the forearm. It is important to consider that such NMM technology is highly modular, and does not need to apply to sEMG of the forearm. As discussed in this research, NMM technology has been utilized for computational models of lower extremities and prosthesis. In this sense, this thesis benefits the study of kinematics as open-source development to a proven numerical algorithm which calculates human motion with a high degree of precision. Sensors are investigated for capability to capture sEMG at a sufficient spatial resolution to generate HD-sEMG, which greatly improves the capability of a system to identify optimal muscle locations and reduce crosstalk between muscles. With proper selection of muscles, any limb could be projected into the digital workspace given the proper musculoskeletal model.

Future work on this research will be focused on proving the feasibility of forearm and hand NMM for HID. While technologies like Kinect or the CYBERGLOVE II allow a user to translate gestures into HID commands, users must either treat the room, or be equipped with unwieldy technology to do so. Sensors small enough to fit 900 sEMG into an armband are investigated in future work for application of HD-sEMG to the forearm; a development which allows a "heatmap" of electrical muscle activity to be measured from the surface of the skin. While this does not directly elicit individual muscles being detected, a sleeve will be significantly more intuitive for

end users. Developments in HD-sEMG detection are at the edge of this field and constantly advancing. Several such sleeves have been designed by labs, but no open-source design has existed until the dissemination of this work.

This technology has application in the control of devices where precise hand movement is needed. Despite initial investigation as an interfacing vector for robotic surgical devices such as the DaVinci Robot, a plethora of applications have been considered from home appliance interfacing to piloting a crane, operating machinery outside of a spacecraft, prosthesis and assistive devices, virtual and augmented reality, gaming, and hazardous chemical handling. Furthermore, NMM has been shown capable for embedded systems, making it a perfect interface for individuals with disabilities or those with fully functioning limbs. Individuals with physical limitations on the fingertip workspace could still learn to use a high degree of the digital workspace through measuring functioning muscles or retraining new muscles to actuate the workspace. In research applications, this technology has even been proposed as a technique for physical therapy and training to help practicians better visualize subject muscle activity and joint moments.

Despite lack of discussion in this thesis, such devices, and the data that they produce will require significant ethical development for implementation in consumer products [62]. As shown through Neuromusculoskeletal Modeling and the work of Beauchamp et al, coefficients descriptive of an individual's unique somatome are required for transduction of joint angles of a limb. Commercial use of such technology raises concern about the ownership and control of biomedical data, while also creating a significant knowledge gap between developers and end users. While this thesis discusses open-source implementation of this technology purely for scientific development, companies selling such a device should be clear about data encryption, secure storage and

transmission protocols, and guidelines about the ownership and control of biomedical data for users.

In the age of modern computing, interfacing devices such as the keyboard and mouse can be the bottleneck for information transfer between a user and computer. Information transfer is limited by the user's knowledge of the device, but also the physiological characteristics of the individual using the tool, and the effectiveness of the tool at solving a specific task. While tasks such as technical writing make the use of a keyboard intuitive, 3D modeling such as CAD may see benefit from interfacing with a designer's hands. By detecting gestures through sEMG signals, the device would allow users to control devices and interact with technology in a way that is natural and intuitive. Additionally, because the device does not require physical contact with the hand, it could be used in situations where the user's hands are otherwise occupied or unavailable. This could improve information transfer and increase the user's ability to interact with the environment. In a similar manner to how voice recognition software contributed speech as a computer interfacing vector, NMM offers the opportunity for gesture recognition and the ability to vectorize human hand motion for computer input.

Chapter 6 - Suggestions for future research

Future work was focused on the development of an integrated system architecture for High Density surface electromyographic (HD-sEMG) transduction of hand joint angles in human interfacing devices (HID). This involved the development of a preamplifier with high spatiotemporal resolution, as well as the integration of an ADC and RAM for data acquisition and storage. The goal of this work was to create a reliable and efficient HID that can accurately translate sEMG signals into intuitive and responsive hand gestures, ultimately enhancing the usability and accessibility of human-machine interfaces (HMI). The work in this section was included for insight to solve several of the open technical and scientific issues referenced in the introduction of IEEE Press' Surface Electromyography: Physiology, Engineering and Applications published in 2016. Data transmission and storage is not investigated extensively in this work but was included for the dissemination of viable solutions and methods for the development of this sleeve. For the ARMS Lab Model to be investigated for embedded systems, these open issues must be addressed.

While the non-invasive nature of sEMG is useful for commercial applications, the significant drop off in signal quality from fine wire EMG means that the seven signals measured will be corrupted with crosstalk, noise, and motion artifacts. While the dataset only recorded seven sEMG spots, the original research performed to find these spots investigated 30 sEMG locations on the forearm [47]. The purpose of this future work was to design an sEMG amplification system that can capture HD-sEMG with a high bandwidth and sampling frequency for use as an alternative input for EMG Driven Musculoskeletal Modeling. The HD-sEMG sleeve designed in this chapter implements preamplifiers small enough to observe ~ 900 signal locations on the forearm and

benefits previous research as an investigatory tool for increasing the number of sEMG signals observable to spatiotemporal resolution.

The architecture presented in this section is open source and was designed as a launchpad for future work into this topic. While this preamplifier PCB is available on GitHub and scalable for HD-sEMG, it requires development of electrode connectors, referencing, and power. Power was not investigated in this research, but a suggestion of Merletti et al is the development of battery powered preamplifiers [1]. These tasks along with testing of the completed preamplifier should be performed before a rigid-flex sleeve is designed for the device. Implementation of the rectification circuit provided has not been performed but was included as analog rectification would decrease computational load on the neuromusculoskeletal model.

6.1 – Data Acquisition Units

Data Acquisition Units (DAQ) convert voltage signals into digitally stored data and provide a robust and programmable tool for the development of an HD-sEMG sleeve. Examples of such technologies typically used for sEMG study are the 16-Channel EMG System through Motion Labs and PowerLab System through National instruments shown below in Table 6.1. While not utilized for data capture in this thesis, many DAQ offer flexibility in data capture through expandable I/O, companion signal processing software, and the ability to test sensors before implementation of an embedded system. Although these devices are relatively inexpensive for time invested in development of an embedded system, most are not small enough to be wearable and do not have the number of channels required to capture HD-sEMG.

Table 6.1: Example DAQ Devices

Name	Channels	Sampling Freq	Resolution	Citation
PowerLab C Digital DAQ	<32	<100kHz	16 bit	[63]
MA400 EMG System	<16	2kHz	16 bit	[64]

6.2 – HD-sEMG Sleeve Architecture

The system architecture shown below in Figure 6.1 illustrates the implementation of Wang, Tang, and Bronlund's modified sensor topology discussed in chapter 2.3. Preamplifiers are separated from filtering and digitization in this Figure as a reminder to readers that signal integrity is significantly impeded by distance between it and electrodes and should therefore be designed to reduce this distance as much as possible. The distance between preamp, filter, and rectifier is less causal on interference. Implementation of analog rectification is optional and implemented in this Figure for visualization purposes, investigation is still needed on the voltage drop of the rectifier. Furthermore, this investigation does not include powering this system. Embedded analog to digital conversion (ADC) for sEMG was reviewed extensively by Merletti et al [1] but could be substituted with a data acquisition (DAQ) unit of a sufficient sampling rate such as the PowerLab system [63].
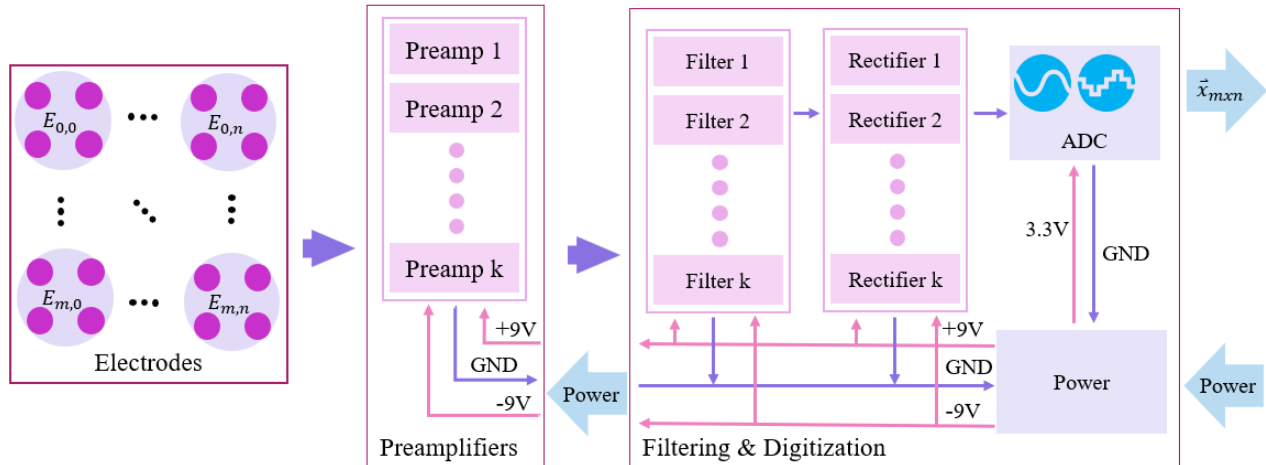
Figure 6.1: HD-sEMG Signal Conditioning, Filtering, and Digitization

To produce a wearable device usable as an HMI, neuromusculoskeletal modeling of the hand and forearm will need to be implemented on an embedded system. This not only requires all sensors to be captured as digital signals at a sufficient sampling frequency of 2 kHz at 1k samples per second [9], but also that this data is readily available for signal processing at a sufficient frequency for the model of the limb to update. While ADCs for sEMG have been reviewed extensively by Merletti et al [1], particular interest has been taken to the ADS1298 for its implementation of Σ - Δ converters [65], ability to turn channels on and off, low power consumption and small size.

Using the ADS1298 for the designed HD-sEMG sleeve addresses limitations in both power and the sampling rate through its eight parallel Σ - Δ converters. This parallelism means that for 900 sEMG sensors, approximately 115 ADC will be required. Equation 35 estimates the maximum number of slave ADS1298 modules which can be connected to one master device as the frequency of the slave clock divided by the sum of the data rate times the number of bits times the number of channels and a 24-bit status word. Using a 48 MHz SCLK for eight 24-bit precision channels sampling at 1 kSPS yields a maximum number of 250 devices, significantly higher than the number

of ADC required for the system. Furthermore, if analog rectification can be implemented, the data

rate can be drastically reduced to a minimum of 8 Hz or synchronized with the sample rate of the

CYBERGLOVE II (90 Hz).

$$N_{DEVICES} = \frac{f_{SCLK}}{f_{DR}(N_{BITS})(N_{CHANNELS}) + 24}$$

<div align="right">Equation 35</div>

There are several ADCs that offer comparable power consumption, sampling speed, and

precision to the ADS1298, but with higher channel counts. The AD7793, MCP3911, and

MAX11131 are three examples of such ADCs that are also SPI devices. Compared to the

ADS1298, which has 8 parallel Σ-Δ converters and a maximum of 8 input channels, the

ADAS14400 from Analog Devices offers 40 input channels with 14-bit resolution and a maximum

sampling rate of 400 kHz, while the MAX11905 from Maxim Integrated offers 20 input channels

with 14-bit resolution and a maximum sampling rate of 1 MSPS. All three ADCs use the SPI

interface and have comparable power consumption, making them suitable choices for embedded

systems requiring high channel count and precision with fast sampling rates. The selection of the

appropriate ADC will depend on the specific needs and constraints of the project, such as power

consumption, sampling rate, and number of channels required.

When considering data storage on an HD-sEMG device, it's essential to consider the data

requirements of the specific application. For example, recording raw sEMG for 900 sensors at

1kSPS and 24-bit resolution would require 5.5 megabytes of memory per second, which is

impractical for low-cost real-time implementations. However, if the rectified integral of EMG was

implemented in hardware, this operation would be reduced significantly to 5.52 kilobytes per

second. Factors such as read and write speeds, power consumption, voltage, and memory density

should be considered when choosing a RAM option. Careful evaluation of each option is necessary to determine the most suitable choice for the specific requirements of the implementation.

For data storage on an HD-sEMG device, several RAM options are available with different strengths. The Fujitsu MB85RS256T device is an excellent choice for applications that require fast access times and low power consumption operating at 1.8 V over SPI up to 20 MHz and storing up to 2 megabytes [66]. However, if large storage capacities are a priority, the Alliance Memory AS7C34100A SRAM device offers 8 megabytes of memory density, while maintaining fast access times through a 100 MHz parallel interface and low power consumption [67]. On the other hand, the Cypress Semper NOR Flash S34ML08G2 device offers an impressive 8 gigabytes of memory density and read speeds of up to 133 MHz over SPI, making it the best choice for applications that require a large storage capacity [68]. Each RAM option has its unique strengths, and careful consideration of the specific requirements of the application is necessary to determine the best choice.

While visual feedback to raw sEMG signals is only required during determination of measurement locations, data acquisition units (DAQ) such as the MA400 system require supplemental feedback devices to visualize sEMG which can cost as much as the DAQ itself [69]. A solution to this may be utilizing the work of Kandalaft et al, a solution to transmitting HD-sEMG data may be using FPGA and MQTT technology. Baud-Rate limitations could be circumvented by selecting the number of ADC through FPGA "pipes" to that which can be transmitted over WiFi at a sufficient frequency [70]. In this way, parallel WiFi connections can be resynchronized sequentially after WiFi transmission to a PC for storage.

6.3 - Preamplifier PCB

The preamplifier circuit used in this design was based on the INA128 topology used by Wang et al for low voltage signal measurement [9] as shown in Figure 6.2. Despite the INA828 being available as an upgrade for the INA128, the topology of the circuit has not been modified and the two parts can be considered replacements for one another. The INA828 benefits from increased precision, ESD ratings, reduced bias current, bandwidth and slew rate.
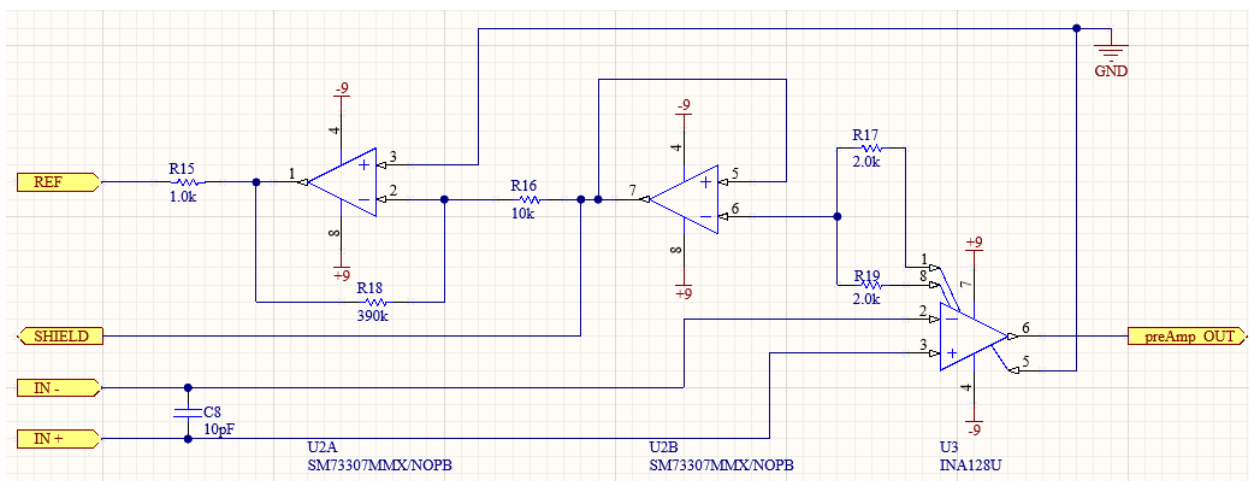

Figure 6.2: Schematic for EMG Preamplifier

The surface area of the forearm is approximately 900 cm^2 [71]. As shown in Figure 6.3 below only the differential input must be connected to the wristband. The Figure shows the INA128 configured with positive and negative leads for the preamplifier connected across the measurement site, while the shield was connected to the amplifier ground. Furthermore, the Figure shows a single reference electrode placed far away from the positive and negative leads [31]. A similar topology could be implemented for EMG, but with a significantly smaller IED [72].

Because the Ref electrode was a separate electrode far from the wristband, and the shield was connected to the preamplifier PCB ground, there are only two electrodes required per sensor. This

is referred to as a bipolar measurement as the sensor measures the difference between the positive and negative electrodes. At a pitch and IED of 5 mm, each electrode required an area of 10x10 mm as shown in Figure 6.3. This led to approximately 900 electrodes which can be placed on the forearm. A diagram for connecting preamplifiers to an sEMG wrist band is shown in Figure 6.4.
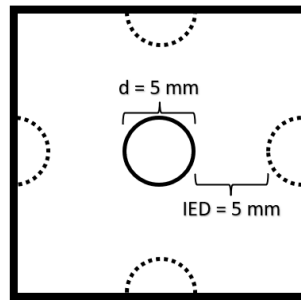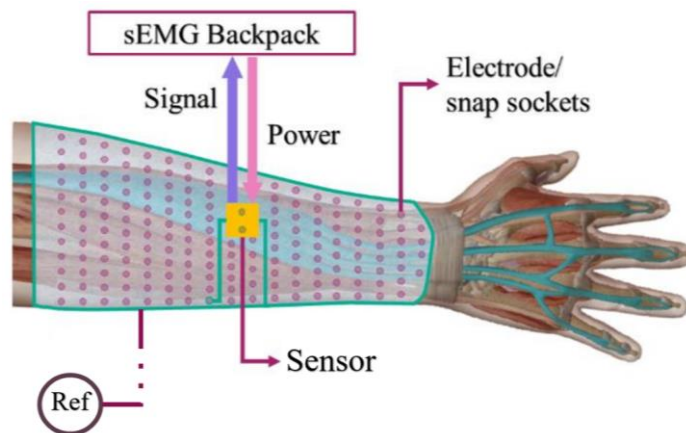

Figure 6.3: Electrode Spacing

Figure 6.4: sEMG Wristband

Each sensor used two electrodes; therefore, the entire preamplifier circuit must occupy a space no larger than 10mm x 20mm. For implementation of the preamplifier PCB, 0402 resistors and capacitors were chosen for prototyping. The size requirement for the sensor was satisfied as shown in Figure 6.5. For complete implementation, power circuitry and signal would need to be exchanged between preamplifiers and the sEMG Backpack as shown in Figure 6.4.
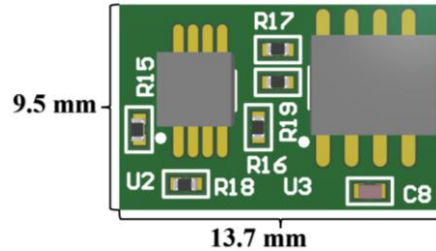
Figure 6.5: sEMG Preamplifier PCB

This device could be made using individual preamplifier PCBs to be snapped onto an electrode wristband but would likely benefit from advancements in Rigid Flex PCB technology to have an elastic wristband which can slide on and off the forearm. Using Rigid Flex technology – while causing a significant increase in the price of the device – would mean that less assembly is required to collect data using the device. Different processes for microelectrode fabrication were investigated by Zhou et al [72]. Gold microelectrodes were fabricated at diameters of 150 -300 µm by Choi et al using an electrochemical etching technique and a parylene based flexible polymer for isolation [73]. This would be beneficial in the design of a rigid flex circuit. A GitHub link for the sensor PCB is listed in Appendix B.2.

This sEMG amplification system would be capable of capturing high information signals on the forearm satisfying the spatiotemporal Nyquist limit. Implementation of this system would capture sEMG at a spatial frequency thirty times that of Jarque Bou et al, offering new opportunities for input to the ARMS Lab Hand and Wrist Model. The system was designed in ordinance with current IEEE research on optimal HD-sEMG systems with an IED of 5mm and has preamplifier circuitry which can fit between IED. Because rigid flex technology would be preferred in the design of such a system, flexible parylene isolation between gold microelectrodes was determined optimal for this application. Further developments in this device could be explored in electrode material, cross talk between sensors, or capacitive sensors.

134

6.4 - Precision Full Wave Rectifier

While the Jarque-Bou dataset implemented the envelope of sEMG digitally, computational expense could be reduced through the implementation of a full wave rectifier. The two most significant issues with implementing analog rectification are the considerations of power and voltage drop. The rectifier designed below in Figure 6.6 has a voltage drop of approximately 50 mV but could likely be reduced by using Schottky diodes in its topology. Furthermore, the design below requires a supply voltage of +/-15 V. Output voltage equations are shown for positive and negative voltages in equations 36.a and 36.b respectively [74].
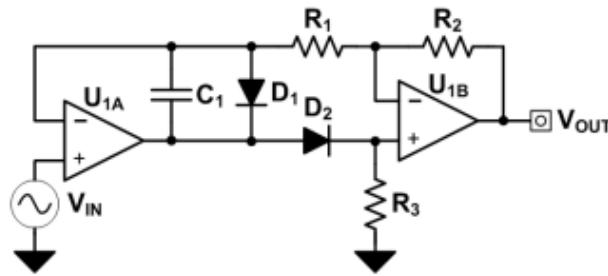

Figure 6.6: Precision Full Wave Rectifier [74]

$$V_{OUT} = V_{IN}$$ Equation 36.a

$$\frac{V_{OUT}}{V_{IN}} = \left(-\frac{R_2}{R_1}\right) = -1 \ [V/V]$$ Equation 36.b

Appendix A - Forearm Muscle Atlas for KIN-MUS UJI Dataset

Table A.1: Muscles deep to sEMG Spot 1

Muscle	Origin	Insertion	Action	Innervation	Spinal Location	MU Count
Flexor Carpi Ulnaris						
	Medial epicondyle of humerus, olecranon, and posterior border of ulna	Pisiform, hamate, base of metacarpal V	Wrist flexion, wrist adduction	Ulnar nerve	C7-T1	C7-T1

Table A.2: Muscles deep to sEMG Spot 2

Muscle	Origin	Insertion	Action	Innervation	Spinal Location	MU Count
Flexor Carpi Radialis						
	Medial epicondyle of humerus	Base of second and third metacarpal bones	Flexion and abduction at wrist	Median nerve	C7-C8	235
Palmaris Longus						
	Medial epicondyle of humerus	Palmar aponeurosis and flexor retinaculum	Wrist flexor	Median nerve	C7-C8	

Table A.3: Muscles deep to sEMG Spot 3

Muscle	Origin	Insertion	Action	Innervation	Spinal Location	MU Count
Flexor Digitorum Superficialis						
	Medial epicondyle of the humerus, ulnar coronoid process, below radial tuberosity	Anterior margins on the base of middle phalanges of digits II -V	Flexor of fingers, primarily at proximal inter- phalangeal joints	Median nerve	C8-T1	306
Flexor Digitorum Profundus						
	Upper three quarters of the anterior and medial surfaces of the body of the ulna, interosseous membrane, and deep fascia of the forearm	Base of the digital phalanges of the fingers	Flex hands at both inter- phalangeal joints digits II-V	Ulnar nerve	C8-T1	475

Flexor Pollicis Longus						
	Middle half of the anterior surface of the radius and the adjacent interosseous membrane	The base of the distal phalanx of the thumb	Flexion of the thumb	Median nerve	C7-C8	

Table A.4: Muscles deep to sEMG Spot 4

Muscle	Origin	Insertion	Action	Innervation	Spinal Location	MU Count
Abductor Pollicis Longus						
	Lateral dorsal surface of ulna and radius interosseous membrane	Pedicle of 1st metacarpal	Thumb extension (abduction)	Posterior inter-osseous nerve (deep division radial nerve)	C8-T1	126

Extensor Pollicis Brevis						
	Lateral dorsal surface of body of radius interosseous membrane	Base of proximal phalanx of thumb	Thumb extension, wrist abduction	Posterior inter-osseous nerve (deep division radial nerve)	C7-C8	
Extensor Pollicis Longus						
	Middle third of posterior surface of ulna, interosseous membrane	Thumb, distal phalanx	Extension of thumb	Posterior inter-osseous nerve (deep division radial nerve)	C8-T1	14

Table A.5: Muscles deep to sEMG Spot 5

Muscle	Origin	Insertion	Action	Innervation	Spinal Location	MU Count
Extensor Digitorum						
	Lateral epicondyle of humerus by common tendon	Extensor expansion of middle and distal phalanx of digits 2-4	Extension of hand, extension of wrist, extension of fingers	Posterior inter-osseous nerve (deep division radial nerve)	C8-T1	273

Table A.6: Muscles deep to sEMG Spot 6
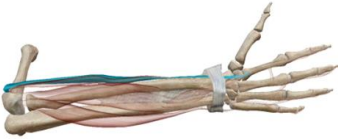
Muscle	Origin	Insertion	Action	Innervation	Spinal Location	MU Count
Extensor Carpi Ulnaris						
	Humeral head: lateral epicondyle of the Humerus. Ulnar head: olecranon, posterior surface of ulna, ante-brachial fascia.	5th metacarpal	Wrist extension, wrist adduction	Posterior inter-osseous nerve (deep division radial nerve)	C7-C8	

Table A.7: Muscles deep to sEMG Spot 7

Muscle	Origin	Insertion	Action	Innervation	Spinal Location	MU Count
Brachioradialis						
	Lateral supra-condylar ridge of the humerus	Distal radial styloid process	Flexion of the elbow, supination and pronation of the radioulnar joint to 90deg	Radial nerve	C5-C6	
Pronator Teres						
	Humeral head: medial supra-condylar ridge of humerus. Ulnar head: coronoid process of ulna	Middle of the lateral surface of body of the radius	Pronation of forearm, flexes elbow	Median nerve	C6-C7	
Extensor Carpi Radialis Brevis						
	Humerus at the anterior of lateral epicondyle	Posterior base of 3rd metacarpal	Extensor and abductor of the hand at the wrist joint	Radial nerve	C5-C7	890*

Extensor Carpi Radialis Longus						
	Lateral supra- condylar ridge humerus	2nd metacarp al	Extensor at the wrist joint, abducts the hand at the wrist	Radial nerve	C5-C7	890*

*Motor unit count for ECRB and ECRL is a joint reference [1].

Appendix B – Git Hub Links

Appendix B.1 - GitHub Link for Forearm Atlas

https://github.com/beauchab/GestureComputerInterfacing

Appendix B.2 - Preamplifier GitHub

https://github.com/beauchab/PreAmplifier-sEMG-PCB-

Appendix C - Declaration of Co-Authorship & Previous Publication

Appendix C.1 - Co-Authorship Declaration

I hereby declare that this thesis incorporates material that is the result of joint research with Dr. Nabeeh Kandalaft, Dr. Samhita Rhodes, Dr. Brian Krug, Dr. Gordon Alderink and Dr. Karl Brakora. I am aware of the Grand Valley State University Policy on Authorship, and I certify that I have acknowledged contribution of other researchers to my thesis and have obtained written permission from each of the co-authors to include the above materials in my thesis.

I certify that this thesis and the research to which it refers is the product of my own work.

Appendix C.2 - Declaration of Previous Publication

This thesis includes five original papers that have been previously published / submitted for publication in peer reviewed journals, as follows:

Thesis Chapter	Publication title/ full citation	Award(s)	Publication Status
4	B. Beauchamp, S. Rhodes, and N. Kandalaft "Differentiating Pinch and Grasp using sEMG", IEEE BioSmart 2023		Submitted
4	B. Beauchamp, S. Rhodes, and N. Kandalaft, "Coherence of Hand Muscles During Activities of Daily Living", IEEE CCWC 2022	Best Paper Best Presentation	Published
5	B. Beauchamp, N. Kandalaft, and K. Brakora, "MicroElectrodes for High Density Surface Electromyography", IEEE ICEESE 2023		Accepted
5	B. Beauchamp, C. Vollmers, S. Shahriar, and N. Kandalaft, "A Low Cost sEMG Development Platform for Hand Joint Angle Acquisition" IEEE IEMCON 2020	Best Paper Best Presentation	Published
5	B. Beauchamp and N. Kandalaft, "HD-sEMG for Human Interfacing Devices", IEEE IEMCON 2019		Published
6 (Journal)	B. Beauchamp, L. Corneal, and N. Kandalaft, "Privacy of biofeedback human interfacing devices", IJAAS 2022		Published

I certify that I have obtained written permission from the copyright owner(s) to include the above published material(s) in my thesis. I certify that the above material describes work completed during my registration as a graduate student at Grand Valley State University.

I declare that this is a true copy of my thesis, including any final revisions, as approved by my thesis committee and the Graduate Studies office, and that this thesis has not been submitted for a higher degree to any other University or Institution.

Appendix D - Vita Auctoris

Education

M.Sc. in Biomedical Engineering	2020 - 2023

Grand Valley State University, Grand Rapids, Michigan, USA
Advisor: Dr. Nabeeh Kandalaft
Thesis topic: Surface Electromyographic (sEMG) Transduction of Hand Joint Angles for Human Interfacing Devices (HID)

B.Sc. in Computer Engineering	2016 - 2023

Grand Valley State University, Grand Rapids, Michigan, USA

Awards and Accomplishments

Invited to present at GVSU Graduate Showcase	Apr. 2023
Awarded Graduate Citation for Academic Excellence and Outstanding Publication	Apr. 2023
Awarded $2500 in research grants from Grand Valley State University	2018 - 2023
President of Biomedical Engineering Society Grand Rapids Chapter	2022 - 2023
Treasurer of Biomedical Engineering Society Grand Rapids Chapter	2019 - 2022
Awarded Best Paper and Best Presentation	CCWC 2022
Special recognition from Padnos College of Engineering and Computing	Feb. 2021
Awarded Best Paper and Best Presentation	IEMCON 2020
Founding Member of Biomedical Engineering Society Grand Rapids Chapter	2019
Received International Baccalaureate Diploma	2016

Publications

B. Beauchamp and N. Kandalaft, "HD-sEMG for Human Interfacing Devices", IEMCON 2019

B. Beauchamp et. al, "A Low Cost sEMG Development Platform for Hand Joint Angle Acquisition" IEMCON 2020

C. Subedi et al, "MQTT Based Wi-Fi Communication Between Microcontroller and FPGA", IPCCC 2021

B. Beauchamp et al, "Privacy of Biofeedback Human Interfacing Devices", IJAAS 2022

B. Beauchamp et al, "Coherence of Hand Muscles During Activities of Daily Living", CCWC 2022

Bibliography

[1]   R. Merletti and D. Farina, Surface Electromyography: Physiology, Engineering, and Applications. John Wiley & Sons, 2016.

[2]   S. I. Fox, Human physiology. New York, NY: McGraw Hill Education Create, 2022.

[3]   Winter, D. A. (2023). Biomechanics and motor control of human movement (5th ed.). Wiley.

[4]   M. B. I. Raez, M. S. Hussain, and F. Mohd-Yasin, "Techniques of EMG signal analysis: Detection, processing, classification and applications," Biological procedures online, 2006.

[5]   R. Merletti, "The electrode–skin interface and optimal detection of bioelectric signals," Physiological Measurement, vol. 31, no. 10, 2010.

[6]   I. Talib, K. Sundaraj, C. K. Lam, J. Hussain, and M. A. Ali, "A review on crosstalk in Myographic signals," European Journal of Applied Physiology, vol. 119, no. 1, pp. 9–28, 2018.

[7]   R. Merletti and G. L. Cerone, "Tutorial. surface EMG detection, conditioning and pre-processing: Best practices," Journal of Electromyography and Kinesiology, vol. 54, p. 102440, 2020.

[8]   "Human Body Model for Electrostatic Discharge" [Online]. Available: http://www.aeroelectric.com/Reference_Docs/ESD/Human%20body%20model%20and%20ESD.pdf. [Accessed: 17-Feb-2023].

[9]   J. Wang, L. Tang, and J. E Bronlund, "Surface EMG Signal Amplification and Filtering," IJCA, vol. 82, no. 1, pp. 15–22, Nov. 2013, doi: 10.5120/14079-2073

[10]   E. M. Spinelli, P. Garcia, F. Guerrero, and M. Haberman, "A capacitive electrode with fast recovery feature," Research Gate.

[11]   Brendan. P. Beauchamp et. al, "A Low Cost sEMG Development Platform for Hand Joint Angle Acquisition" in 2020 IEEE 11th Annual Information Technology, Electronics and Mobile Communication Conference (IEMCON), Oct. 2020, doi: 10.1109/IEMCON51383.2020.9284889.

[12]   Gallina A;Peters S;Neva JL;Boyd LA;Garland SJ; "Selectivity of conventional electrodes for recording motor evoked potentials: An investigation with high-density surface electromyography," Muscle & nerve. [Online]. Available: https://pubmed.ncbi.nlm.nih.gov/27649483/. [Accessed: 07-Apr-2023].

[13]   Y. A. Patel, A. Willsie, I. P. Clements, R. Aguilar, S. Rajaraman, and R. J. Butera, "Microneedle cuff electrodes for extra fascicular peripheral nerve interfacing," 2016 38th Annual International Conference of the IEEE Engineering in Medicine and Biology Society (EMBC), 2016.

[14]   L. Mesin, "Crosstalk in surface electromyogram: Literature review and some insights," Physical and Engineering Sciences in Medicine, vol. 43, no. 2, pp. 481–492, 2020.

[15]   E. Brodsky, "Kmeans In C," University of Wisconsin - Madison, 2011. [Online]. Available: http://ece-research.unm.edu/jimp/codesign/project/2017/C_code/kmeans.c. [Accessed: 03-Jul-2022].

[16]   D. N. Rutledge and D. J.-R. Bouveresse, "Independent Components Analysis with the jade algorithm," TrAC Trends in Analytical Chemistry, 24-May-2013. [Online]. Available: https://www.sciencedirect.com/science/article/abs/pii/S0165993613001222. [Accessed: 03-Jul-2022].

[17]   A. Dogadov, C. Serviere, and F. Quaine, "Blind separation of surface electromyographic mixtures from two finger extensor muscles," Latent Variable Analysis and Signal Separation, pp. 481–488, 2015.

[18]   Jarque-Bou, N. J., Vergara, M., Sancho-Bru, J. L., Gracia-Ibáñez, V., & Roda-Sales, A. (2019). A calibrated database of kinematics and EMG of the forearm and hand during activities of daily living. Scientific Data, 6(1). https://doi.org/10.1038/s41597-019-0285-1

[19]   "Visible Body - Virtual Anatomy to See Inside the Human Body," Visible Body. http://www.visiblebody.com (accessed Oct. 25, 2020).

[20]   L. M. Biga, S. Dawson, A. Harwell, R. Hopkins, J. Kaufmann, M. LeMaster, P. Matern, K. Morrison-Graham, D. Quick, and J. Runyeon, "9.4 Synovial Joints," Anatomy Physiology, 26-Sep-2019. [Online]. Available: https://open.oregonstate.education/aandp/chapter/9-4-synovial-joints/#:~:text=Condyloid%20 joints%20are%20found%20at,the%20base%20of%20the%20 thumb. [Accessed: 17-Feb-2023].

[21]   E. Peña-Pitarch, "Virtual human hand: Autonomous grasping strategy," Modelling Simulation and Optimization, 2010.

[22]   E. Peña-Pitarch, Neus Ticó Falguera & Jingzhou (James) Yang, "Virtual human hand: model and kinematics", Computer Methods in Biomechanics and Biomedical Engineering, 2012

[23] J. Denavit and R. S. Hartenberg, "A Kinematic Notation for Lower-Pair Mechanisms Based on Matrices," DH Paper. [Online]. Available: https://home.konkuk.ac.kr/~cgkang/courses/robotics/courseMaterials/DHpaper.pdf.

[24] D. Ioannis, K. Anastasios, N. Konstantinos, K. Lazaros, and N. Georgios, "Palmaris longus muscle's prevalence in different nations and interesting anatomical variations: Review of the literature," Journal of Clinical Medicine Research, vol. 7, no. 11, pp. 825–830, 2015.

[25] D. C. McFarland, B. I. Binder-Markey, J. A. Nichols, S. J. Wohlman, M. de Bruin, and W. M. Murray, "A Musculoskeletal Model of the Hand and Wrist Capable of Simulating Functional Tasks," bioRxiv, p. 2021.12.28.474357, 2021, doi: 10.1101/2021.12.28.474357.

[26] Sollerman, C., & Ejeskär, A. (1995). Sollerman hand function test: A standardized method and its use in tetraplegic patients. Scandinavian Journal of Plastic and Reconstructive Surgery and Hand Surgery, 29(2), 167–176. https://doi.org/10.3109/02844319509034334

[27] "Cyberglove ii," CyberGlove Systems LLC. [Online]. Available: http://www.cyberglovesystems.com/cyberglove-ii/. [Accessed: 11-Dec-2022].

[28] Brendan. P. Beauchamp and Nabeeh. Kandalaft, "HDsEMG for Human Interfacing Devices," in 2019 IEEE 10th Annual Information Technology, Electronics and Mobile Communication Conference (IEMCON), Oct. 2019, pp. 0519–0522, doi: 10.1109/IEMCON.2019.8936298.

[29] "Device class definition for HID 1.11," USB. [Online]. Available: https://www.usb.org/document-library/device-class-definition-hid-111. [Accessed: 17-Feb-2023].

[30] Sartori, M., D. Farnia, and D. G. Lloyd, "Hybrid neuromusculoskeletal modeling to best track joint moments using a balance between muscle excitations derived from electromyograms and optimization," J. Biomech. 47, 3613-3621 (2014).

[31] "INA828 Datasheet" [Online]. Available: https://www.ti.com/lit/ds/symlink/ina828.pdf?&ts=1588932746855. [Accessed: 17-Feb-2023].

[32] R. Heine, K. Manal, and T. S. Buchanan, "Using hill-type muscle models and EMG data in a forward dynamic analysis of joint moment," Journal of Mechanics in Medicine and Biology, vol. 03, no. 02, pp. 169–186, 2003.

[33] Y. K. Kong, K. S. Lee, D. M. Kim, and M. C. Jung, "Individual finger contribution in submaximal voluntary contraction of gripping," (in eng), Ergonomics, vol. 54, no. 11, pp. 1072-80, Nov 2011, doi: 10.1080/00140139.2011.620176.

[34] P. Gerus, M. Sartori, T.F. Besier, B.J. Fregly, S.L. Delp, S. A. Banks, M. G. Pandy, D. D. D'Lima, D. G. Lloyd, "Subject - specific knee joint geometry improves predictions of medial tibiofemoral contact forces," J. Biomech. (2013).

[35] D. G. Lloyd, T. F. Besier, "An EMG-driven musculoskeletal model to estimate muscle forces and knee joint moments in vivo," J. Biomech. (2003).

[36] F. Sartori, D. Farnia, D. G. Lloyd, "EMG-driven forward-dynamic estimation of muscle force and joint moment about multiple degrees of freedom in the human lower extremity," PLoS One. (2012).

[37] C. R. Winby, D. G. Lloyd, T. F. Besier, T. B. Kirk, "Muscle and external load contribution to knee joint contact loads during normal gait," J. Biomech, (2009).

[38] T.S. Buchanan, D. G. Lloyd, K. Manal, and T.F. Besier, "Neuromusculoskeletal modeling: estimation of muscle forces and joint moments and movements from measurements of neural command." J. Appl. Biomech. (2004).

[39] Zajac, F. E., "Muscle and tendon: properties, models, scaling, and application to biomechanics and motor control," Crit. Rev. Biomed. Eng. 17 (1989)

[40] Scott, S. H. and Winter, D.A., A comparison of three muscle pennation angle assumptions and their effect on isometric and isotonic force, J. Biomech. 24 (1991)

[41] An, K. N., Takahashi, K., Harrigan, T. P. and Chao, E. Y., Determination of muscle orientations and moment arms, J. Biomech. Eng. (1984)

[42] K. Stollenwerk, A. Hinkenjann, and R. Klein, "Documentation on a database of grasp motions and its creation", [Online]. Available: https://pub.h-brs.de/frontdoor/deliver/index/docId/3462/file/TechReportGraspDB14_Stollen werk-web.pdf .

[43] Lee, S. K., & Wisser, J. R. (2012). Restoration of pinch in intrinsic muscles of the hand. Hand Clinics, 28(1), 45–51. https://doi.org/10.1016/j.hcl.2011.10.002

[44] J. A. Nichols, M. S. Bednar, S. J. Wohlman, and W. M. Murray, "Connecting the wrist to the hand: A simulation study exploring changes in thumb-tip endpoint force following wrist surgery," (in eng), J Biomech, vol. 58, pp. 97-104, Jun 14 2017, doi: 10.1016/j.jbiomech.2017.04.024.

[45] K. J. VanZwieten, K. P. Schmidt, G. J. Bex, P. L. Lippens, and W. Duyvendak, "An analytical expression for the D.I.P.–P.I.P. flexion interdependence in human fingers," Acta of Bioengineering and Biomechanics, vol. 17, no. 1.

[46] "CTRL-Labs Neural Interface Technology," CTRL. [Online]. Available:https://www.luxcapital.com/companies/ctrl-labs#:~:text=CTRL%2Dlabs%20has%20created%20a,the%20brain%20%2D%20no%20gestures%20required./. [Accessed: 08-Feb-2021].

[47]   Jarque-Bou, N., Vergara, M., Sancho-Bru, J., Roda-Sales, A., & Garcia-Ibanez, V. (2018, October 29). Identification of forearm skin zones with similar muscle activation patterns during activities of daily living - journal of Neuroengineering and Rehabilitation. BioMed Central. Retrieved December 6, 2022, from https://jneuroengrehab.biomedcentral.com/articles/10.1186/s12984-018-0437-0

[48]   R. Sica, A. McComas, A. Upton, and D. Longmire, "Motor Unit Estimations of Small Muscles in the Hand," Journal of Neurology, Neurosurgery and Psychiatry (JNNP). [Online]. Available: https://jnnp.bmj.com/content/jnnp/37/1/55.full.pdf. [Accessed: 10-Dec-2022].

[49]   S. Thongpanja, A. Phinyomark, C. Limsakul, and P. Phukpattaranont, "Application of mean and median frequency methods for identification of human joint angles using EMG Signal," Lecture Notes in Electrical Engineering, pp. 689–696, 2015.

[50]   "MYOWARE 2.0 Muscle Sensor," MYOWARE by Advancer Technologies, 01-Apr-2022. [Online]. Available: https://myoware.com/products/muscle-sensor/. [Accessed: 10-Dec-2022].

[51]   "Ulna," Ulna - an overview | ScienceDirect Topics. [Online]. Available: https://www.sciencedirect.com/topics/agricultural-and-biological-sciences/ulna. [Accessed: 10-Dec-2022].

[52]   D. Farina, C. Fevotte, C. Doncarli, and R. Merletti, "Blind separation of linear instantaneous mixtures of nonstationary surface myoelectric signals," IEEE Transactions on Biomedical Engineering, vol. 51, no. 9, pp. 1555–1567, 2004.

[53]   E. G. Lovett and K. M. Ropella, "Time-frequency coherence analysis of atrial fibrillation termination during Procainamide administration," Annals of Biomedical Engineering, vol. 25, no. 6, pp. 975–984, 1997.

[54]   Lindstrom, L., and R. Magnusson, "Interpretation of myoelectric power spectra: a model and its applications," Procc. IEEE 65, 653 – 662 (1977).

[55]   DeLuca, C. J., "Physiology and mathematics of myoelectric signals," IEEE Trans. Biomed. Eng. (1979).

[56]   Lago, P. J., and N. B. Jones, "Effect of motor unit firing time statistics on e.m.g. spectra," Med. Biol. Eng. Comput. 5, 648-655 (1977).

[57]   Clancy, E. A., Bertolina, M. V., Merletti, R., & Farina, D. (2008). Time- and frequency-domain monitoring of the myoelectric signal during a long-duration, cyclic, force-varying, fatiguing hand-grip task. Journal of Electromyography and Kinesiology, 18(5), 789–797. https://doi.org/10.1016/j.jelekin.2007.02.007

[58] "Biering-Sørensen Test," Shirley Ryan AbilityLab. [Online]. Available: https://www.sralab.org/rehabilitation-measures/beiring-sorensen-test. [Accessed: 15-Nov-2021]. [H] J. P. M. Mogk and P. J. Keir, "Crosstalk in surface electromyography of the proximal forearm during gripping tasks," Journal of Electromyography and Kinesiology, vol. 13, no. 1, pp. 63–71, 2003.

[59] J. P. M. Mogk and P. J. Keir, "Crosstalk in surface electromyography of the proximal forearm during gripping tasks," Journal of Electromyography and Kinesiology, vol. 13, no. 1, pp. 63–71, 2003.

[60] M. Yung and R. P. Wells, "Changes in muscle geometry during forearm pronation and supination and their relationships to EMG cross-correlation measures," Journal of Electromyography and Kinesiology, vol. 23, no. 3, pp. 664–672, 2013.

[61] M. A. Islam, K. Sundaraj, R. B. Ahmad, S. Sundaraj, N. U. Ahamed, and M. A. Ali, "Cross-talk in mechanomyographic signals from the forearm muscles during sub-maximal to maximal isometric grip force," PLoS ONE, vol. 9, no. 5, 2014.

[62] B. Beauchamp, L. Corneal, and N. Kandalaft, "Privacy of biofeedback human interfacing devices", IJAAS 2022

[63] "PowerLab C," ADInstruments. [Online]. Available: https://www.adinstruments.com/products/powerlab/c.

[64] "MA-400 User Manual - Motion Lab Systems," Motion Labs. [Online]. Available: https://motionlabsystems.com/wp-content/uploads/2020/07/ma400_user_manual.pdf. [Accessed: 17-Feb-2023].

[65] "ADS1298 analog front end," Mouser, 02-Sep-2011. [Online]. Available: https://www.mouser.in/new/texas-instruments/ti-ads1298-afe/. [Accessed: 17-Feb-2023].

[66] "Fujitsu Semiconductor FRAM" [Online]. Available: https://www.fujitsu.com/us/Images/SPBG_FRAM_Overview_JP.pdf. [Accessed: 17-Feb-2023].

[67] Alliance memory AS7C1024B SRAM. Alliance Memory. (2023, February 23). Retrieved April 2, 2023, from https://www.alliancememory.com/

[68] S34ML08G2 Datasheet. ALLDATASHEET. Retrieved April 2, 2023, from https://pdf1.alldatasheet.com/datasheet-pdf/view/1046739/CYPRESS/S34ML08G2.html

[69] "Motion Labs MA720," Motion Labs. [Online]. Available: https://motionlabsystems.com/. [Accessed: 17-Feb-2023].

[70]   C. Subedi, B. P. Beauchamp, and N. Kandalaft, "MQTT based Wi-Fi communication between microcontroller and FPGA," 2021 IEEE International Performance, Computing, and Communications Conference (IPCCC), 2021.

[71]   "Surface area of human skin," Surface Area of Human Skin - Human Homo sapiens - BNID 100578. [Online]. Available: https://bionumbers.hms.harvard.edu/bionumber.aspx?s=y&id=1 00578&ver=1. [Accessed: 30-Mar-2022].

[72]   P. C. Liu, J. Zhou, S. L. Li, and H. M. Ma, "Review of microelectrode fabrication," Advanced Materials Research, vol. 565, pp. 503–507, 2012.

[73]   B.-J. Choi, J.-H. Kim, W.-J. Yang, D.-J. Han, J. Park, and D.-W. Park, "Parylene-based flexible microelectrode arrays for the electrical recording of muscles and the effect of electrode size," Applied Sciences, vol. 10, no. 20, p. 7364, 2020.

[74]   "Precision full-wave rectifier, dual-supply - Texas Instruments." [Online]. Available: https://www.ti.com/lit/ug/tidu030/tidu030.pdf. [Accessed: 08-Apr-2023].